Combined Short-lived (^{182}W, ^{142}Nd) and Long-Lived (^{147}Sm-^{143}Nd) Isotope Study on Rocks from the Pulpwood-Playter Harbour Sequence (Wawa Subprovince): Constraints on the Mantle Source of Neoarchean Ferropicrites

Ayesha Landon-Browne

A thesis submitted in partial fulfillment of the requirements for the Master's degree in Earth Sciences

Department of Earth and Environmental Sciences
Faculty of Science
University of Ottawa

Abstract

Short-lived isotope systems can be utilized to track differentiation processes that had occurred during Earth's early history. Both the ^{182}Hf-^{182}W and ^{146}Sm-^{142}Nd systems are sensitive to silicate fractionation events due to differing parent-daughter incompatibilities. The ^{182}Hf-^{182}W system is also affected by metal-silicate fractionation events due to the siderophile nature of W. An increasing number of mantle-derived rocks, mainly formed during the Archean (4.0-2.5 Ga), have presented variable anomalies in the daughter products of both systems, indicating their sources contain isotope signatures established shortly after the formation of the Earth.

Some Archean Fe-rich primitive magmas known as ferropicrites, have been suggested to derive from mantle domains that differentiated after the crystallization of a Hadean (>4.0 Ga) magma ocean. In order to investigate the potential involvement of a Hadean source in the petrogenesis of Archean ferropicrites, we have studied the Nd and W isotopic compositions of rocks from the Pulpwood-Playter Harbour sequence in the Wawa subprovince, Ontario, Canada. This sequence is composed of ferropicritic intrusive rocks and lavas in association with tholeiitic mafic lavas. A ^{147}Sm-^{143}Nd isochron including all lithologies yields an age of 2681±51 Ma (MSWD =6.6) with an initial ε^{143}Nd of +2.5. This Nd initial isotopic composition indicates the rocks were derived from a long-term incompatible-element depleted mantle source. Both the ferropicritic and the tholeiitic rocks plot on the same isochron, suggesting they derived from the same mantle source, despite their different geochemical compositions. Negative ^{142}Nd anomalies compared to the Nd terrestrial standard were found in the majority of the rocks studied here, yielding an average μ^{142}Nd value of -2.0±3.9. Although not resolvable from the terrestrial standard given

the current analytical precision, the fact that almost all analysed samples exhibit negative $\mu^{142}Nd$ values could suggest the influence of a Hadean source in their formation. If this is the case, a single early silicate fractionation event occurring between 4.56 and 4.47 Ga could explain both the $\varepsilon^{143}Nd$ and $\mu^{142}Nd$ values obtained for the studied rocks. Alternatively, the involvement of eclogitic material, with a Hadean basaltic protolith, interacting with Archean peridotitic mantle could explain the Nd isotopic composition of the ferropicrites, but this would not account for the identical isotopic composition of the tholeiites – thus rendering a garnet pyroxenite source improbable. One intrusive ferropicritic sample yielded a resolvable ^{182}W excess of +14.1 ±6.7 ppm. If this excess ^{182}W is characteristic of the Pulpwood-Playter Harbour sequence, it indicates the decoupling of ^{182}Hf-^{182}W and ^{146}Sm-^{142}Nd systems. This decoupling could be explained by early metal-silicate fractionation recorded in the Hf-W systematics of these rocks or the contribution of Fe-rich meteoritic material into the source of ferropicrites.

Acknowledgments

First and foremost my biggest thanks go to my supervisors, Jonathan O'Neil (University of Ottawa) and Hanika Rizo (Carleton University) for the privilege to complete my time as a Master's student under their guidance and supervision. I am eternally grateful for your time and patience you have provided me both within my academic pursuits and extra curricular endeavours. The assistance and knowledge you have passed on in the lab, in the interpretation of data and in the field have allowed this project to be possible.

I would also like to thank all the laboratory staff that have made the attainment of data possible. This includes Alain Mauviel for preparing thin sections of the samples collected, Nimal DeSilva and Smita Mohanty at the University of Ottawa geochemistry laboratories, Lilianne Pagé for XRF major element analysis. Thanks also go to Shuangquan Zhang at the Carleton University IGGRC for his help with TIMS analysis and allowing us to use the instrument for weeks at a time. Fieldwork would not have been possible without the support of Parks Canada and the staff at Pukaskwa National Park.

The other students of the Ottawa-Carleton Early Earth group – Dan Stepner, Benjamin Wasilewski, Janick Flageole, Christian Sole, Andréane Mitchelle-Dupuis, Alexandre Rouleau, and Victor Garcia, thank you for the time we have been together. Your support, feedback and assistance have allowed me to have fun both inside and outside of the lab and have formed many good memories. I would also like to thank the Department of Earth Sciences here at the University of Ottawa, and my fellow graduate students within the department. The constant support and words of encouragement that I have received over the past few years have been motivating and have provided a lot of support during my time here as a graduate student.

A last thanks goes to my friends and family outside of the world of Earth sciences. Thank you to my parents and brother for supporting me through this endeavour, and dealing with my very specific interests in Earth sciences.

Table of Contents

List of Figures

List of Tables

1.0 Introduction

Ferropicrites are Fe-rich ultramafic rocks whose occurrence was widespread during the Archean Eon (4.0 -2.5 Ga) and seem to have become increasingly rare since (Gibson, 2002). They have been commonly misidentified as aluminum depleted komatiites (ADK), but studies have suggested that their geochemical characteristics are different to that of komatiites (Hanksi and Smolkin, 1989; Gibson et al., 2000; Gibson, 2002; Goldstein and Francis, 2008). Ferropicrites can be alkaline or subalkaline in composition and are characterized by a high FeO content (>14 wt.%), with MgO content generally similar to that of picrites and komatiites (~12-18 wt.%). They are also characterized by depletions in Al_2O_3, and enrichments in TiO_2 and incompatible trace elements.

Ferropicrites predominantly occurred during the Archean, but Proterozoic and Phanerozoic ferropicrites have also been identified. Their decrease in occurrence has been attributed towards a decrease in the temperature and Fe contents of the mantle since the Archean (Francis et al., 1998; Gibson et al., 2000; Gibson, 2002). The petrogenesis of Archean, Proterozoic, and Phanerozoic ferropicrites remains debated and different hypotheses have been put forward. Studies have suggested that ferropicrites could source from olivine cumulate domains that crystallized from a deep-seated Hadean magma ocean (Goldstein and Francis, 2008; Kitayama and Francis, 2014), from garnet pyroxenite domains produced from the interaction of eclogite melt and peridotitic mantle (Gibson 2002; Milidragovic and Francis, 2014; Jennings et al., 2016), or from late accreted Martian or Vesta-like affinity material into the mantle (Milidragovic and Francis 2014).

This thesis provides a geochemical and isotopic study of ferropicrites from the Pulpwood-Playter Harbour (PPH) volcanic sequence from the Wawa subprovince (Superior Province, Canada). This sequence was previously studied by Kitayama and Francis (2014), where detailed petrography and geochemical compositions of the different lithologies were determined. They identified Fe-rich and tholeiitic-like lavas, as well as Fe-rich intrusive rocks grading from dunites and peridotites to clinopyroxenites and gabbros. The parental magma of the Fe-rich intrusive rocks was estimated to have ~19 wt.% FeO and ~9 wt.% MgO, representing one of the most Fe-rich magmas of the Wawa subprovince. These geochemical characteristics, along with a well-preserved field sequence, have made the PPH rocks a prime example of an Archean ferropicritic occurrence.

The main goal of this study was to use the ^{142}Nd and ^{182}W short-lived isotopes to investigate any possible involvement of a Hadean mantle source in the formation of Archean ferropicrites. These early-formed isotopes are ideal tracers of early-silicate differentiation events. For this study, 61 samples were collected from the PPH sequence. All samples were analysed for whole-rock major and trace element concentrations, which allowed for the selection of the most representative lithological samples for isotopic work (^{147}Sm-^{143}Nd, ^{142}Nd and ^{182}W).

An overview of the characterization, occurrences and current existing petrogenetic models for ferropicrites is provided in Section 2.0; the geological setting of the Pulpwood-Playter Harbour sequence is described in Section 3.0; and Section 4.0 explains the isotope systematics applied in this study. The detailed analytical methods are presented in Section 5.0 and Appendix A, B and C. The results of the major and trace element analyses are found in Section 6.0 and in

Appendices D to F. Finally, Section 7.0 gives the interpretation and discussion of the results, and the conclusions can be found in Section 8.0.

2.0 Main characteristics, occurrences and theories of the origin of ferropicrites

Ferropicrites are rocks that can be classified as picritic in composition, but are distinguished from picrites by a higher Fe content. In general, a ferropicritic magma is characterized by FeO contents above 14 wt.%, MgO contents between 12 and 18 wt.%, Al_2O_3 contents lower than 10 wt.%, TiO_2 ranging from 1 to 2 wt.% and enrichments in light rare earth elements (LREE) (Hanski and Smolkin, 1989; Gibson et al., 2000; Gibson, 2002; Heinonen and Luttinen, 2008; Goldstein and Francis, 2008; Kitayama and Francis, 2014; Milidragovic and Francis, 2016; Jennings et al., 2016). Ferropicrites can compositionally be reminiscent of aluminum-depleted komatiites (ADK). However, the aforementioned studies suggest that due to some of their geochemical differences (e.g. higher Fe contents, LREE enrichments and depletions in Al_2O_3), their petrogenesis cannot be the same as the ADK.

Ferropicrites were first identified by Hanski and Smolkin (1989) in the Proterozoic Kola Peninsula from the Pechenga Province (Russia). Since their discovery, ferropicrites have been identified worldwide (Figure 2.1), with Archean occurrences commonly associated with greenstone belts located in the Superior, Slave, Yilgarn and Kaapvaal cratons (Goldstein and Francis, 2008; Kitayama and Francis, 2014; Milidragovic and Francis, 2016).

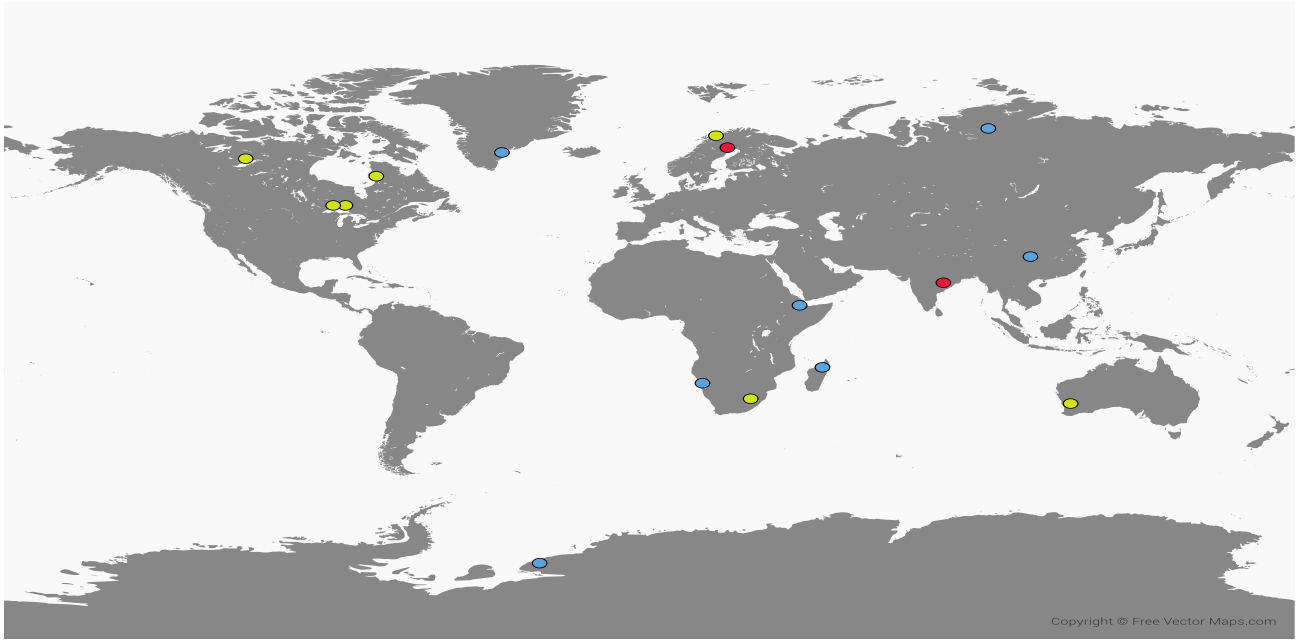

Figure 2.1: Global distribution of ferropicritic occurrences, Archean (yellow circles), Proterozoic (blue circles) and Phanerozoic (red circles). Modified after maps presented by Heinonen and Luttinen (2008), Milidragovic and Francis (2016), Jennings (2016).

The decrease in ferropicritic occurrences after the Archean has loosely been attributed towards the mantle being hotter (Campbell and Griffiths, 1992) and more Fe-enriched during the Archean compared to the Proterozoic and Phanerozoic mantle. This is supported by the observation that post-Archean ferropicrites have lower FeO contents (Francis et al., 1999; Gibson, 2002). Given their Fe contents and related density, Archean ferropicritic lavas would have been able to become buoyant in the Archean mantle (Kitayama and Francis, 2014) and rise to the surface; this would be more difficult after the Archean due to the aforementioned mantle changes. It has also been noted that some occurrences of Archean ferropicrites, within the Superior Province, cannot have come from the melting of the peridotitic mantle (Goldstein and Francis, 2008). This was shown through experimental petrological studies where melting at up to 20 GPa of peridotite with Mg# = 89-90, did not reach the necessary enrichment to generate ferropicrites despite resulting in an Fe-enrichment in the produced magma (Goldstein

and Francis, 2008). However, assuming a more Fe-rich Archean mantle source with an Mg# 85, melting at ~5 GPa, would produce a magma with Fe-enrichments comparable to ferropicrites (Goldstein and Francis, 2008). As such, Goldstein and Francis (2008) suggest that Archean ferropicrites from the Superior Province could be the result of melting of an olivine cumulate that had crystallized from a deep-seated Hadean magma ocean.

Post-Archean ferropicrite occurrences have been noted in association with large igneous provinces and continental flood basalts (Hanski and Smolkin, 1989; Gibson et al., 2000; Gibson, 2002; Heinonen and Luttinen, 2008; Jennings et al., 2016). Gibson et al. (2000) suggested that this association results from variations in the composition of their contributing melt source regions; while flood basalts would derive from melting of peridotitic mantle, ferropicrites could derive from the preferential melting of Fe-rich pyroxenite 'streaks' in upwelling mantle plume heads. The nature and origin of these Fe-rich streaks is unclear, and hypotheses include the existence of eclogite/pyroxenite heterogeneities in the convective mantle or high-Fe domains in the lower mantle created after the crystallization of a magma ocean or input of core material into the lower mantle (Gibson 2000 and references therein; Francis et al., 1998). Alternatively, they could come from the denser Fe-rich portions of iron-silica immiscibility melts (Jakobsen, 2005). These Fe-rich portions of the mantle would preferentially melt over normal peridotic mantle, and as such form the head of the plume. The geochemical composition of these Fe-rich layers, however, is different to that of ferropicrites and mixing with picritic mantle material would be necessary (Jakobsen et al., 2005).

Alternatively, it has been proposed that a garnet pyroxenite (Gibson, 2002) or a silica-deficient pyroxenite (Jennings et al., 2016) could be the source of post-Archean ferropicrites. Mantle

pyroxenite is formed through the metasomatism of mantle peridotite by melts from eclogite, formerly subducted basaltic crust (Green and Ringwood, 1967). This interaction could produce a pyroxenite which, when undergoing partial melting is characterized by a high FeO and low CaO contents due to low degrees of partial melting and depleted in Al_2O_3 due to their high pressure of formation (Jennings et al., 2016). A study on Pleistocene silica-poor ferropicrites from North China suggested they were formed by melting of silica deficient/iron rich eclogite that has come from a continental protolith and stagnated in the upper mantle (Zhang et al., 2017). The pressure dependent compatibility of Fe in garnet will also fractionate Y, Yb and Lu, with Fe and Y becoming incompatible in eclogitic garnet at pressures >5 GPa (Tuff et al., 2005; Zhang et al., 2017). The breakdown of garnet under these conditions releases Fe and allows the upper mantle to undergo Fe enrichment. The resulting iron-enriched silica-deficient pyroxenite would be less dense than the surrounding peridotite, allowing the plume to rise.

Milidragovic and Francis (2016) noted that ferropicritic compositions, particularly subalkaline ferropicrites, overlapped with that of shergottite-nakhlite-chassignite (SNC) and howardite-eucrite-diogenite (HED) achondritic meteorites. These meteorites are thought to be representative of the Martian or Vesta surface, respectively. The similarities in geochemical compositions suggest that ferropicrites have derived from a mantle source that was subjected to an influx of SNC and HED material (Milidragovic and Francis, 2014). These sources would be characterized by Fe and Mg enrichments, and could give rise to Archean ferropicrites.

3.0 Geological Setting

The PPH sequence is part of the Schreiber-Hemlo greenstone belt (SHGSB) (Figure 3.1), which is located in the northern section of the Wawa subprovince of the Superior Province (Canada).

The SHGSB evolved as an oceanic plateau between 2750-2725 Ma (Polat et al., 1998) and consists of tholeiitic and transitional to alkaline basalts (Polat, 2009). The SHGSB transitioned from an oceanic plateau to a subduction margin at ~2.72 Ga, forming an oceanic island arc (Polat, 2009; Polat et al., 1998).

The SHGSB can be further subdivided into three lithotectonic metavolanic assemblages; Heron Bay, Hemlo-Black River and Schreiber greenstone belt assemblages. The Heron Bay assemblage hosts the PPH sequence and is bounded to the south by the Pukaskwa gneissic complex (2.72-2.69 Ma) and the Heron Bay Pluton (2.69 Ga) to the north (Figure 2.1). The estimated age of the PPH sequence is ~2.72 Ga (Corfu and Muir, 1989), and has been inferred from field relationships and U-Pb dating of surrounding plutons, which range in age from 2.69-2.72 Ga. It has been interpreted that the PPH sequence was intruded by these plutons, as such rendering it older.

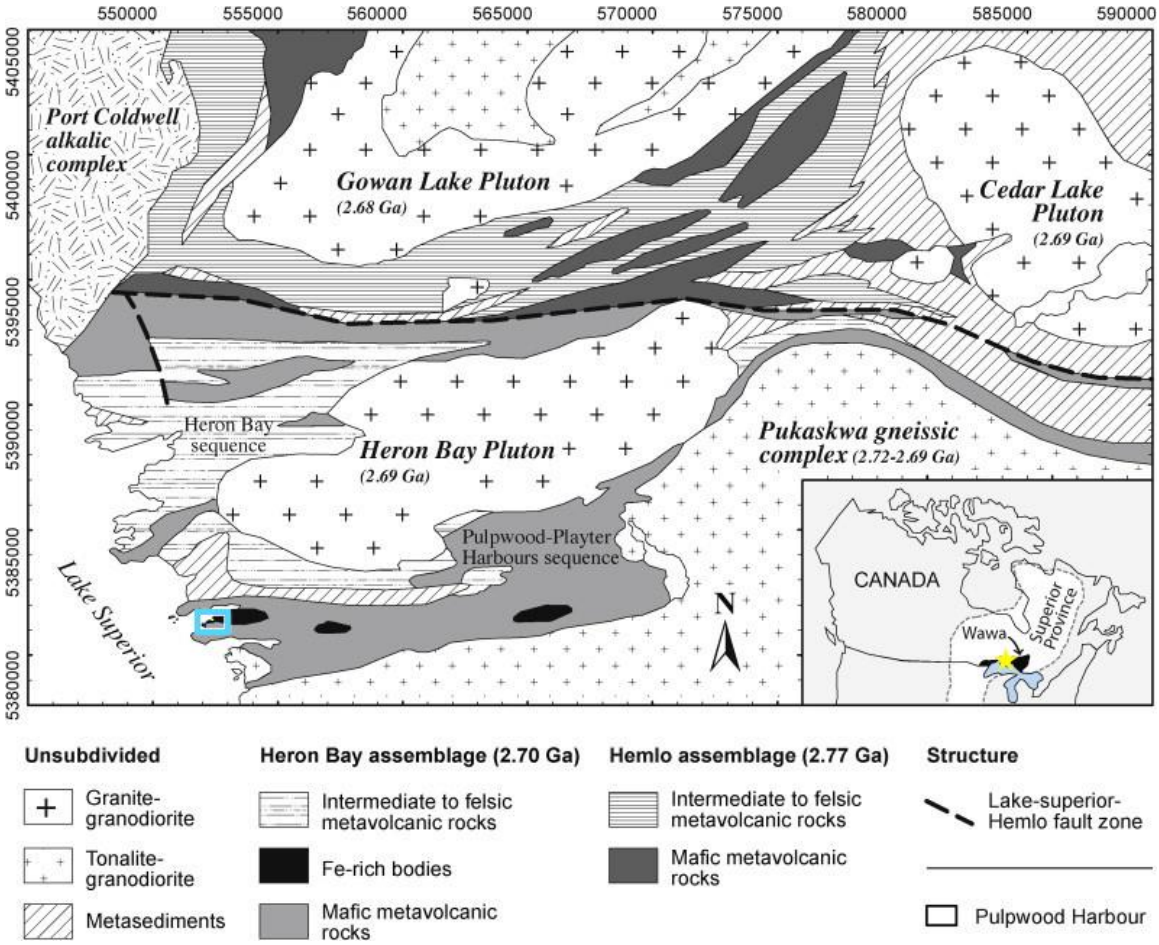

Figure 3.1: Simplified map of the Schreiber-Hemlo greenstone belt. Blue square – study area, yellow star on inset – location of SHGSB in the Wawa subprovince, modified after Kitayama and Francis, 2014.

Figure 3.2 shows a simplified geological map of the PPH sequence with the main lithologies described by Kitayama and Francis (2014), and Figure 3.3 shows a simplified stratigraphic log of lithologies. Three distinct units compose the PPH sequence: 1) underlying pillow basalts with tholeiitic-like affinity, 2) differentiated alkaline Fe-rich intrusive rocks, and 3) overlying Fe-rich basaltic pillow lavas.

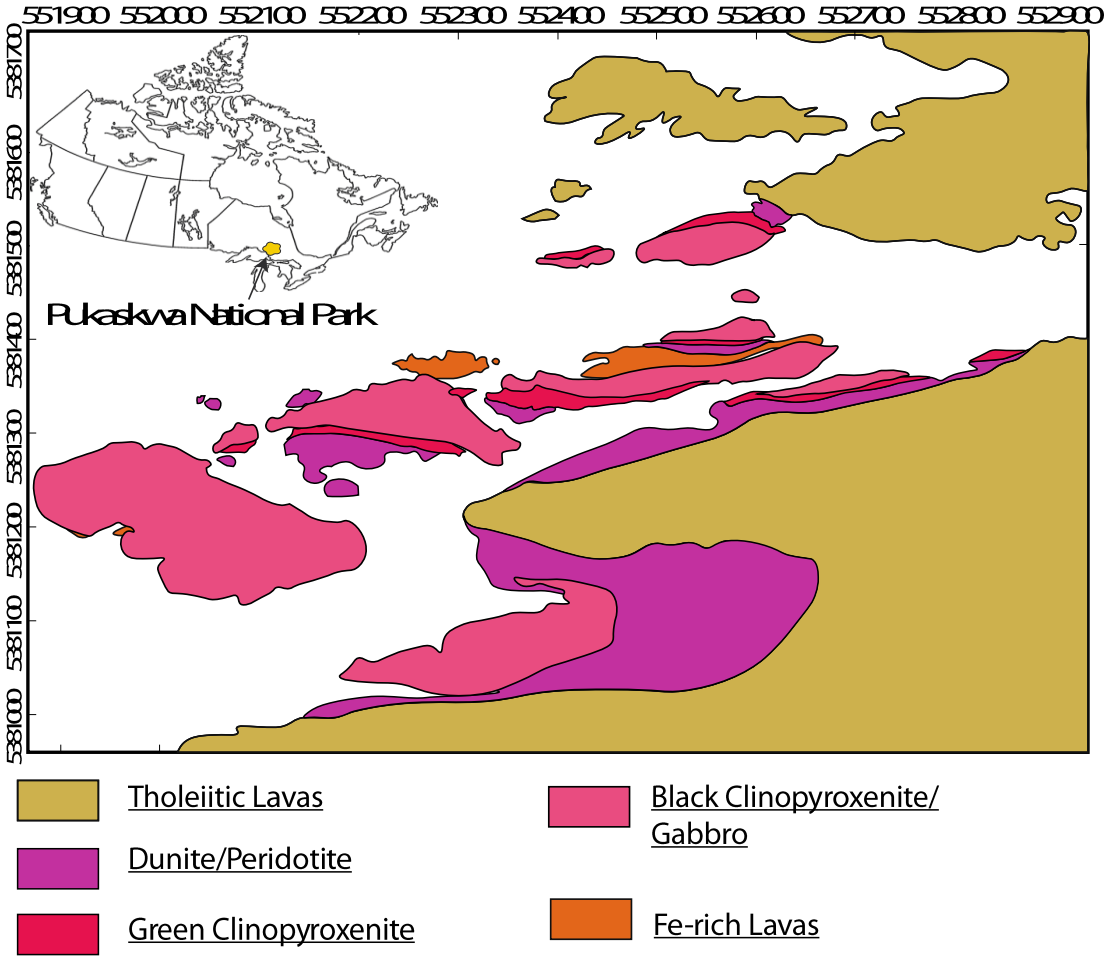

Figure 3.2: Simplified geological map of the Pulpwood-Playter Harbour. Coordinates are in UTM NAD 27, zone 16. Modified after Kitayama and Francis (2014).

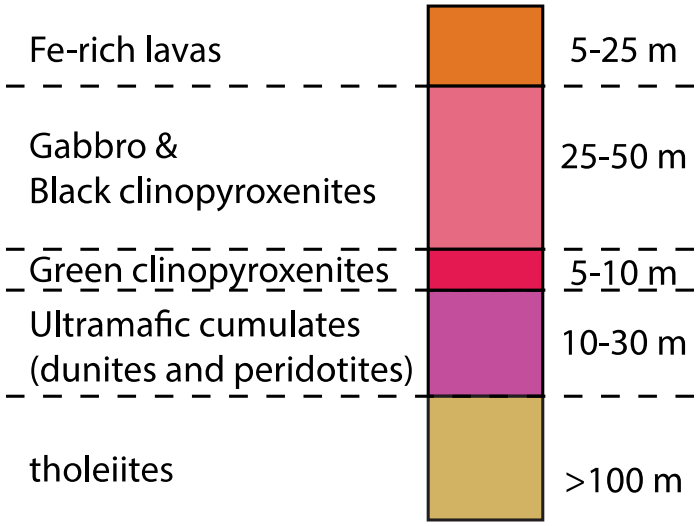

Figure 3.3: Stratigraphic log of the Pulpwood-Playter Harbour sequence with relative unit thicknesses, modified after Kitayama and Francis (2014).

Field relationships (Figure 3.3) suggest that the underlying tholeiites are older than the overlying Fe-rich rocks and despite their close spatial association with the ferropicrites, it is not known if they are coeval, or if they have been sourced from the same mantle source (Kitayama and Francis, 2014). The PPH sequence has been metamorphosed to greenschist facies, but both the overlying and underlying volcanic occurrences exhibit well-preserved pillow lava structures (Kitayama and Francis, 2014).

The intrusive rocks are composed of three distinct units, ultramafic rocks (dunites and peridotites), green and black clinopyroxenites, and gabbros (Kitayama and Francis, 2014). There is no sharp contact between the intrusive rocks, but each unit is evident based on their mineralogy phases that are present (Kitayama and Francis). The ultramafic rocks are primarily composed of serpentinite pseudomorphing olivine serpentine, the clinopyroxenites consist of elongated amphibole minerals and the gabbroic samples are composed of plagioclase feldspar and amphibole (Kitayama and Francis, 2014). As a whole, the intrusive unit is relatively well

preserved, although calcite, quartz veining and sulphides are found throughout the units (Kitayama and Francis, 2014). The underlying tholeiites are green in colour, fine-grained, and are not as well preserved as the overlying Fe-rich lavas, which are black in colour (Kitayama and Francis, 2014).

4.0 Isotope Systematics

4.1 Sm-Nd isotopes

Samarium (Sm) and Neodymium (Nd) are lithophile, refractory, rare earth elements, and have similar incompatibilities, however, Nd is slightly more incompatible than Sm. Samarium has seven naturally occurring isotopes, of which ^{147}Sm is still undergoing radioactive decay into ^{143}Nd with a half life of 106 Ga, and is utilized for Sm-Nd geochronology. The short-lived, now extinct, ^{146}Sm decayed into ^{142}Nd with a half-life of 103 Ma, and is used to detect processes causing Sm/Nd fractionation within the first ~500 Ma of the Solar System history.

4.1.1 Long-lived ^{147}Sm-^{143}Nd isotope systematics

The decay of ^{147}Sm to ^{143}Nd can be used to date rocks using their different minerals or suites of co-genetic rocks, as well as to trace crust-mantle differentiation processes throughout the history of Earth. The high closure temperature (600-650°C) of Sm-Nd allows for the system to remain closed during relatively high metamorphic grade events, resulting in a greater reliability on isochron dating, compared to the Rb-Sr system. In order to apply isochron dating to a suite of rocks, several assumptions must be made; the rocks must be co-genetic, and therefore have the same initial isotopic composition (^{143}Nd/^{144}Nd), and the system must not have reopened (i.e. not have undergone metamorphic resetting) since their time of formation. The amount of

daughter product (^{143}Nd) in the system is dependent on two things: 1) how much ^{143}Nd was in the system (minerals or rocks) at the time of crystallization, and 2) how much of the parent ^{147}Sm nuclide has decayed into ^{143}Nd since crystallization. This can be expressed with the following radioactive decay equation:

$$\left(\frac{^{143}Nd}{^{144}Nd}\right) = \left(\frac{^{143}Nd}{^{144}Nd}\right)_{t=0} \left(\frac{^{147}Sm}{^{144}Nd}\right)(e^{\lambda t} - 1)$$

where *t=0* is the time of crystallization, *t* is the time between crystallization and present day, and λ is the ^{147}Sm decay constant. The present day ^{143}Nd/^{144}Nd and ^{147}Sm/^{144}Nd isotopic compositions can be measured and plotted on a ^{143}Nd/^{144}Nd vs. ^{147}Sm/^{144}Nd diagram (Figure 4.1) called the "isochron diagram". Co-genetic samples and that have not been subjected to post-formation disturbances will show correlations between the measured ^{143}Nd/^{144}Nd vs. ^{147}Sm/^{144}Nd (Figure 4.1b). The slope in an isochron diagram is proportional to the age of the samples, where the slope is equivalent to $e^{\lambda t}$-1. Since the decay constant of ^{147}Sm is known (λ^{147}Sm=6.54x10^{-12}) time can be calculated. The intercept of the y-axis, when ^{147}Sm/^{144}Nd=0, gives the initial ^{143}Nd/^{144}Nd composition of the co-genetic suite, which reflects the isotopic composition of the rocks at the time of their formation as well as the isotopic composition of their source.

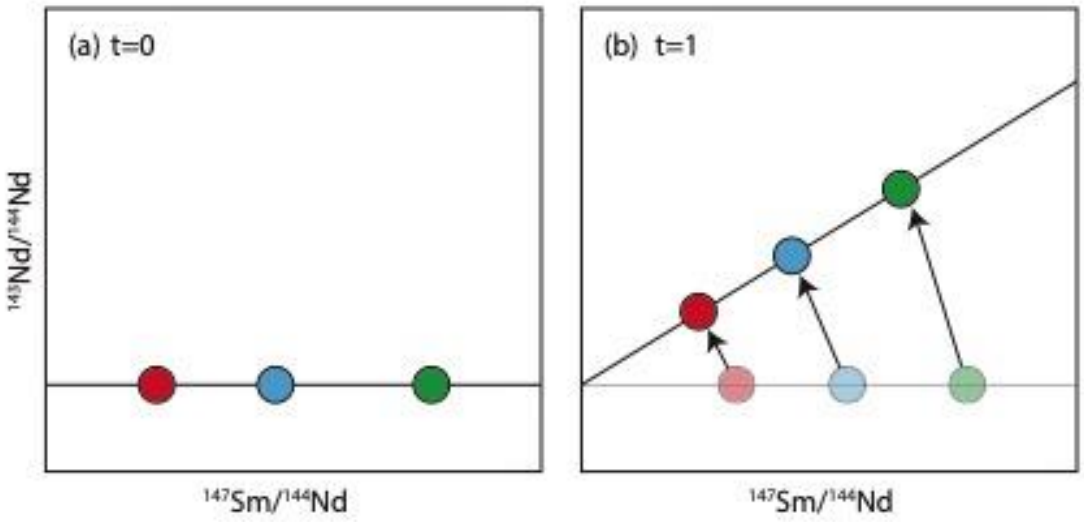

Figure 4.1: Schematic of the evolution of the ^{147}Sm-^{143}Nd system. (a) At the time of crystallization (t=0), the samples have the same $^{143}Nd/^{144}Nd$ ratio, but varying $^{147}Sm/^{144}Nd$ ratios. (b) As time elapses, the ^{147}Sm decays to ^{143}Nd, increasing the $^{143}Nd/^{144}Nd$ ratio and decreasing the $^{147}Sm/^{1444}Nd$ ratio.

Due to the differences in incompatibility of Sm and Nd within most minerals in the mantle and the crust, partial melting and fractional crystallization fractionates the Sm/Nd ratio of the differentiated products, which will evolve to variable $^{143}Nd/^{144}Nd$ compositions. During igneous processes, Nd is more incompatible than Sm; therefore, melts will have a lower Sm/Nd ratio compared to the solid. When the system closes (i.e. cools below the closure temperature), the Nd-depleted reservoir with the higher Sm/Nd ratio will evolve to become more radiogenic compared to the Nd-enriched reservoir with a lower Sm/Nd ratio, becoming less radiogenic with time (Figure 4.2).

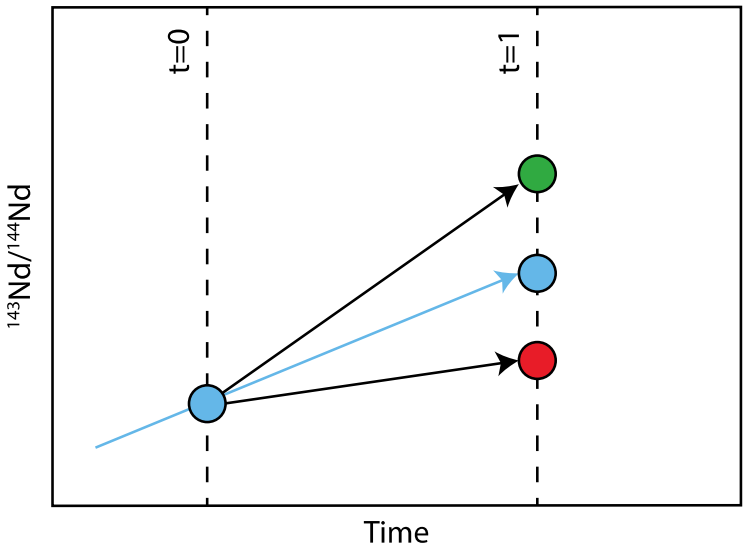

Figure 4.2: Evolution of the $^{143}Nd/^{144}Nd$ ratios for three reservoirs. Differentiation of the initial source (blue) occurs at t=0, forming an Nd-depleted reservoir (green) and an Nd-enriched reservoir (red). As time elapses to t=1 the isotopic compositions of these reservoirs will evolve differently depending on their Sm/Nd ratios. Modified after Allègre (2008).

The initial $^{143}Nd/^{144}Nd$ isotopic compositions can be expressed as $\varepsilon^{143}Nd$ values, which are deviations of the $^{143}Nd/^{144}Nd$ ratio from the chondritic uniform reservoir (CHUR):

$$\varepsilon^{143}Nd = \left(\frac{\left(\frac{^{143}Nd}{^{144}Nd}\right)_{sample}}{\left(\frac{^{143}Nd}{^{144}Nd}\right)_{CHUR}} - 1 \right) * 10^4$$

CHUR isotopic compositions are determined from undifferentiated chondritic meteorites and the present day values are $^{143}Nd/^{144}Nd=0.512630$ and $^{147}Sm/^{144}Nd=0.1960$ (Bouvier et al., 2008). Reservoirs evolving with a lower Sm/Nd compared to CHUR will have $\varepsilon^{143}Nd<0$ and reservoirs evolving with a suprachondritic Sm/Nd ratio will have $\varepsilon^{143}Nd>0$ (Figure 4.3).

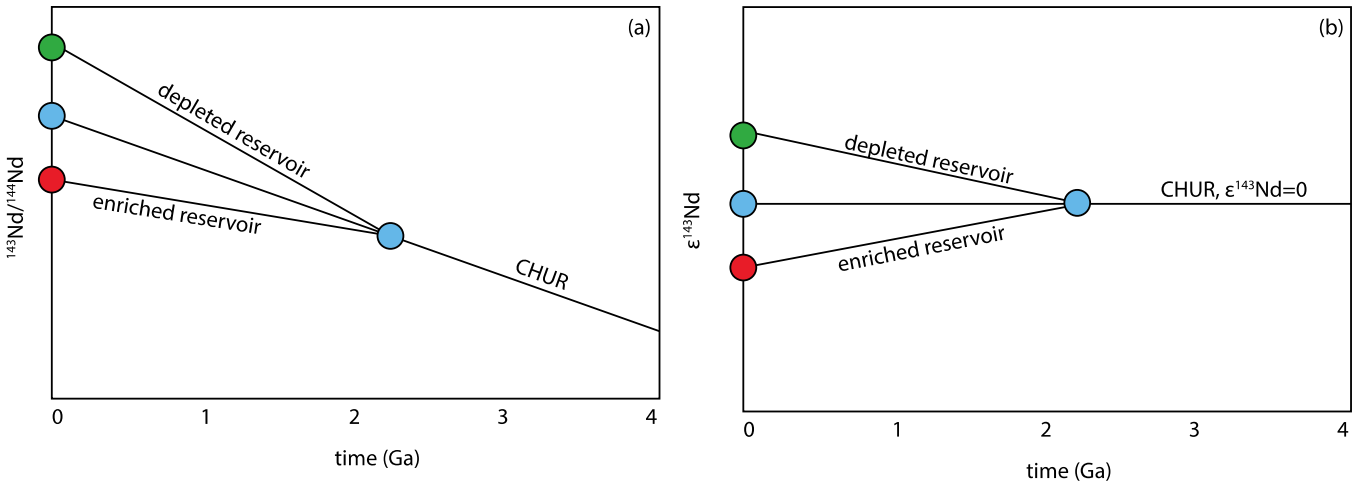

Figure 4.3: (a) $^{143}Nd/^{144}Nd$ vs. time for a depleted reservoir and an enriched reservoir with respect to CHUR (b) $\varepsilon^{143}Nd$ vs. time for an enriched and depleted reservoir, with respect to CHUR ($\varepsilon^{143}Nd_{CHUR} = 0$).

4.1.2 Short-lived ^{146}Sm-^{142}Nd isotope systematics

The short-lived ^{146}Sm decayed into ^{142}Nd with a half-life of 103 Ma, resulting in the system becoming extinct after ~500 Ma of Solar System formation. Therefore, variations in ^{142}Nd can only be produced by Sm/Nd fractionation occurring within the Hadean Eon (4.56-4.0 Ga) (Figure 4.4). This system cannot be used to date samples that have formed after the extinction of ^{146}Sm, but its applications are useful for studying early silicate differentiation events that would occur shortly after Earth's accretion.

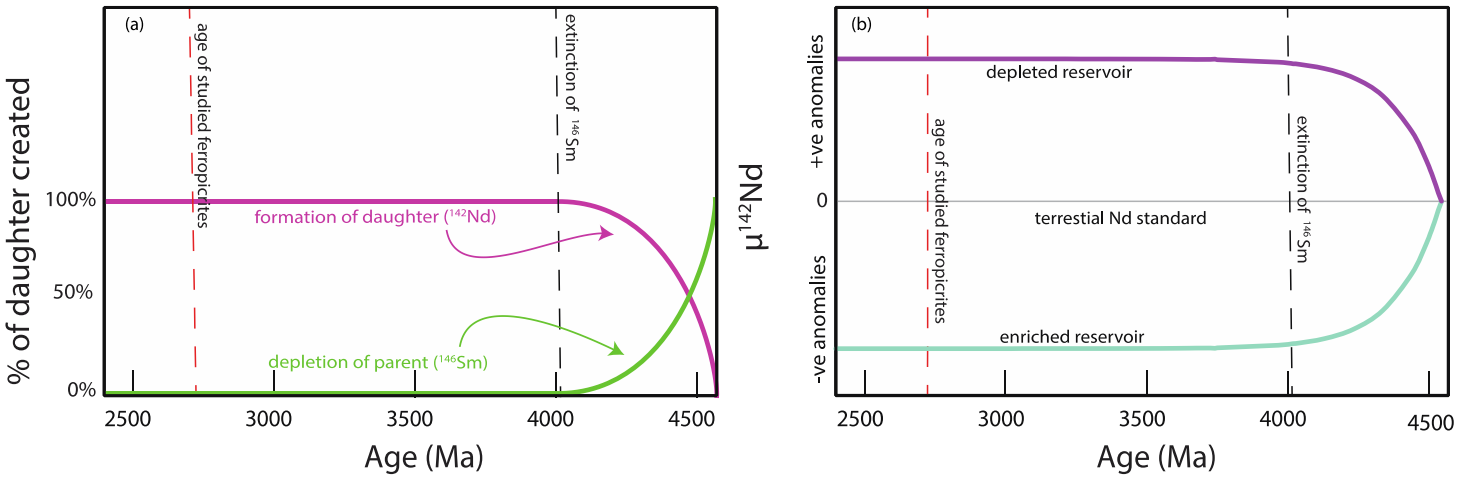

Figure 4.4: (a) ^{146}Sm decays to ^{142}Nd until ~500 Ma after Solar System formation. At this point, ^{146}Sm becomes undetectable. (b) Fractionation events solely taking place during the Hadean will form reservoirs with ^{142}Nd/^{144}Nd variations (or μ^{142}Nd values, which are deviations from the terrestrial standard).

The deviation of the ^{142}Nd/^{144}Nd ratio from the Nd terrestrial standard is expressed as μ^{142}Nd values, which are differences in parts per million and is calculated as:

$$\mu^{142}Nd = \left(\frac{\left(\frac{^{142}Nd}{^{144}Nd}\right)_{sample}}{\left(\frac{^{142}Nd}{^{144}Nd}\right)_{standard}} - 1 \right) * 10^6$$

Differentiation events occurring during the Hadean will form complementary Nd-enriched and Nd-depleted reservoirs that will continue to evolve until the extinction of ^{146}Sm (~4.0 Ga) to variable μ^{142}Nd values (Figure 4.4b). Such differentiation events can be early crust-mantle differentiation processes, which will form an enriched crust characterized by μ^{142}Nd<0 and a depleted mantle reservoir with μ^{142}Nd>0 (Figure 4.4b). Early magma ocean crystallization events will also fractionate the Sm/Nd ratio creating depleted and enriched mantle reservoirs.

Post-Hadean differentiation events, after the extinction of ^{146}Sm, will form enriched and depleted reservoirs characterized by the same $\mu^{142}Nd$ values. Therefore, any rock or reservoir younger than 4 Ga, but with a $\mu^{142}Nd$ that deviates from the terrestrial standard has to have acquired its ^{142}Nd isotopic composition from a source produced during the Hadean.

4.2 Hf-W isotope systematics

Another extinct chronometer that has been utilized to study early Earth processes is the ^{182}Hf-^{182}W isotopic system. The short-lived ^{182}Hf decayed to ^{182}W, with a half-life of 8.9 Ma, allowing it to be a powerful tool to study events occurring within the first 50 Ma of Earth's history. The difference in chemical behaviour between the lithophile parent (^{182}Hf) and siderophile daughter (^{182}W) in metal-silicate fractionation events results in Hf preferentially partitioning into the silicate portion during events such as formation of the core, with W going into the metallic portion (Figure 4.5).

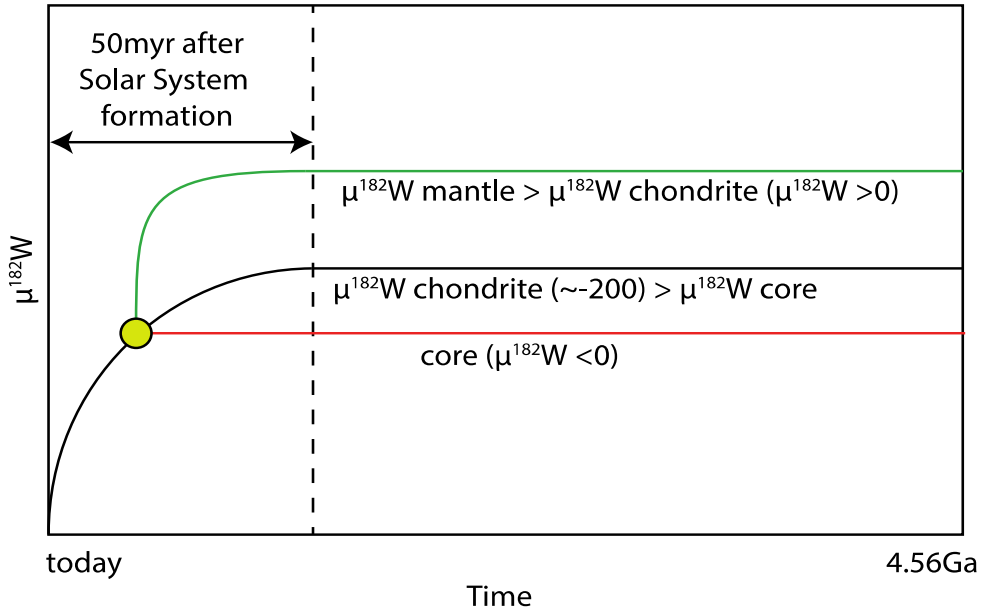

Figure 4.5: Fractionation of Hf/W whilst 182Hf was still extant. Metal-silicate fractionation events will result in the entire available W partitioning into the core, and Hf being preferentially retained in the mantle. After such events, the core essentially contains no Hf (thus no 182Hf) and μ182W will not change. However, since 182Hf is retained in

the mantle, decay to 182W will continue until it is extinct, causing the μ182W of the mantle to increase compared to chondrite.

Measurements of ^{182}W are relative to the stable ^{184}W and can be expressed as $\mu^{182}W$ notation. This notation reflects parts per million deviations of the $^{182}W/^{184}W$ ratio of samples from the W terrestrial standard ($\mu^{182}W=0$) using the following equation:

$$\mu^{182}W = \left(\frac{\left(\frac{^{182}W}{^{184}W}\right)_{sample}}{\left(\frac{^{182}W}{^{184}W}\right)_{standard}} - 1 \right) * 10^6$$

Furthermore, W is more incompatible than Hf during silicate differentiation events, and therefore the ^{182}Hf-^{182}W system is also useful to study early silicate-silicate fractionation events. If a silicate differentiation event were to occur whilst ^{182}Hf is still extant, a depleted reservoir, characterized by a high Hf/W ratio and an enriched reservoir, characterized by a low Hf/W ratio will be formed (Figure 4.6). The ^{182}Hf will continue to decay within these reservoirs until it is no longer extant, leading to an enriched reservoir with lower $\mu^{182}W$ values compared to the depleted reservoir. If a differentiation event were to occur after the extinction of ^{182}Hf, the $\mu^{182}W$ of both reservoirs will be that of their source.

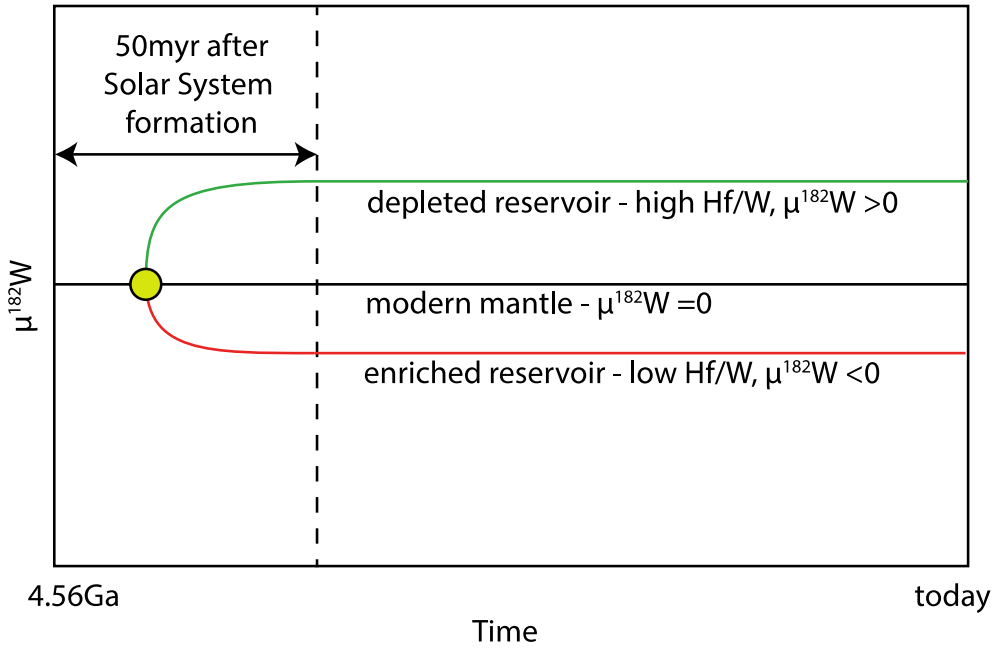

Figure 4.6: Fractionation of Hf and W in the mantle, the depleted reservoir will preferentially incorporate Hf, evolving to a higher μ182W, the enriched reservoir, with a lower Hf/W ratio will evolve to a lower μ182W than its source.

5.0 Methods

This section details the methods that were followed for sample collection and preparation for W concentration analysis and isotopic analysis. The detailed procedures for whole-rock major and trace element analysis can be found in Appendix A and B respectively. The chromatographic column separation procedures followed for determination of W-concentrations and for ^{147}Sm-^{143}Nd, ^{142}Nd and ^{182}W analyses are found in Appendix C.

5.1 Rock Sample Collection

Sample collection occurred in the summer of 2017 and took place in Pukaskwa National Park in Northern Ontario. A total of 61 samples were collected, from all lithologies of the PPH (Figure 5.2), sample locations can be found in Appendix D.

Whilst in the field, sample collection was undertaken to note surrounding geological features, and to collect samples that were as fresh as possible. A variety of each lithology was collected to ensure that we had a representative rock collection for analysis. All 61 samples were analyzed for major and trace element concentrations, 29 were analyzed for W concentrations by isotopic dilution, 19 for ^{147}Sm-^{147}Nd, 15 of which were also analyzed for ^{142}Nd, and 5 for ^{182}W.

5.2 Sample preparation for petrography

Polished thin sections were prepared for all samples at the University of Ottawa. Cut slabs (~ 5 cm x 3 cm x 2 cm) were used to make thin sections at the University of Ottawa rock preparation facilities. The slabs were chosen to be representative of the sample, in order to be able to gain insights into the various lithologies of the PPH sequence.

5.3 Preparation of sample powders for whole-rock geochemical and isotopic analysis

In preparation for geochemical and isotopic analysis rock samples were reduced to powder through a number of steps, which removed the weathered surfaces, veining and sulphides, and reduced the overall impacts of possible sample contamination by the tools used to during the powdering process. These precautions were taken since we would be analyzing selected samples for W concentrations at the ppb level. Since steel from a hammer or a jaw crusher can have W concentrations up to wt. % level, having any metal residue could result in W contamination of the samples. The samples were first cut with a diamond-bladed rock saw to remove weather edges, veining and sulphides. Samples were cut into ~1cm thick slabs and visually inspected for any remaining weathering, veining or sulphides, which was cut out if

observed. Slabs were then sanded with silicon carbide sandpaper to remove metal marks left by the saw and washed in an ultrasonic bath for 15 minutes to remove the dust.

The cleaned rock slabs were then wrapped in plastic and broken in <2 cm sized pieces using a plastic hammer. These pieces were visually inspected for any weathering, sulphides or veining was picked out, or sanded out if found. The pieces were then crushed to < 0.5 cm in size using a ceramic jaw crusher. Several precautionary steps were taken in order to reduce the effects of contamination between samples. Prior to the sample being crushed, the jaw crusher was pre-contaminated with some of the same sample that was to be crushed. Between crushing samples, the crusher jaws, ceramic sides, lid, and collection box was washed and dried using ethanol and compressed air. If sample residue remained on the crusher jaws, sandpaper was used to clean these residues and the jaws were then washed.

A ceramic ring mill was used in the final step to reduce crush to powder. The ring mill was cleaned after each use by powdering silica sand, then rinsing the ring mill water and drying it with compressed air and ethanol. The ring mill was pre-contaminated with some sample crush before each samples, this was discarded and the ring mill was cleaned prior to powdering the sample that would be used for geochemical analysis.

5.4 Sample preparation and W concentration analysis via isotope dilution

A selection of 29 samples of varying lithologies were analysed for their W concentrations. These samples were selected to represent a spread of the major and trace element chemistry and lithology of samples collected. Two USGS geo-reference materials BCR-2 and BHVO-2 were also analysed for their W concentration. All tungsten concentrations were determined using an isotope dilution method with a spike enriched in ^{186}W.

About 100 mg of sample with added spike solution were dissolved in a 5:1 ratio of concentrated HF:HNO_3. Samples were dissolved in capped 15 mL Savillex Teflon beakers, placed on the hotplate at 80°C for 3 days, before being cooled and opened. 2 mL of 7M HNO_3 was added to each beaker, and the beakers placed on the hotplate to evaporate to dryness at 80°C. Once dry, several drops of concentrated HNO_3 was added to each beaker and allowed to dry down at 90°C – this was repeated 4-5 times until the samples had turned a rusty brown colour. Samples were dissolved in 6M HCl, the beakers sealed and placed on the hotplate at 80°C for 1-2 days, before being cooled, opened and evaporated to dryness.

The W separation protocol used is similar to the one reported by Nagai & Yokoyama (2014) and only the main steps are mentioned here. Before column chromatography, samples were dissolved in 5 mL of 0.5M HF and centrifuged. Insoluble fluorides (e.g. MgF and CaF) that could bond with W, are removed in this step. The supernatant was extracted and dried down at 80°C. Samples were then dissolved in 1 mL of 0.4M HCl – 0.5M HF and centrifuged prior loading them into columns filled with an anion resin AG1-X8, 200-400 mesh. Tungsten was eluted from the resin in 10 mL of 9M HCl – 1M HF. The eluted samples were then dried down on a hotplate before being treated with aqua regia 4-5 times to remove any traces of Os, which has isobaric interferences with W. The full column procedure can be found in Appendix C, Table C1.

Samples were analyzed using the Agilent 8800 ICP-MS QQQ of the Geochemistry Core Facility of the University of Ottawa. Samples were dissolved in 2 mL of 0.5M HNO_3 + traces of HF to ensure W remains in solution. Data acquisition was conducted using sample-standard bracketing, where a W standard was measured every 3 samples and used to apply fractionation

corrections to the samples. Each W measurement represents the average of 30 replicates and 10 sweeps per replicate. In addition to measuring all W isotopes (^{180}W, ^{182}W, ^{183}W, ^{184}W and ^{186}W), ^{47}Ti, ^{178}Hf, and ^{189}Os were also measured to correct for isobaric interferences and monitor the cleanliness of chemistry.

Two geo-reference standards, BHVO-2 and BCR-2 were dissolved and analyzed under the same conditions as the samples. The W concentration obtained for BHVO-2 during the analytical session was 228±6 ppb, consistent with literature results between 192-240 ppb (Arevalo and McDonough, 2008; Babechuk et al., 2010; Stoll et al., 2008; Konig et al., 2008; Jochum et al., 2005; Shaheen et al., 2008). Our result for the BCR-2 yielded 515±24 ppb W, which falls between the average W concentration of 550±6 ppb reported by Arevalo and McDonough (2008) and 465±5 ppb W reported in Jochum et al. (2005).

5.5 ^{147}Sm-^{143}Nd sample preparation and analytical methods

In preparation for ^{147}Sm-^{143}Nd isotopic analysis, enough sample powder was weighed out for sample dissolution to ensure 300 ng of Nd, and a mixed spike of ^{150}Nd-^{149}Sm was added. Samples were digested in Savillex Teflon beakers using a 5:1 ratio of concentrated HF:HNO_3, which were then sealed and placed on the hot plate at 125°C for 4 days. The beakers were then opened and evaporated to dryness. Samples were then re-dissolved in 6M HCl, capped, and placed on the hotplate at 125°C for 2 days, after which 1-2 drops of H_3BO_3 were added to dissolve any remaining fluorides. Samples were placed on the hotplate and evaporated to dryness.

Samarium and Nd extraction procedures used here are similar to the ones reported in Pin and Zalduegui (1997), and only the main steps are described here (the full analytical procedure is found in Appendix C, Table C2). The LREE fraction was extracted from the dissolved rocks using a first set of columns filled with 2 mL of a cation resin AG50W-X8 200-400 mesh. Prior to the sample being loaded onto the column, the resin was conditioned using 20 mL of 2M HCl. The sample was centrifuged and then loaded onto the column in 2 mL of 2M HCl. Iron and other rock matrix elements are eluted with 18 mL of 2M HCl, and 10 mL of 2.5M HCl. The LREE fraction is collected in 10 mL of 6M HCl and dried down on the hotplate.

A second quartz column filled with 300 mg LN spec resin (50-100 µm) was used to separate the Sm and Nd from the LREE fractions. The full column protocol is detailed in Appendix C, Table C3. The columns were conditioned prior to the samples being loaded in 0.25 mL of 0.2M HCl. After the sample was loaded the columns were rinsed, and the Nd fraction collected in 5.5 mL of 0.2M HCl, and the Sm fraction in 3.5 mL of 0.5M HCl in separate beakers. The samples were placed on the hotplate to dry down.

Samarium and Nd fractions were analyzed at the Isotope Geochemistry and Geochronology Research Centre (IGGRC) at Carleton University, Ottawa, on a *Thermo-Fisher Triton* Thermal Ionization Mass Spectrometer (TIMS). Samples were dissolved in 1.5M HCl and loaded onto previously outgassed double Re filaments. Samarium standards and the Nd standard JNdi-1 were also loaded into the filaments and measured at the same time as the samples. Data acquisition was measured in static mode with the cup configurations shown in Table 5.1 for Nd and Table 5.2 for Sm.

L4	L3	L2	L1	C	H1	H2	H3	H4
-	^{143}Nd	^{144}Nd	^{145}Nd	^{146}Nd	^{147}Sm	^{148}Nd	^{150}Sm	-

Table 5.1: Faraday cup configuration for Nd analysis using static mode.

L4	L3	L2	L1	C	H1	H2	H3	H4
^{146}Nd	^{147}Sm	^{148}Sm	^{149}Sm	^{150}Sm	^{152}Sm	^{154}Sm	^{155}Gd	-

Table 5.2: Faraday cup configuration for Sm analysis using static mode.

During the Nd analysis, ^{147}Sm was monitored to correct for isobaric interferences on Nd isotopes, and in the Sm analysis ^{155}Gd and ^{146}Nd were monitored to correct for isobaric interferences on Sm isotopes. Each Nd isotope measurement is the average of 140 ratios (7 blocks of 20 ratios) using an integration time of 8.39 seconds. Peak centre and lens focus were performed every 4th block. Samarium isotope data is the average of 100 ratios, collected with an integration time of 8.39 seconds.

Isotope data was corrected for instrumental mass bias fractionation using an exponential law and a ^{146}Nd/^{144}Nd = 0.7219 for Nd isotope ratios and ^{147}Sm/^{152}Sm = 0.56081 for Sm isotope ratios. The JNdi-1 Nd standard yielded an average ^{143}Nd/^{144}Nd ratio of 0.512084 ± 2 (n=3) for the first analytical session and 0.512104 ± 5 (n=6) for the second analytical session. Both sessions yield average ^{143}Nd/^{144}Nd ratios lower than the ratio reported by Tanaka et al. (2000) of 0.512115 ±7, therefore, the data was corrected to account the difference. The difference in ^{143}Nd/^{144}Nd between the JNdi-1 standards analysed in both analytical sessions is due to the fact that all Faraday cups were replaced in between the sessions. The JNdi-1 ^{143}Nd/^{144}Nd ratio obtained from the new Faraday cups used for the 2nd analytical session is within error the values of Tanaka et al. (2000). Initial ε^{143}Nd and uncertainty were calculated following Fletcher

and Rosman (1982) and using CHUR values of $^{143}Nd/^{144}Nd$ = 0.51263 and $^{147}Sm/^{144}Nd$ = 0.196 (Bouvier et al. 2008)

5.6 ^{142}Nd sample preparation and analytical methods

Analysis of ^{142}Nd requires a high purification of Nd. Therefore, the separation of Nd for high-precision isotopic analysis is a four-step process, modified after Garçon et al. (2018) and Li et al. (2015). The complete sample dissolution and column chromatography is detailed in Appendix C, Table C3 to C6, and only the main steps are described here.

Samples are dissolved to extract ~ 1000 ng of Nd from the rocks and no spike is added. After the sample has been digested, the LREE fraction is separated in a first step using columns filled with 2 mL of the cation AG50W-X8 200-400 mesh resin. Step 2 removed Ce, since ^{142}Ce is an isobaric interference on ^{142}Nd. The LREE fractions were dissolved in HNO_3 with $NaBrO_3$ to oxidize Ce to a tetravalent state (Ce^{4+}), whilst the other REEs remain in a trivalent state (3+). The samples are passed twice through columns filled with 100-150 µm LN resin to ensure removal of Ce from the LREE portion. The samples were then dried down on the hotplate in preparation for step 3. In step 3, the samples are passed through columns filled with the cation AG50W-X8 200-400 mesh resin, similar to step 1, which removes the Na and Br introduced during step 2.

After samples were dried down, they went through the final step for Nd clean up. Step 4 column protocols efficiently removed Sm and any remaining Ce from the sample. Step 4 consists of 0.4 cm x 12 cm columns filled with fine-grained 20-50 µm LN resin, under N_2 gas pressure to speed up elution time. A 1% aliquot was taken from the final Nd fractions to

measure yields. With the exception of sample PW-027, yields were >60 %. Due to its low yield, sample PW-027 was not analyzed for ^{142}Nd.

Samples for high-precision Nd measurements were analyzed on the *Triton* TIMS at the IGGRC. Approximately 600 ng of samples were dissolved in 1.5N HCl and loaded onto zone-refined double Re filaments. The Nd standard JNdi-1 was also measured at the same time as the samples. Samples were analysed during two different sessions, in July 2018 and November 2018. Neodymium isotopes were measured using a two-line acquisition mode to dynamically obtain ^{142}Nd/^{144}Nd ratios. The dynamic mode allows for the application of corrections due to Faraday cup degradation through time. The Faraday cup configuration is detailed in Table 5.3.

	L4	L3	L2	L1	C	H1	H2	H3	H4
Line 1	^{140}Ce	^{141}Pr	^{142}Nd	^{143}Nd	^{144}Nd	^{145}Nd	^{146}Nd	^{148}Nd	–
Line 2	^{142}Nd	^{143}Nd	^{144}Nd	^{145}Nd	^{146}Nd	^{147}Sm	^{148}Nd	^{150}Nd	–

Table 5.3: Faraday cup configuration for ^{142}Nd data acquisition in dynamic mode using two lines.

In addition to measuring Nd isotopes, ^{140}Ce and ^{147}Sm isotopes were also measured in order to correct for isobaric interferences (Table 5.4).

Species	^{142}Nd	^{143}Nd	^{144}Nd	^{145}Nd	^{146}Nd	^{148}Nd	^{150}Nd
Mass	142	143	144	145	146	148	150
Interfering Species	^{142}Ce	/	^{144}Sm	/	/	^{148}Sm	^{150}Sm

Table 5.4: Interfering species of Ce and Sm isotopes on Nd isotopes

Each Nd measurement represents the average of 600 ratios collected in 25 cycles of 24 blocks, with 8.39 seconds acquisition time. A peak centre and lens focus was performed every 4th block. The amplifiers rotated in between blocks and a baseline of 30 seconds was measured between each block.

Data was treated offline, with corrections made for isobaric interferences. The instrumental mass bias fractionation for Nd isotope ratios was corrected using the exponential law to $^{146}Nd/^{144}Nd = 0.7219$. The data was dynamically integrated to obtain a $^{142}Nd/^{144}Nd$ ratio where the $^{142}Nd/^{144}Nd$ ratio of line 1 is corrected from mass fractionation using $^{146}Nd/^{144}Nd$ from line 2, in the same cups (L2 and C; see Table 5.3). These values are then statistically treated to remove outliers outside of two standard deviations. The JNdi-1 standard yielded an average $^{142}Nd/^{144}Nd$ ratio of 1.141837 ± 0.000005 (n=4) for the June 2018 analytical session and 1.141837 ± 0.000004 (n=9) for the November 2018 analytical session. Both averages are in perfect agreement with Garçon et al. (2018). $\mu^{142}Nd$ values for samples were calculated using the $^{142}Nd/^{144}Nd$ for the JNdi-1 standard analysed in the same analytical session.

5.7 ^{182}W sample preparation and analytical methods

The sample preparation protocol for ^{182}W isotopic analysis used here has been modified after Breton and Quitté (2014), and only the main steps will be described here. Appendix C, Table C8 and C9 outlines the detailed protocols used.

Enough sample to ensure the extraction of ~1000 ng of W from each sample was dissolved in 120 mL Teflon beakers, using 5 mL of concentrated HNO_3 and 25 mL of concentrated HF per 3 g of rock powder, capped, and placed on the hotplate at 100°C for 5 days. Samples were then opened and 5 mL of 7M HNO_3 added, and evaporated to dryness. This step ensures the preferential evaporation of HF before the HNO_3 and therefore avoiding the formation of fluorides that can incorporate W. Once dried, concentrated HNO_3 was added to each sample and evaporated, and this was repeated 3 times. After this, the samples were re-dissolved in 100

µL of concentrated HNO_3 + 30% H_2O_2, the beakers were sealed and placed on the hot plate for an hour, then opened and samples evaporated to dryness at 80°C. This step dissolves the organic matter from the samples. The samples were then re-dissolved in 20 mL of 6M HCl, capped, and placed on the hot plate for ~6 hours, and then evaporated. This step was repeated twice, and ensures further dissolution of fluorides.

Tungsten-separation was a three-step column procedure. The first column separates the high field strength elements (HFSE). The second column separated W from the collected HFSE fraction. A final clean up column ensures the purification of W.

Prior to being loaded onto the 20 mL AG50W-X8 resin, 200-400 mesh, samples were dissolved in 1M HCl-0.1M HF with 5 mL for every 1.2 g of sample dissolved. The column chemistry procedure can be found in Appendix C Table 12, with no more than 1.2 g of sample being loaded onto each column. The resin was equilibrated using 1M HCl-0.1M HF. Samples were dissolved in the loading acid and centrifuged for and loaded onto the resin. Due to the nature of the cationic nature of the columns, the HFSE elements were not retained and eluted and collected at this step. The centrifuge tubes were then rinsed with 5 mL of 1M HCl-0.1M HF, shaken, and centrifuged to ensure that no HFSE were retained in the resin, this was done a total of 3 times. Prior to being dried down, an aliquot of 1% or 4% of the collected cut was taken to test the yields. The resin was cleaned as detailed in Appendix C, Table C7.

The HFSE aliquot fraction was spiked and 3 mL of 1M HF was added to each sample before being capped and placed on the hot plate to homogenize for several days. Samples were dried down and cleaned up to separate the W fraction as per Appendix C. Chemistry yields for 10 out

the 11 fractions collected resulted in > 85%, except for one sample, PW-033a that yielded ~ 70%.

The unspiked HFSE fractions (97% to 99% of the total sample) were treated with HF-HCl dissolutions in order to remove any remaining fluorides. Samples were dissolved in 5 mL of 1M HF per 1 g of digested powder, capped, and placed on the hotplate overnight at 110°C. Samples were then centrifuged and supernatants were extracted from the samples. The residues were rinsed with ultrapure H_2O and centrifuged again, and supernatants were extracted. The remaining residue dissolved in 6M HCl (5 mL/g of powder) dried down. These steps were repeated 3 times in order to ensure complete extraction of W from the residue.

Samples were dissolved in 16.6 mL 0.6M HF – 0.33% H_2O_2 and loaded into columns filled with 10 ml of AG1-X8 resin 200-400 mesh, that were conditioned using 40 mL of 4M HCl-2M HF prior to sample loading. Samples were split over several columns in order to ensure no more than 1.8 g of dissolved powder per column to avoid oversaturation of the resin. The W fraction was eluted in 35 mL of 4M HCl - 2M HF, prior to the samples being dried down, 0.5 % (350 µL) of the sample was taken as an aliquot for yield analysis. Yields were analyzed at the University of Ottawa on the Agilent 8800 QQQ Triple-Quadrupole ICP-MS, and resulted in yields above 73 %.

The collected sample was dried down until about 10 mL remained, and transferred to 15 mL beakers and continued to dry down until <500 µL remained. At this point, 300 µL of concentrated HF was added to each beaker to ensure that W remained in solution, and the samples were dried until <100 µL remained. Another 300 µL of concentrated HF was added in preparation for the final column step.

The final column ensures that the eluted W-fraction in the previous column is cleaned from all remaining Ti, which inhibits the ionization of W during measurements. Samples were dried down on the day of the chemistry until ~20 µL remained, before being diluted in 1 mL of H_2O and 15 µL of H_2O_2 in preparation for loading. Columns containing 30 µL of AG1-X8 200-400 mesh were prepared on the day of chemistry.

Samples were loaded onto the columns, rinsed and the W was eluted in 4 mL of 4M HCl – 2M HF in clean 7 mL Teflon beakers. A 1% (40 µL) aliquot was taken to test for final yields in 5 mL centrifuge tubes, and diluted to 5 mL of 0.5M HNO_3 + traces of HF. W-yields were tested on the Agilent 8800 QQQ Triple-Quadrupole ICP-MS, and the yield results were between 77 % and 93 % (Table 5.5).

Sample Number	Theoretical W (ppb)	Measured W (ppb)	Yield W (%)
PW-009	1443	1193	83%
PW-012	1210	1126	93%
PW-015	1599	1322	83%
PW-023	1331	1094	82%
PW-033	1518	1165	77%
PW-038	1243	1093	88%
PW-039	1242	997	80%

Table 5.5: W-yields after the final column pass.

Collected samples were evaporated at 80 °C to almost dryness – samples are never completely dried down in order to avoid W being precipitated, which is hard to dissolve when dried down. When almost dried they were treated with a 3:1 concentrated HNO_3: HCl ratio, three times. 200 µL of 9M HF was added to each sample and dried down until <20 µL remained, and another 200 µL of 9M HF was added, and dried down until ~5 µL of sample remained.

Tungsten isotopic composition was measured as trioxide WO_3^- molecules in negative mode on the Triton TIMS at the Carleton University IGGRC. The procedure followed was slightly modified

from Archer et al. (2016). Tungsten samples (~1000 ng W) were loaded with 9M HF in previously outgassed zone-refined single Re filaments, together with 5 uL of La-Gd activator. Data acquisition was collected using a multi-static method with three lines of acquisition (Line 1, Line 2 and Line 3), with masses 232, 233 and 234 placed in the central cup, alternately. Table 5.6 details the three-line cup configuration used for these analyses. Faraday cups L4 to H2 were connected to amplifiers with 10^{11} Ω resistors, which were rotated between every block. H3 and H4 Faraday cups were connected to amplifiers with 10^{12}Ω resistors, in order to measure the low signals from $^{186}W^{16}O_2{}^{18}O$ and $^{187}Re^{16}O_2{}^{18}O$.

	L4	L3	L2	L1	C	H1	H2	H3	H4
Line 1	$^{194}PtO_2$	$^{181}TaO_3$	$^{182}WO_3$	$^{183}WO_3$	$^{184}WO_3$	$^{185}ReO_3$	$^{186}WO_3$	$^{186}W^{16}O_2{}^{18}O$	$^{187}Re^{16}O_2{}^{18}O$
Line 2	$^{195}PtO_2$	$^{182}WO_3$	$^{183}WO_3$	$^{184}WO_3$	$^{185}ReO_3$	$^{186}WO_3$	$^{187}ReO_3$	$^{187}Re^{16}O_2{}^{18}O$	$^{190}OsO_3$
Line 3	$^{180}WO_3$	$^{183}WO_3$	$^{184}WO_3$	$^{185}ReO_3$	$^{186}WO_3$	$^{187}ReO_3$	$^{186}W^{16}O_2{}^{18}O$	$^{190}OsO_3$	$^{191}IrO_3$

Table 5.6: Faraday cup configuration for data acquisition utilizing 9 Faraday cups, unless specified it is ^{16}O.

Each sample measurement represents the average of 560 cycles, each consisting of 28 blocks of 20 cycles (~12h of analysis). Integration time for the Line 1 was 33.55 seconds in order to obtain a good signal for the low intensities (~ 6mV) of $^{186}W^{16}O_2{}^{18}O$ and $^{187}Re^{16}O_2{}^{18}O$, and 8.39 seconds in Line 2 and 3. An idle time of 12 seconds for Line 1, and 4 seconds for Line 2 and 3 was conducted before each line was measured. A peak centre and lens focus was performed every three blocks, and baselines of 1200 seconds (~20 min) were measured every 7 blocks.

Species	$^{180}W^{16}O_3^-$	$^{181}Ta^{16}O_3^-$	$^{182}W^{16}O_3^-$	$^{183}W^{16}O_3^-$	$^{184}W^{16}O_3^-$	$^{185}Re^{16}O_3^-$	$^{186}W^{16}O_3^-$	$^{187}Re^{16}O_3^-$	$^{186}W^{16}O_2{}^{18}O^-$	$^{187}Re^{16}O_2{}^{18}O^-$	$^{190}Os^-$
Mass	228	229	230	231	232	233	234	235	236	237	238
Interfering Species	/	$^{180}W^{49}O_3^-$	$^{180}W^{50}O_3^-$	$^{180}W^{51}O_3^-$	$^{180}W^{52}O_3^-$	$^{180}W^{53}O_3^-$	$^{180}W^{54}O_3^-$	/	/		/
	/	/	$^{181}Ta^{49}O_3^-$	$^{181}Ta^{50}O_3^-$	$^{181}Ta^{51}O_3^-$	$^{181}Ta^{52}O_3^-$	$^{181}Ta^{53}O_3^-$	$^{181}Ta^{54}O_3^-$	/		/
	/	/	/	$^{182}W^{49}O_3^-$	$^{182}W^{50}O_3^-$	$^{182}W^{51}O_3^-$	$^{182}W^{52}O_3^-$	$^{182}W^{53}O_3^-$	/		/
	/	/	/	/	$^{183}W^{49}O_3^-$	$^{183}W^{50}O_3^-$	$^{183}W^{51}O_3^-$	$^{183}W^{52}O_3^-$	/		/
	/	/	/	/	/	$^{184}W^{49}O_3^-$	$^{184}W^{50}O_3^-$	$^{184}W^{51}O_3^-$	$^{184}W^{52}O_3^-$		$^{184}W^{54}O_3^-$
	/	/	/	/	/	/	$^{185}Re^{49}O_3^-$	$^{185}Re^{50}O_3^-$	$^{185}Re^{51}O_3^-$		$^{185}Re^{53}O_3^-$
	/	/	/	/	/	/	/	$^{186}W^{49}O_3^-$	/		$^{186}W^{52}O_3^-$
	/	/	/	/	/	/	/	/	$^{187}Re^{49}O_3^-$		$^{187}Re^{51}O_3^-$

Table 5.7: Isobaric oxides that interfere with W species. Oxygen isotopic compositions are the sum of the total oxygen masses.

The raw tungsten isotope data were treated offline, where corrections for isobaric interferences, oxides and fractionation are preformed. Given that tungsten isotopes are measured as trioxide species, these species can be combined with the different isotopes (^{16}O, ^{17}O and ^{18}O) causing multiple isobaric interferences (Table 5.7). For example, the $^{182}W^{16}O_3^-$ molecule has a mass of 230, which is also the same mass as the $^{180}W^{16}O_2{}^{18}O^-$ molecule. These interferences can be corrected by estimating the probability of combination of the various O isotopes with W, using their respective abundances (e.g. trioxide species with ^{16}O have high probabilities since the abundance of ^{16}O is 99.762%). Oxide species are then corrected for oxygen fractionation, where the $^{18}O/^{16}O$ ratio is obtained using measured $^{186}W^{16}O_2{}^{18}O$ over $^{186}W^{16}O_3$, and the $^{17}O/^{16}O$ ratio was estimated from the oxygen fractionation slope of 0.0954 (Archer et al. 2017). Nier (1950) oxygen isotope compositions were not used here, since oxygen seems to fractionate differently during TIMS analyses (e.g. Archer et al. 2017). Metal W ratios are then obtained from the measured $^{x}W^{16}O_3^-$ molecules, e.g. $^{182}W^{16}O_3^-$ over $^{184}W^{16}O_3^-$ gives the $^{182}W/^{184}W$ ratio. The $^{182}W/^{184}W$ and $^{183}W/^{184}W$ ratios were then corrected for mass fractionation using $^{186}W/^{184}W = 0.92767$ (Lee, 1995), and data from Line 1 and Line 2 for each cycle are averaged in a multistatic mode. The Alfa Aesar W standard was measured repeatedly

during analytical sessions and yielded a $^{182}W/^{184}W$ ratio of 0.864892 ± 0.000004 (n=7, 2SE), corresponding to a reproducibility of 5.93 ppm. This $^{182}W/^{184}W$ ratio is in agreement with reported values for the same W standard (Archer et al., 2017).

6.0 Results

6.1 Hand sample and thin section petrology

The petrology of the PPH volcanic sequence was described in detail by Kitayama and Francis (2014). The samples collected for this study targeted all the lithologies present, which includes the ferropicritic intrusive rocks, the Fe-rich lavas and the tholeiitic rocks (Figure 2.2, 2.3). Only a brief description of the petrology of the various samples is presented here. Sample locations and associated lithology – intrusive rocks: peridotite, dunite, green clinopyroxenite, black clinopyroxenite, or gabbro, lavas: Fe-rich and tholeiite – names are in Appendix C.

The underlying mafic tholeiitic volcanic rocks are commonly fractured, and fresh surfaces are hard to find in the field, however, pillow textures are easily identifiable. There is the presence of thin quartz and carbonate veins throughout the tholeiitic unit. The tholeiites are fine-grained, green in colour – both on the fresh and weathered surface. They are composed of minor plagioclase, hornblende and subordinate chlorite, epidote and opaque minerals.

The ultramafic rocks can be classified as peridotites, dunites and clinopyroxenites. At the base of the intrusive sequence, the dunites and peridotites are composed of heavily serpentinized olivine, pyroxene and secondary magnetite and sulphides.

There are two types of clinopyroxenites, which can be distinguished by their colour; the black clinopyroxenites and the green clinopyroxenites. The green clinopyroxenites are composed of

minor pseudomorphic serpentine, elongated amphibole minerals (1-3 cm in length), which have replaced the clinopyroxenes, and some minor Fe-oxides, veining is also present in this unit. The black clinopyroxenites are generally the best-preserved intrusive lithology, although some minor veining. They are composed of elongate amphibole minerals (1-7 cm in length), with relict clinopyroxene still present. Within the black clinopyroxenites, minor sulphides and oxides are present in greater concentration compared to other units. The gabbros are composed of coarse-grained amphibole and plagioclase, with minor Fe-oxides.

The Fe-rich lavas are black in colour, fine grained, and appear to be better preserved, compared to the tholeiites, primary pillow textures are also apparent. The Fe-rich lavas are primarily composed of hornblende with minor amounts of plagioclase feldspar. At the base of the lavas, as the transition from the gabbros or black clinopyroxenites occurs, elongate amphibole crystals (up to 5 cm in length) are present with no preferred orientation.

The primary igneous mineralogy of the PPH rocks is mostly replaced by greenschist facies minerals and most ultramafic rocks have undergone serpentinization. Figure 6.1 shows the calculated CIPW normative of the lavas and intrusive rocks in order to have a better understanding of their primary mineralogy and compare the intrusive and volcanic rocks with variable degrees of serpentinization and metamorphic mineral replacement. The normative mineralogy of the PPH rocks is mostly qualitative since their whole-rock chemical composition has been affected to some extent by post-magmatic processes. This is indicated by the normative hypersthene of some ultramafic rocks interpreted by Kitayama and Francis (2014) to be cumulates derived from a mildly alkaline primary magma. They attributed this to the serpentinization of olivine and subsequent loss of Mg, affecting the calculated normative

mineralogy. Nevertheless, the different lithologies are well discriminated on a normative pyroxene-plagioclase-olivine ternary diagram (Figure 6.1). The normative mineralogy of the tholeiites is mostly composed of plagioclase and pyroxene with only a few samples exhibiting minor amounts of normative olivine, compared to the ferropicritic samples which have variable amounts of olivine (Figure 6.1). The dunites and peridotites are dominated by normative olivine and pyroxene with subordinate plagioclase (Figure 6.1), with the proportions of olivine increasing for the dunites. The clinopyroxenites and gabbros show variable amounts of normative pyroxene and plagioclase, with lesser amounts of normative olivine compared to the dunites and peridotites (Figure 6.1). Additionally, the relative proportions of normative pyroxene appear to decrease as plagioclase increase as the transition from green clinopyroxenite to black clinopyroxenite to the gabbro occurs (Figure 6.1). The Fe-rich lavas are similar in composition to the gabbros, plotting the field of olivine gabbros (Figure 6.1). The Fe-rich lavas can be distinguished from the tholeiitic lavas by their normative olivine content between 10-25%, whereas the tholeiites do not contain normative olivine except for a few samples with >5% olivine.

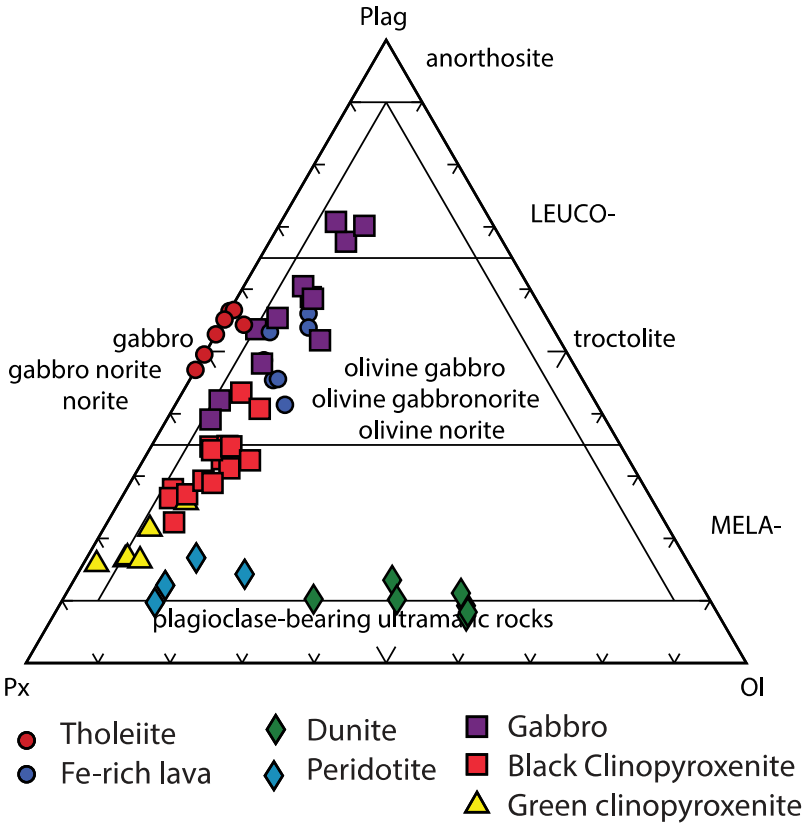

Figure 6.1: Normative mineralogy ternary diagram for the intrusive samples and over and underlying lavas.

6.2 Major and trace element geochemistry results

The geochemistry of the lithologies of the PPH have been described in detail in Kitayama and Francis (2014). This section shows the major (Appendix E) and trace element (Appendix F) element results for the rocks collected during this study.

The ferropicritic lavas and intrusive rocks display a wide variation of MgO content, from the dunites (~30 wt.% MgO) to the gabbros (<5 wt.% MgO). All the intrusive rocks and Fe-rich lavas display high Fe content with most samples between 16-24 wt.% FeO, except for a few green clinopyroxenites with FeO concentrations closer to ~13 wt.% (Figure 6.2).

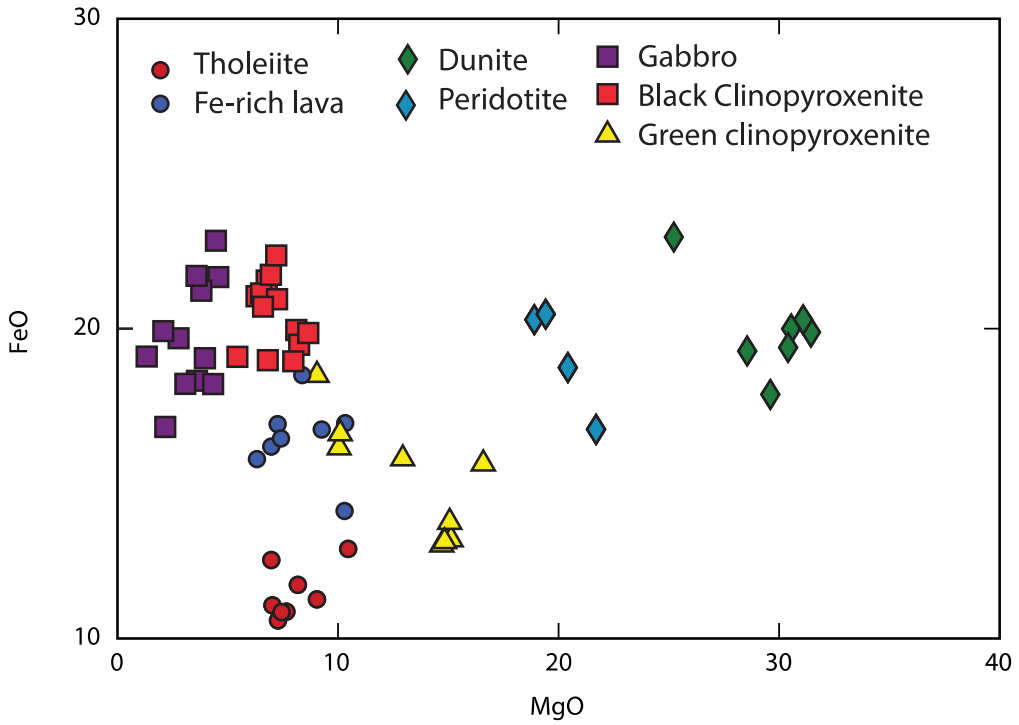

Figure 6.2: MgO (wt.%) vs. FeO (wt.%) plot for all 61 samples collected from the PPH sequence.

The sampled ferropicritic intrusive rocks follow the same fractional crystallization trend previously observed in Kitayama and Francis (2014). The CaO contents increase with decreasing MgO contents for the dunites and peridotites, and decrease for the clinopyroxenites and gabbros (Figure 6.3). The decrease in CaO content can be correlated with the amount of normative plagioclase and clinopyroxene. The whole-rock major element compositions for the Fe-rich intrusive rocks appear to be controlled by the fractionation of olivine for the dunites and peridotites, whilst clinopyroxene and plagioclase fractionation is the dominant process, which controls the compositions of the clinopyroxenites and gabbros.

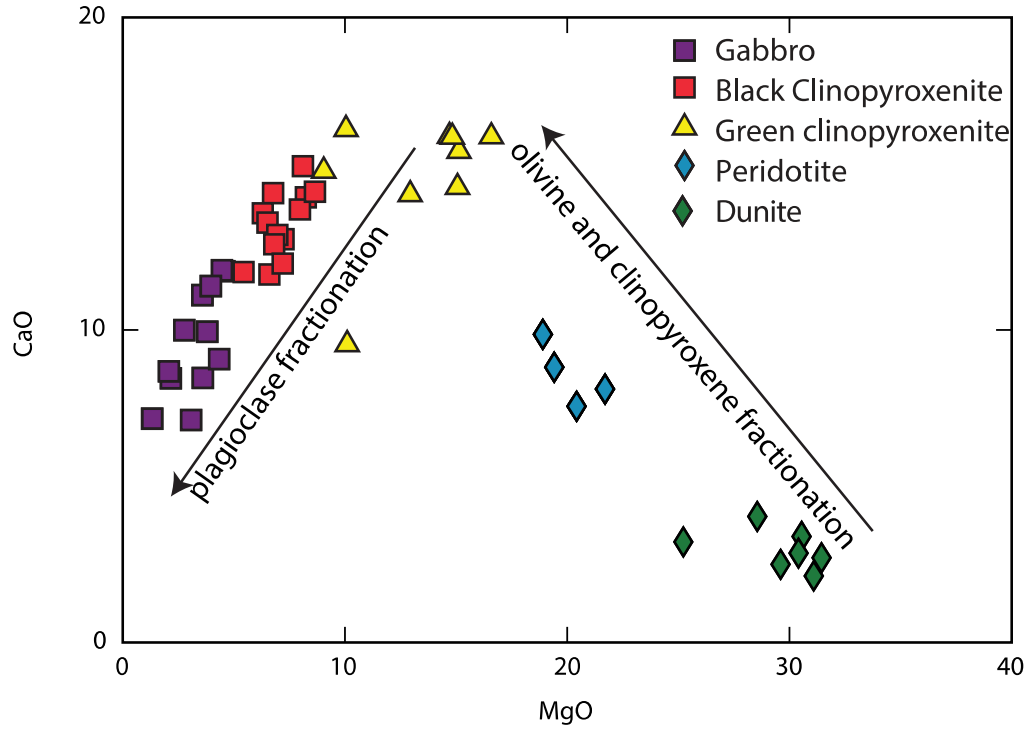

Figure 6.3: MgO (wt.%) vs. CaO (wt.%) plot for the intrusive samples

The tholeiitic rocks have similar MgO contents to the Fe-rich lavas, but lower FeO contents (10-13 wt.% FeO). On a total alkali vs. silica diagram the mafic Fe-rich rocks display lower SiO_2 content compared to the tholeiites and appear to fall on the side of alkaline compositions, as opposed to the subalkaline tholeiites that are basaltic in composition (Figure 6.4).

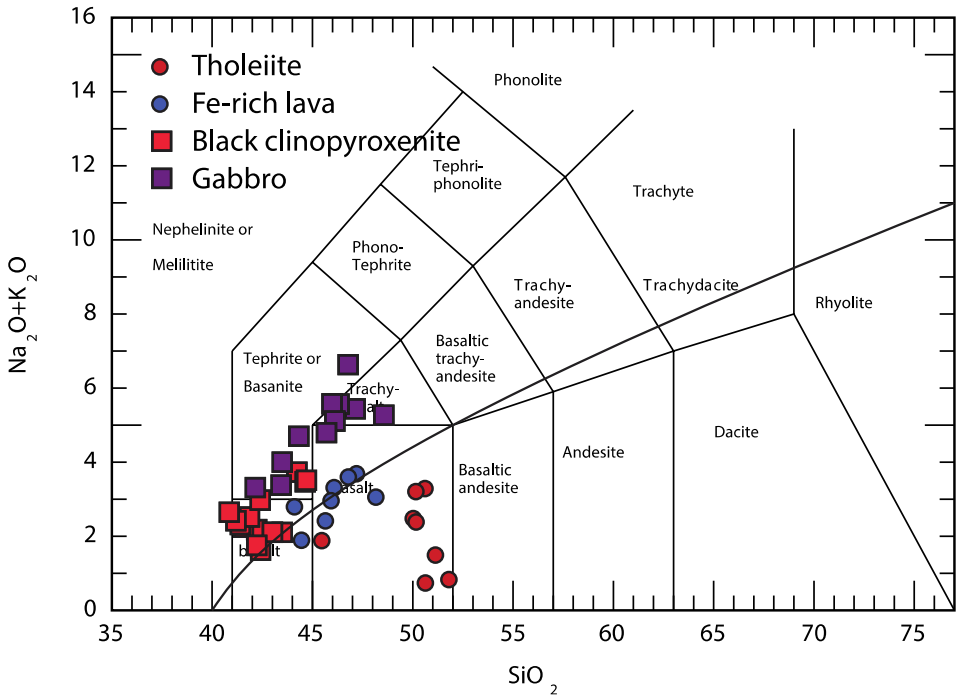

Figure 6.4: Total alkali vs. silica (TAS) diagram for lavas, and most evolved (black clinopyroxenite and gabbro) intrusive samples. Major element oxides are in wt.%.

The ferropicritic lavas overlap the alkaline-subalkaline divide and have been interpreted by Kitayama and Francis (2014) to have undergone contamination by the underlying subalkaline tholeiites, resulting in them not being as alkaline rich as the parental magma that gave rise to the Fe-rich intrusive rocks.

The trace element compositions of the ferropicritic samples collected are consistent with what was previously reported in Kitayama and Francis (2014). The Fe-rich intrusive rocks are highly enriched in incompatible trace elements and display LREE enriched profiles (Figure 6.5). The total REE concentrations display a general increase from dunites to gabbros, but with no systematic variations in their La/Sm ratios (Figure 6.6). The Fe-rich lavas also display slight LREE enrichments compared to the tholeiites, but with La/Sm ratios lower than most of the intrusive rocks (Figure 6.6). The tholeiites are characterized by flat REE profiles (Figure 6.5).

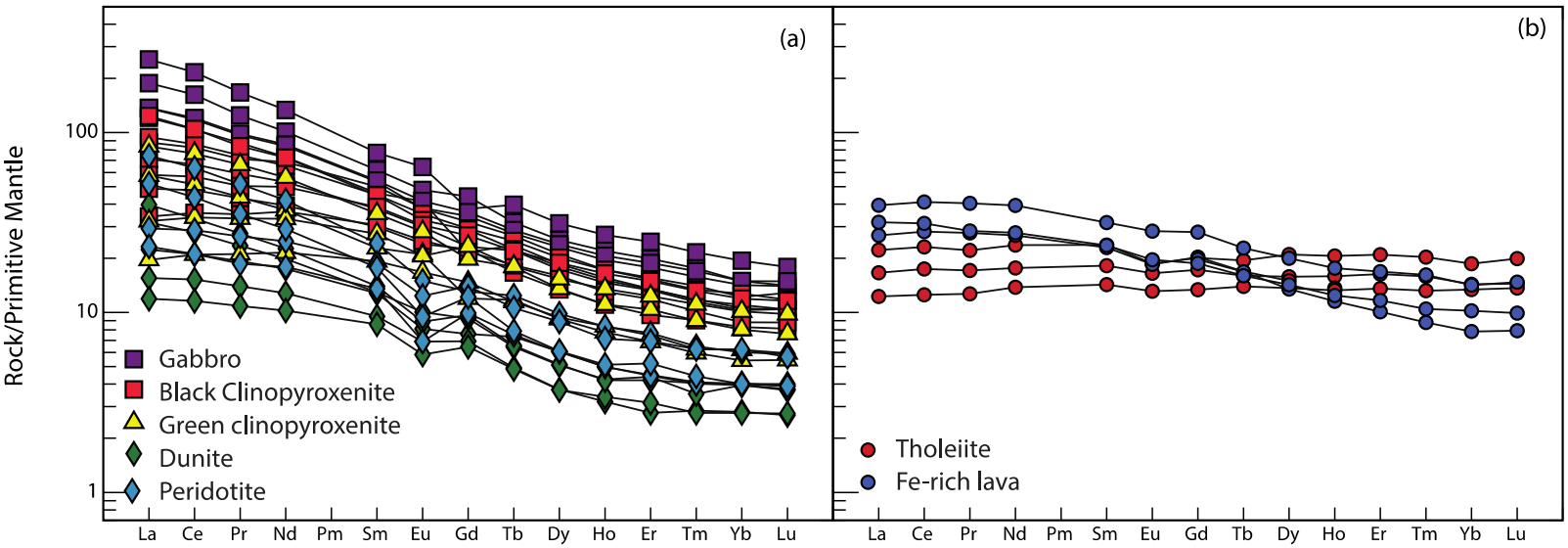

Figure 6.5: Chondrite-normalized rare earth element plot the (a) intrusive samples and (b) Fe-rich lavas and tholeiites. Only a subset of samples is shown for clarity, but they show the general trends for each lithologies. Chondrite values from Sun and McDonough (1989)

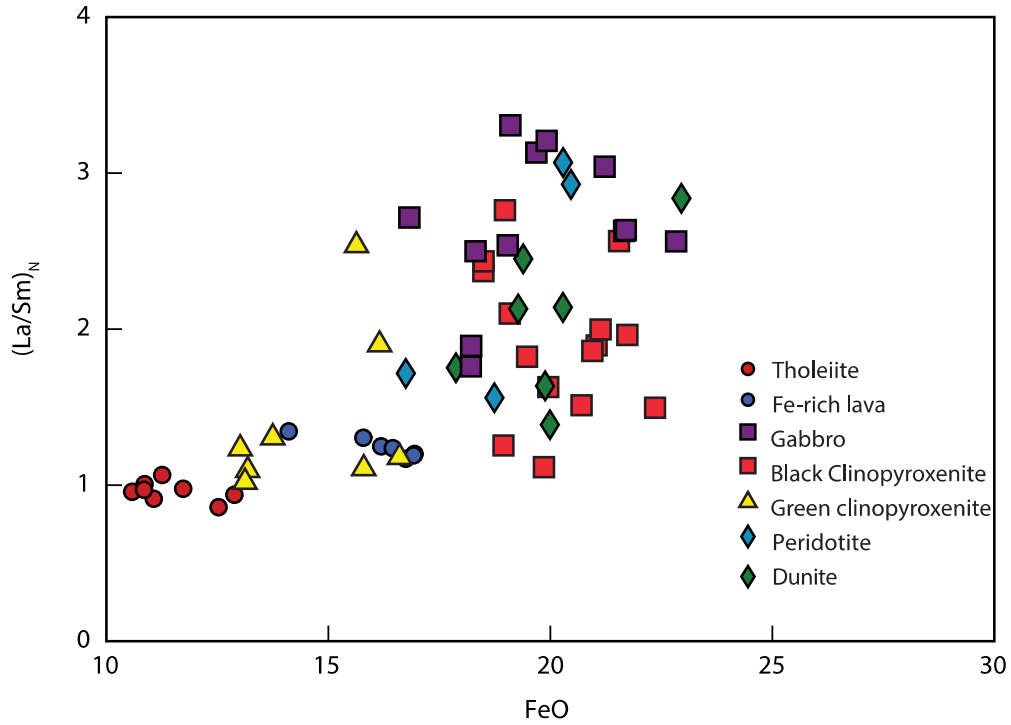

Figure 6.6: $(La/Sm)_N$ vs. FeO (wt.%) plot for all samples. Chondrite normalization values after Sun and McDonough (1989)

Tungsten is an incompatible element with similar behaviour as Th and U. In an unperturbed magmatic system, W concentrations should thus generally increase with differentiation. When plotted against MgO, which is an indicator of magmatic differentiation, no overall correlation was found (Figure 6.7).

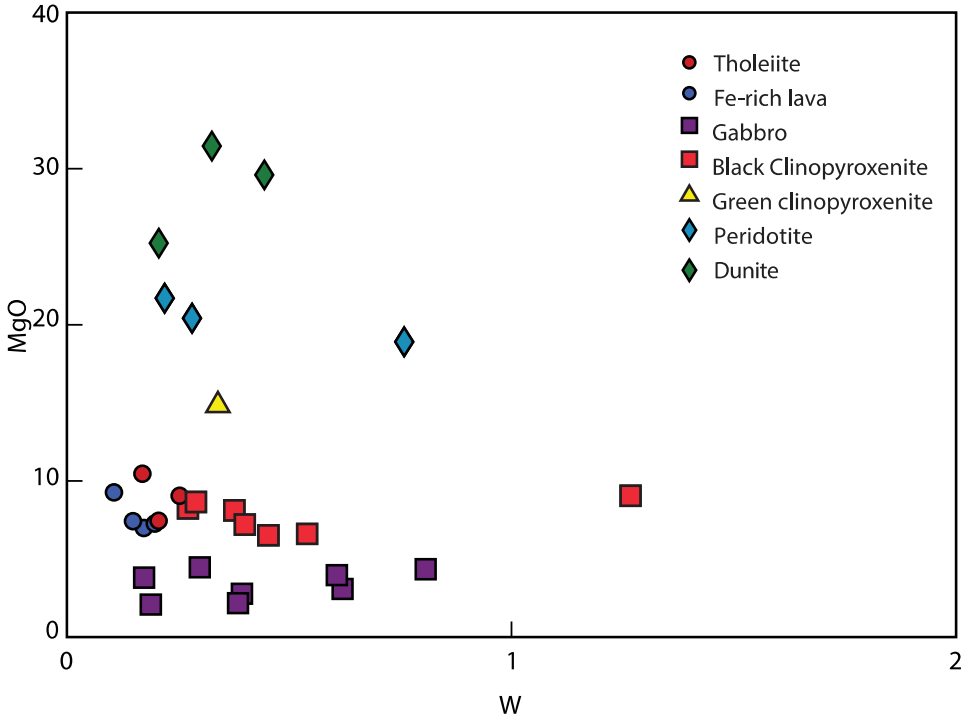

Figure 6.7: MgO (wt.%) vs. W (ppb) for the PPH sequence.

Tungsten, however, is also a fluid-mobile element and W/W* values (calculated using $W/W^*=W_N/\sqrt{(Th_N*U_N)}$) are used here in order to assess for possible enrichments or depletions relative to Th and U which have similar incompatibilities to W. Calculated W/W* values are plotted against U and Th (Figure 6.8). It appears that the W/W* ratio decreases as the intrusive samples evolve from ultramafic to gabbroic in composition. The tholeiitic lavas indicate homogeneity between W/W* and U or Th composition, whilst the Fe-rich lavas indicate some spread.

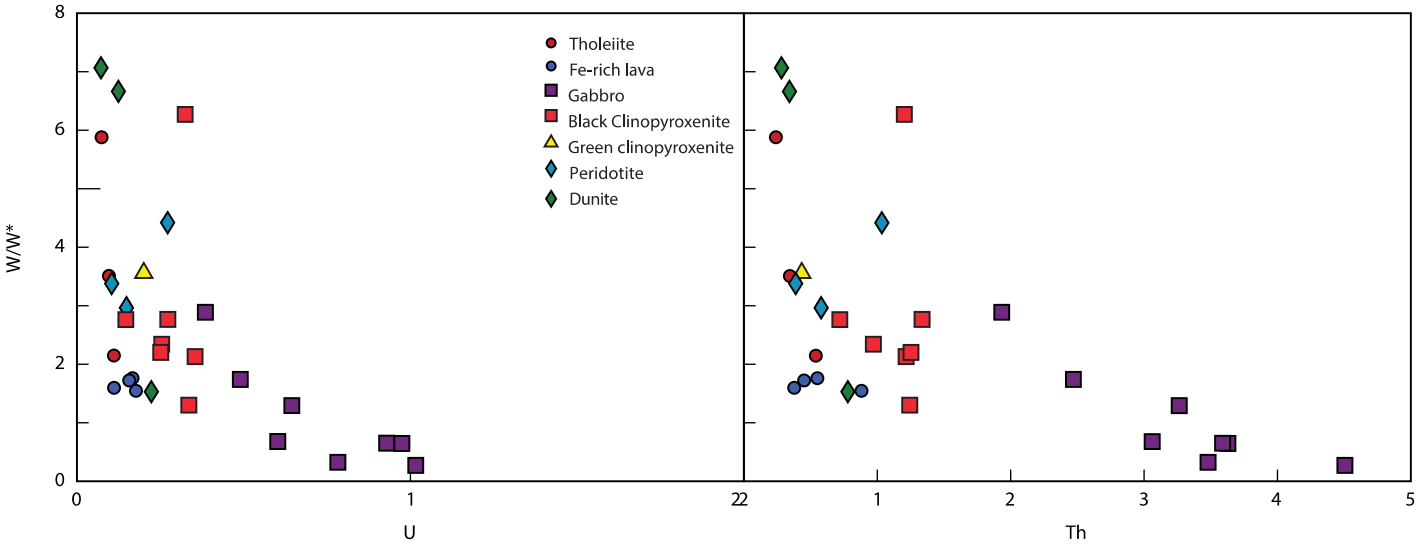

Figure 6.8: W/W* vs. U (ppm) (left) and Th (ppm) (right) plots for the 29 samples of varying lithologies which were analyzed for their W concentrations by isotopic dilution.

Furthermore, there is no correlation between W and U and Th, despite there being correlations between Nb and U and Th and U, which are trace element indicators of magmatic differentiation (Figure 6.9).

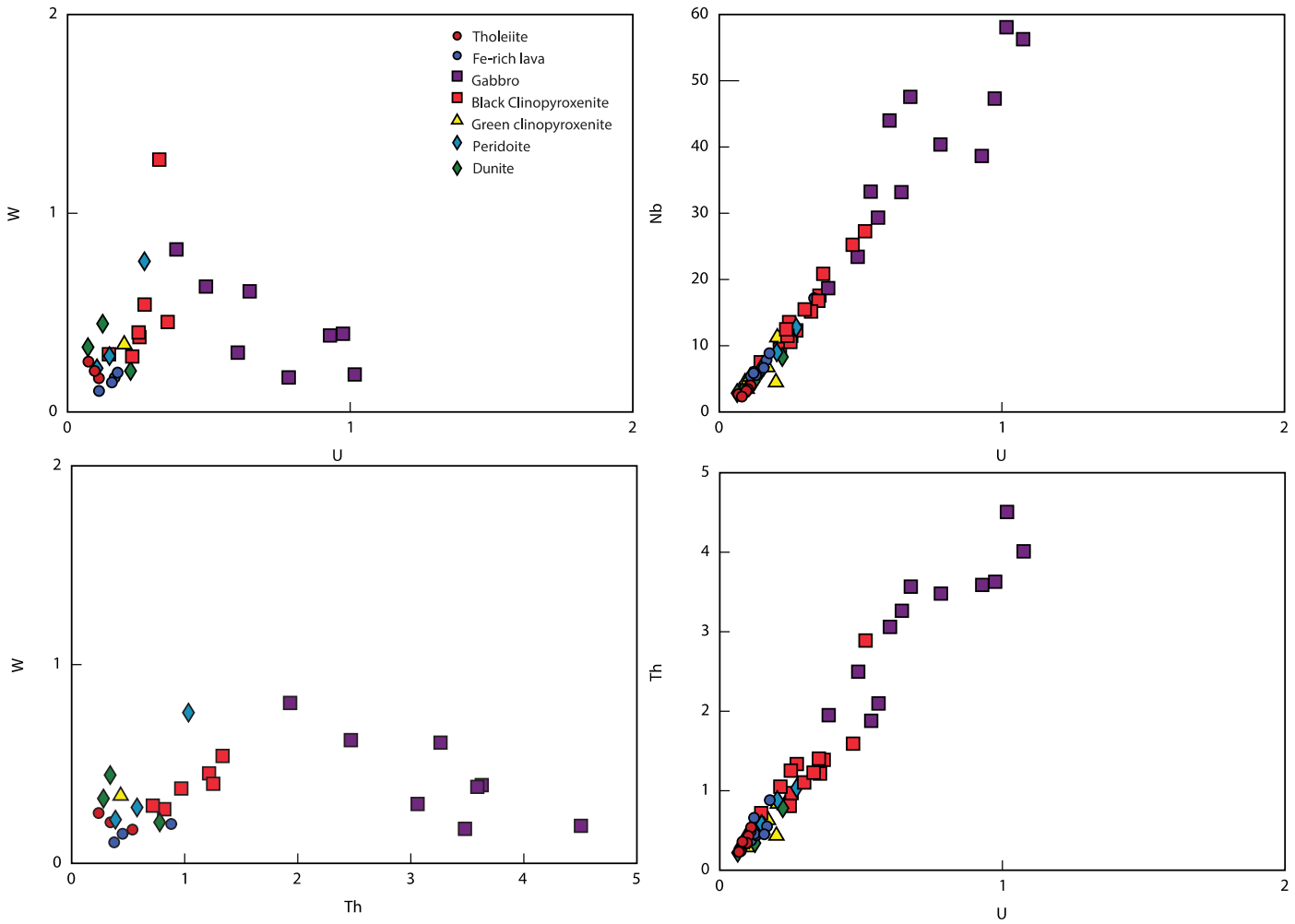

Figure 6.9 various trace element plots. A correlation exists between U (ppm) vs. Th (ppm) and U (ppm) vs. Nb (ppm), however, no correlation exists between W (ppm) and U or Th.

6.3 ^{147}Sm-^{143}Nd isotopic results

A total of 18 samples (with 6 duplicates that are different dissolutions) were analysed for their ^{147}Sm-^{143}Nd isotopic compositions. Samples were selected to cover a wide range of Sm/Nd ratios in order to obtain the most precise isochron possible. This included 3 tholeiites, 2 dunites, 1 peridotite, 1 green clinopyroxenite, 5 black clinopyroxenites, 4 gabbros, and 2 Fe-rich lavas. The ^{147}Sm/^{144}Nd ratios for the analyzed samples range from 0.1134 to 0.1911 with the

tholeiites having the highest $^{147}Sm/^{144}Nd$ ratios and the gabbros the lowest $^{147}Sm/^{144}Nd$ ratios. The $^{143}Nd/^{144}Nd$ ratios range from 0.511268 to 0.512642 and εNd values calculated at 2681 Ma are ranging from +1.7 to +3.2 (Table 6.1).

Sample	Lithology	[Nd] ppm	[Sm] ppm	$^{143}Nd/^{144}Nd$	2σ Error	$^{147}Sm/^{144}Nd$	$^{143}Nd/^{144}Nd_i$	εNd_i
PW-002	gabbro	62.08	11.64	0.511268	0.000003	0.1134	0.509238	2.3
PW-009	black cpx	29.50	6.59	0.511658	0.000005	0.1350	0.509241	2.3
PW-012	gabbro	46.56	9.27	0.511397	0.000005	0.1204	0.509241	2.4
PW-014	black cpx	26.70	5.53	0.511477	0.000004	0.1252	0.509236	2.3
PW-015	black cpx	21.04	4.80	0.511709	0.000004	0.1379	0.509240	2.3
PW-015*	black cpx	21.01	4.74	0.511710	0.000004	0.1365	0.509267	2.9
PW-019	Fe-lava	23.22	3.92	0.512257	0.000004	0.1679	0.509252	2.6
PW-019*	Fe-lava	14.33	3.95	0.512247	0.000004	0.1669	0.509259	2.7
PW-020	Fe-lava	19.23	5.22	0.512187	0.000005	0.1640	0.509251	2.6
PW-020*	Fe-lava	19.42	5.26	0.512173	0.000004	0.1637	0.509242	2.4
PW-027	tholeiite	9.60	3.01	0.512613	0.000004	0.1894	0.509224	2.0
PW-029	tholeiite	8.35	2.64	0.512642	0.000004	0.1911	0.509221	2.0
PW-032	tholeiite	8.66	2.73	0.512640	0.000005	0.1900	0.509229	2.1
PW-033	peridotite	13.21	2.97	0.511685	0.000005	0.1359	0.509251	2.6
PW-033*	peridotite	20.99	5.13	0.511900	0.000004	0.1478	0.509255	2.6
PW-038	green cpx	9.50	2.75	0.512249	0.000004	0.1698	0.509209	1.7
PW-039	dunite	4.89	1.20	0.511930	0.000004	0.1483	0.509275	3.0
PW-039*	dunite	5.25	1.24	0.511847	0.000005	0.1431	0.509285	3.2
PW-043	dunite	8.87	1.96	0.511645	0.000004	0.1336	0.509255	2.6
PW-049	gabbro	59.97	11.41	0.511306	0.000004	0.1150	0.509248	2.5
PW-055	black cpx	14.92	4.13	0.512226	0.000004	0.1675	0.509227	2.1
PW-055*	black cpx	15.16	4.06	0.512178	0.000005	0.1617	0.509284	3.2
PW-058	black cpx	28.32	5.43	0.511934	0.000004	0.1505	0.509241	2.3
PW-060	gabbro	37.63	7.80	0.511491	0.000004	0.1253	0.509247	2.5

Table 6.1: Sm and Nd isotopic data for the PPH samples. Initial $^{143}Nd/^{144}Nd$ and εNd_i were calculated using an age of 2681 Ma, $^{147}Sm/^{144}Nd$ error is 0.5% of their measured value. Sample numbers denoted with * are duplicate analyses

When all the samples (tholeiites, intrusive rocks and Fe-rich lavas) are plotted together, a Sm-Nd isochron age of 2681±51 Ma is yielded, with an mean square weighted deviation (MSWD) of

6.6 and an initial $^{143}Nd/^{144}Nd$=0.509279±0.000008, corresponding to an εNd_i=2.3±0.2 (Figure 6.10).

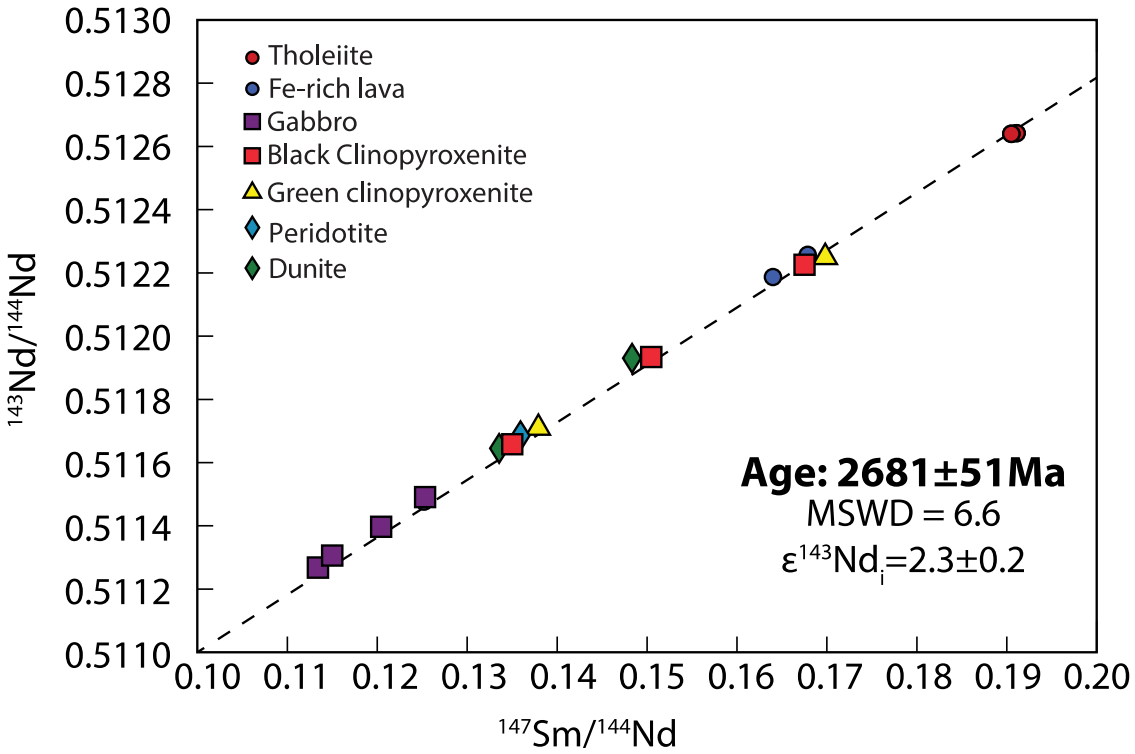

Figure 6.10: ^{147}Sm-^{143}Nd isochron diagram for samples of all lithologies together. Regression (dashed lines) were calculated using ISOPLOT v.4.15 Ludwig (2012),

6.4 ^{142}Nd results

A total of 15 samples were analysed for high precision Nd isotopic compositions in June and November 2018. A total of 2 tholeiites, 2 dunites, 1 peridotite, 1 green clinopyroxenite, 4 black clinopyroxenites, 3 gabbros, and 2 Fe-rich lavas were analysed, the Nd isotopic results for the samples and JNdi-1 standards are in Table 6.2 a-d, Table 6.3, and Figure 6.13. During each session the JNdi-1 standard was analysed multiple times and yielded average $^{142}Nd/^{144}Nd$ of 1.141837±0.000005 (n=4, 2σ) and 1.141837±0.000004 (n=9, 2σ) for the June and November sessions respectively.

June 2018 Analytical Session Standards					Line 1 (144_Ax)					Line 2 (146_Ax)					
Standard: JNdi-1		$^{140}Ce/^{144}Nd$	$^{141}Pr/^{144}Nd$	$^{147}Sm/^{144}Nd$	$^{146}Nd/^{144}Nd$	$^{142}Nd/^{144}Nd$	$^{143}Nd/^{144}Nd$	$^{145}Nd/^{144}Nd$	$^{148}Nd/^{144}Nd$	$^{146}Nd/^{144}Nd$	$^{142}Nd/^{144}Nd$	$^{143}Nd/^{144}Nd$	$^{145}Nd/^{144}Nd$	$^{148}Nd/^{144}Nd$	Dynamic $^{142}Nd/^{144}Nd$
Average ^{142}Nd voltage: 3.4V	Average	-0.000003	0.000049	-0.000001	0.721320	1.141861	0.512107	0.348406	0.241578	0.721304	1.141838	0.512105	0.348403	0.241584	1.141836
	2 Sigma	0.000016	0.000020	0.000010	0.000455	0.000150	0.000058	0.000034	0.000041	0.000457	0.000149	0.000055	0.000034	0.000042	0.000123
	2 SE	0.000000	0.000000	0.000000	0.000011	0.000004	0.000001	0.000001	0.000001	0.000011	0.000004	0.000001	0.000001	0.000001	0.000003

Standard: JNdi-1		$^{140}Ce/^{144}Nd$	$^{141}Pr/^{144}Nd$	$^{147}Sm/^{144}Nd$	$^{146}Nd/^{144}Nd$	$^{142}Nd/^{144}Nd$	$^{143}Nd/^{144}Nd$	$^{145}Nd/^{144}Nd$	$^{148}Nd/^{144}Nd$	$^{146}Nd/^{144}Nd$	$^{142}Nd/^{144}Nd$	$^{143}Nd/^{144}Nd$	$^{145}Nd/^{144}Nd$	$^{148}Nd/^{144}Nd$	Dynamic $^{142}Nd/^{144}Nd$
Average ^{142}Nd voltage: 3.6V	Average	-0.000002	0.000044	-0.000001	0.721571	1.141859	0.512108	0.348406	0.241578	0.721557	1.141840	0.512104	0.348403	0.241583	1.141837
	2 Sigma	0.000020	0.000026	0.000009	0.000893	0.000151	0.000058	0.000033	0.000043	0.000889	0.000163	0.000060	0.000035	0.000043	0.000136
	2 SE	0.000000	0.000001	0.000000	0.000021	0.000004	0.000001	0.000001	0.000001	0.000021	0.000004	0.000001	0.000001	0.000001	0.000003

Standard: JNdi-1		$^{140}Ce/^{144}Nd$	$^{141}Pr/^{144}Nd$	$^{147}Sm/^{144}Nd$	$^{146}Nd/^{144}Nd$	$^{142}Nd/^{144}Nd$	$^{143}Nd/^{144}Nd$	$^{145}Nd/^{144}Nd$	$^{148}Nd/^{144}Nd$	$^{146}Nd/^{144}Nd$	$^{142}Nd/^{144}Nd$	$^{143}Nd/^{144}Nd$	$^{145}Nd/^{144}Nd$	$^{148}Nd/^{144}Nd$	Dynamic $^{142}Nd/^{144}Nd$
Average ^{142}Nd voltage: 3.3V	Average	0.000001	0.000046	-0.000001	0.721792	1.141860	0.512107	0.348406	0.241580	0.721780	1.141842	0.512106	0.348403	0.241583	1.141840
	2 Sigma	0.000016	0.000018	0.000009	0.000609	0.000155	0.000060	0.000036	0.000042	0.000613	0.000151	0.000057	0.000035	0.000042	0.000124
	2 SE	0.000000	0.000001	0.000000	0.000018	0.000005	0.000002	0.000001	0.000001	0.000018	0.000004	0.000002	0.000001	0.000001	0.000004

Standard: JNdi-1		$^{140}Ce/^{144}Nd$	$^{141}Pr/^{144}Nd$	$^{147}Sm/^{144}Nd$	$^{146}Nd/^{144}Nd$	$^{142}Nd/^{144}Nd$	$^{143}Nd/^{144}Nd$	$^{145}Nd/^{144}Nd$	$^{148}Nd/^{144}Nd$	$^{146}Nd/^{144}Nd$	$^{142}Nd/^{144}Nd$	$^{143}Nd/^{144}Nd$	$^{145}Nd/^{144}Nd$	$^{148}Nd/^{144}Nd$	Dynamic $^{142}Nd/^{144}Nd$
Average ^{142}Nd voltage: 3.4V	Average	-0.000004	0.000035	-0.000001	0.722091	1.141857	0.512107	0.348405	0.241578	0.722077	1.141839	0.512105	0.348403	0.241583	1.141835
	2 Sigma	0.000015	0.000024	0.000010	0.001475	0.000150	0.000057	0.000035	0.000041	0.001477	0.000149	0.000057	0.000035	0.000042	0.000122
	2 SE	0.000000	0.000001	0.000000	0.000035	0.000004	0.000001	0.000001	0.000001	0.000035	0.000004	0.000001	0.000001	0.000001	0.000003

Table 6.2a: Nd isotope compositions for the June 2018 analytical session for the terrestrial JNdi-1 standard.

June 2018 Analytical Session Samples					Line 1 (144_Ax)					Line 2 (146_Ax)					
Sample:PW-002		$^{140}Ce/^{144}Nd$	$^{141}Pr/^{144}Nd$	$^{147}Sm/^{144}Nd$	$^{146}Nd/^{144}Nd$	$^{142}Nd/^{144}Nd$	$^{143}Nd/^{144}Nd$	$^{145}Nd/^{144}Nd$	$^{148}Nd/^{144}Nd$	$^{146}Nd/^{144}Nd$	$^{142}Nd/^{144}Nd$	$^{143}Nd/^{144}Nd$	$^{145}Nd/^{144}Nd$	$^{148}Nd/^{144}Nd$	Dynamic $^{142}Nd/^{144}Nd$
Average ^{142}Nd voltage: 3.5V	Average	0.000000	0.596610	-0.000003	0.721233	1.141850	0.511259	0.348405	0.241578	0.721224	1.141840	0.511255	0.348403	0.241583	1.141834
	2 Sigma	0.000013	0.309954	0.000009	0.001418	0.000131	0.000050	0.000029	0.000036	0.001414	0.000138	0.000051	0.000030	0.000037	0.000101
	2 SE	0.000001	0.012664	0.000000	0.000058	0.000005	0.000002	0.000001	0.000001	0.000058	0.000006	0.000002	0.000001	0.000002	0.000004
Sample:PW-014		$^{140}Ce/^{144}Nd$	$^{141}Pr/^{144}Nd$	$^{147}Sm/^{144}Nd$	$^{146}Nd/^{144}Nd$	$^{142}Nd/^{144}Nd$	$^{143}Nd/^{144}Nd$	$^{145}Nd/^{144}Nd$	$^{148}Nd/^{144}Nd$	$^{146}Nd/^{144}Nd$	$^{142}Nd/^{144}Nd$	$^{143}Nd/^{144}Nd$	$^{145}Nd/^{144}Nd$	$^{148}Nd/^{144}Nd$	Dynamic $^{142}Nd/^{144}Nd$
Average ^{142}Nd voltage: 3.3V	Average	0.000005	0.443299	-0.000002	0.721726	1.141854	0.511469	0.348407	0.241577	0.721713	1.141841	0.511463	0.348405	0.241582	1.141834
	2 Sigma	0.000034	0.345058	0.000009	0.001813	0.000143	0.000054	0.000033	0.000040	0.001818	0.000147	0.000055	0.000034	0.000040	0.000119
	2 SE	0.000001	0.009961	0.000000	0.000052	0.000004	0.000002	0.000001	0.000002	0.000052	0.000004	0.000002	0.000001	0.000001	0.000003
Sample:PW-019		$^{140}Ce/^{144}Nd$	$^{141}Pr/^{144}Nd$	$^{147}Sm/^{144}Nd$	$^{146}Nd/^{144}Nd$	$^{142}Nd/^{144}Nd$	$^{143}Nd/^{144}Nd$	$^{145}Nd/^{144}Nd$	$^{148}Nd/^{144}Nd$	$^{146}Nd/^{144}Nd$	$^{142}Nd/^{144}Nd$	$^{143}Nd/^{144}Nd$	$^{145}Nd/^{144}Nd$	$^{148}Nd/^{144}Nd$	Dynamic $^{142}Nd/^{144}Nd$
Average ^{142}Nd voltage: 3.6V	Average	0.000069	0.470502	-0.000004	0.721313	1.141855	0.512250	0.348405	0.241579	0.721299	1.141835	0.512246	0.348404	0.241585	1.141836
	2 Sigma	0.000105	0.231098	0.000009	0.001274	0.000135	0.000049	0.000031	0.000036	0.001269	0.000133	0.000049	0.000032	0.000036	0.000111
	2 SE	0.000004	0.009435	0.000000	0.000052	0.000006	0.000002	0.000001	0.000002	0.000052	0.000006	0.000002	0.000001	0.000002	0.000005
Sample:PW-020		$^{140}Ce/^{144}Nd$	$^{141}Pr/^{144}Nd$	$^{147}Sm/^{144}Nd$	$^{146}Nd/^{144}Nd$	$^{142}Nd/^{144}Nd$	$^{143}Nd/^{144}Nd$	$^{145}Nd/^{144}Nd$	$^{148}Nd/^{144}Nd$	$^{146}Nd/^{144}Nd$	$^{142}Nd/^{144}Nd$	$^{143}Nd/^{144}Nd$	$^{145}Nd/^{144}Nd$	$^{148}Nd/^{144}Nd$	Dynamic $^{142}Nd/^{144}Nd$
Average ^{142}Nd voltage: 3.7V	Average	0.000014	0.387725	-0.000002	0.721627	1.141856	0.512178	0.348405	0.241579	0.721613	1.141842	0.512174	0.348402	0.241585	1.141837
	2 Sigma	0.000032	0.251077	0.000010	0.000669	0.000141	0.000054	0.000032	0.000039	0.000667	0.000136	0.000053	0.000032	0.000040	0.000115
	2 SE	0.000001	0.007248	0.000000	0.000019	0.000004	0.000002	0.000001	0.000002	0.000027	0.000004	0.000002	0.000001	0.000001	0.000003
Sample:PW-029		$^{140}Ce/^{144}Nd$	$^{141}Pr/^{144}Nd$	$^{147}Sm/^{144}Nd$	$^{146}Nd/^{144}Nd$	$^{142}Nd/^{144}Nd$	$^{143}Nd/^{144}Nd$	$^{145}Nd/^{144}Nd$	$^{148}Nd/^{144}Nd$	$^{146}Nd/^{144}Nd$	$^{142}Nd/^{144}Nd$	$^{143}Nd/^{144}Nd$	$^{145}Nd/^{144}Nd$	$^{148}Nd/^{144}Nd$	Dynamic $^{142}Nd/^{144}Nd$
Average ^{142}Nd voltage: 3.7V	Average	0.000006	0.209675	-0.000003	0.720958	1.141858	0.512636	0.348407	0.241576	0.720943	1.141829	0.512629	0.348404	0.241583	1.141833
	2 Sigma	0.000016	0.128621	0.000009	0.001324	0.000127	0.000045	0.000030	0.000036	0.001330	0.000133	0.000049	0.000029	0.000036	0.000110
	2 SE	0.000001	0.005269	0.000000	0.000054	0.000005	0.000002	0.000001	0.000002	0.000054	0.000006	0.000002	0.000001	0.000002	0.000005
Sample:PW-032		$^{140}Ce/^{144}Nd$	$^{141}Pr/^{144}Nd$	$^{147}Sm/^{144}Nd$	$^{146}Nd/^{144}Nd$	$^{142}Nd/^{144}Nd$	$^{143}Nd/^{144}Nd$	$^{145}Nd/^{144}Nd$	$^{148}Nd/^{144}Nd$	$^{146}Nd/^{144}Nd$	$^{142}Nd/^{144}Nd$	$^{143}Nd/^{144}Nd$	$^{145}Nd/^{144}Nd$	$^{148}Nd/^{144}Nd$	Dynamic $^{142}Nd/^{144}Nd$
Average ^{142}Nd voltage: 3.5V	Average	0.000002	0.875331	-0.000003	0.721609	1.141847	0.512625	0.348406	0.241578	0.721600	1.141834	0.512618	0.348404	0.241585	1.141833
	2 Sigma	0.000013	0.558219	0.000008	0.001605	0.000135	0.000053	0.000032	0.000038	0.001599	0.000128	0.000049	0.000031	0.000033	0.000103
	2 SE	0.000001	0.022789	0.000000	0.000066	0.000006	0.000002	0.000001	0.000002	0.000065	0.000005	0.000002	0.000001	0.000001	0.000004
SamplePW-058		$^{140}Ce/^{144}Nd$	$^{141}Pr/^{144}Nd$	$^{147}Sm/^{144}Nd$	$^{146}Nd/^{144}Nd$	$^{142}Nd/^{144}Nd$	$^{143}Nd/^{144}Nd$	$^{145}Nd/^{144}Nd$	$^{148}Nd/^{144}Nd$	$^{146}Nd/^{144}Nd$	$^{142}Nd/^{144}Nd$	$^{143}Nd/^{144}Nd$	$^{145}Nd/^{144}Nd$	$^{148}Nd/^{144}Nd$	Dynamic $^{142}Nd/^{144}Nd$
Average ^{142}Nd voltage: 3.4V	Average	0.000005	0.468198	-0.000004	0.721370	1.141849	0.511934	0.348407	0.241577	0.721358	1.141834	0.511924	0.348405	0.241583	1.141832
	2 Sigma	0.000023	0.357966	0.000009	0.001687	0.000129	0.000047	0.000028	0.000035	0.001686	0.000128	0.000047	0.000029	0.000036	0.000107
	2 SE	0.000001	0.014614	0.000000	0.000069	0.000005	0.000002	0.000001	0.000001	0.000069	0.000005	0.000002	0.000001	0.000001	0.000004

Table 6.2b: Nd isotope compositions for the June 2018 analytical session for the standards analyzed

November 2018 Analytical Session 3 Standards					Line 1 (144_Ax)					Line 2 (146_Ax)					
Standard: JNdi-1		$^{140}Ce/^{144}Nd$	$^{141}Pr/^{144}Nd$	$^{147}Sm/^{144}Nd$	$^{146}Nd/^{144}Nd$	$^{142}Nd/^{144}Nd$	$^{143}Nd/^{144}Nd$	$^{145}Nd/^{144}Nd$	$^{148}Nd/^{144}Nd$	$^{146}Nd/^{144}Nd$	$^{142}Nd/^{144}Nd$	$^{143}Nd/^{144}Nd$	$^{145}Nd/^{144}Nd$	$^{148}Nd/^{144}Nd$	Dynamic $^{142}Nd/^{144}Nd$
Average ^{142}Nd voltage: 2.2V	Average	-0.000007	0.000026	0.000000	0.722582	1.141861	0.512107	0.348407	0.241577	0.722568	1.141843	0.512106	0.348405	0.241581	1.141836
	2 Sigma	0.000016	0.000015	0.000014	0.000769	0.000175	0.000069	0.000036	0.000049	0.000765	0.000168	0.000062	0.000036	0.000046	0.000136
	2 SE	0.000001	0.000001	0.000001	0.000032	0.000007	0.000003	0.000002	0.000002	0.000032	0.000007	0.000003	0.000002	0.000002	0.000006

Standard: JNdi-1		$^{140}Ce/^{144}Nd$	$^{141}Pr/^{144}Nd$	$^{147}Sm/^{144}Nd$	$^{146}Nd/^{144}Nd$	$^{142}Nd/^{144}Nd$	$^{143}Nd/^{144}Nd$	$^{145}Nd/^{144}Nd$	$^{148}Nd/^{144}Nd$	$^{146}Nd/^{144}Nd$	$^{142}Nd/^{144}Nd$	$^{143}Nd/^{144}Nd$	$^{145}Nd/^{144}Nd$	$^{148}Nd/^{144}Nd$	Dynamic $^{142}Nd/^{144}Nd$
Average ^{142}Nd voltage: 3.5V	Average	-0.000003	0.000037	0.000000	0.721773	1.141862	0.512108	0.348406	0.241577	0.721759	1.141841	0.512104	0.348402	0.241584	1.141837
	2 Sigma	0.000015	0.000021	0.000009	0.000920	0.000128	0.000047	0.000029	0.000037	0.000912	0.000127	0.000046	0.000030	0.000036	0.000110
	2 SE	0.000001	0.000001	0.000000	0.000038	0.000005	0.000002	0.000001	0.000002	0.000037	0.000005	0.000002	0.000001	0.000001	0.000005

Standard: JNdi-1		$^{140}Ce/^{144}Nd$	$^{141}Pr/^{144}Nd$	$^{147}Sm/^{144}Nd$	$^{146}Nd/^{144}Nd$	$^{142}Nd/^{144}Nd$	$^{143}Nd/^{144}Nd$	$^{145}Nd/^{144}Nd$	$^{148}Nd/^{144}Nd$	$^{146}Nd/^{144}Nd$	$^{142}Nd/^{144}Nd$	$^{143}Nd/^{144}Nd$	$^{145}Nd/^{144}Nd$	$^{148}Nd/^{144}Nd$	Dynamic $^{142}Nd/^{144}Nd$
Average ^{142}Nd voltage: 3.2V	Average	0.000001	0.000045	0.000001	0.721391	1.141855	0.512108	0.348406	0.241578	0.721380	1.141846	0.512109	0.348404	0.241582	1.141838
	2 Sigma	0.000014	0.000017	0.000012	0.001096	0.000142	0.000052	0.000030	0.000037	0.001093	0.000137	0.000051	0.000030	0.000041	0.000108
	2 SE	0.000001	0.000001	0.000000	0.000045	0.000006	0.000002	0.000001	0.000002	0.000045	0.000006	0.000002	0.000001	0.000002	0.000005

Standard: JNdi-1		$^{140}Ce/^{144}Nd$	$^{141}Pr/^{144}Nd$	$^{147}Sm/^{144}Nd$	$^{146}Nd/^{144}Nd$	$^{142}Nd/^{144}Nd$	$^{143}Nd/^{144}Nd$	$^{145}Nd/^{144}Nd$	$^{148}Nd/^{144}Nd$	$^{146}Nd/^{144}Nd$	$^{142}Nd/^{144}Nd$	$^{143}Nd/^{144}Nd$	$^{145}Nd/^{144}Nd$	$^{148}Nd/^{144}Nd$	Dynamic $^{142}Nd/^{144}Nd$
Average ^{142}Nd voltage: 3.6V	Average	-0.000001	0.000043	-0.000001	0.721517	1.141852	0.512107	0.348405	0.241581	0.721508	1.141845	0.512109	0.348405	0.241582	1.141839
	2 Sigma	0.000016	0.000018	0.000013	0.000764	0.000133	0.000050	0.000028	0.000037	0.000758	0.000127	0.000047	0.000029	0.000038	0.000107
	2 SE	0.000001	0.000001	0.000001	0.000031	0.000006	0.000002	0.000001	0.000002	0.000031	0.000005	0.000002	0.000001	0.000002	0.000004

Standard: JNdi-1		$^{140}Ce/^{144}Nd$	$^{141}Pr/^{144}Nd$	$^{147}Sm/^{144}Nd$	$^{146}Nd/^{144}Nd$	$^{142}Nd/^{144}Nd$	$^{143}Nd/^{144}Nd$	$^{145}Nd/^{144}Nd$	$^{148}Nd/^{144}Nd$	$^{146}Nd/^{144}Nd$	$^{142}Nd/^{144}Nd$	$^{143}Nd/^{144}Nd$	$^{145}Nd/^{144}Nd$	$^{148}Nd/^{144}Nd$	Dynamic $^{142}Nd/^{144}Nd$
Average ^{142}Nd voltage: 3.0V	Average	0.000001	0.000045	-0.000001	0.721343	1.141862	0.512104	0.348406	0.241579	0.721329	1.141844	0.512106	0.348403	0.241586	1.141839
	2 Sigma	0.000029	0.000030	0.000013	0.001019	0.000142	0.000055	0.000031	0.000041	0.001017	0.000137	0.000052	0.000031	0.000041	0.000118
	2 SE	0.000001	0.000001	0.000001	0.000042	0.000006	0.000002	0.000001	0.000002	0.000042	0.000006	0.000002	0.000001	0.000002	0.000005

Standard: JNdi-1		$^{140}Ce/^{144}Nd$	$^{141}Pr/^{144}Nd$	$^{147}Sm/^{144}Nd$	$^{146}Nd/^{144}Nd$	$^{142}Nd/^{144}Nd$	$^{143}Nd/^{144}Nd$	$^{145}Nd/^{144}Nd$	$^{148}Nd/^{144}Nd$	$^{146}Nd/^{144}Nd$	$^{142}Nd/^{144}Nd$	$^{143}Nd/^{144}Nd$	$^{145}Nd/^{144}Nd$	$^{148}Nd/^{144}Nd$	Dynamic $^{142}Nd/^{144}Nd$
Average ^{142}Nd voltage: 3.4V	Average	0.000011	0.000058	-0.000001	0.720953	1.141857	0.512108	0.348407	0.241578	0.720942	1.141839	0.512104	0.348403	0.241582	1.141836
	2 Sigma	0.000031	0.000017	0.000010	0.000292	0.000132	0.000050	0.000029	0.000037	0.000296	0.000130	0.000049	0.000029	0.000039	0.000108
	2 SE	0.000001	0.000001	0.000000	0.000012	0.000006	0.000002	0.000001	0.000002	0.000012	0.000005	0.000002	0.000001	0.000002	0.000005

Standard: JNdi-1		$^{140}Ce/^{144}Nd$	$^{141}Pr/^{144}Nd$	$^{147}Sm/^{144}Nd$	$^{146}Nd/^{144}Nd$	$^{142}Nd/^{144}Nd$	$^{143}Nd/^{144}Nd$	$^{145}Nd/^{144}Nd$	$^{148}Nd/^{144}Nd$	$^{146}Nd/^{144}Nd$	$^{142}Nd/^{144}Nd$	$^{143}Nd/^{144}Nd$	$^{145}Nd/^{144}Nd$	$^{148}Nd/^{144}Nd$	Dynamic $^{142}Nd/^{144}Nd$
Average ^{142}Nd voltage: 3.3V	Average	-0.000004	0.000036	0.000000	0.721829	1.141849	0.512107	0.348407	0.241578	0.721819	1.141845	0.512107	0.348405	0.241583	1.141836
	2 Sigma	0.000013	0.000021	0.000010	0.001451	0.000138	0.000053	0.000032	0.000038	0.001452	0.000135	0.000054	0.000031	0.000039	0.000113
	2 SE	0.000001	0.000001	0.000000	0.000059	0.000006	0.000002	0.000001	0.000002	0.000059	0.000006	0.000002	0.000001	0.000002	0.000005

Standard: JNdi-1		$^{140}Ce/^{144}Nd$	$^{141}Pr/^{144}Nd$	$^{147}Sm/^{144}Nd$	$^{146}Nd/^{144}Nd$	$^{142}Nd/^{144}Nd$	$^{143}Nd/^{144}Nd$	$^{145}Nd/^{144}Nd$	$^{148}Nd/^{144}Nd$	$^{146}Nd/^{144}Nd$	$^{142}Nd/^{144}Nd$	$^{143}Nd/^{144}Nd$	$^{145}Nd/^{144}Nd$	$^{148}Nd/^{144}Nd$	Dynamic $^{142}Nd/^{144}Nd$
Average ^{142}Nd voltage: 3.8V	Average	0.000002	0.000049	0.000000	0.721109	1.141853	0.512108	0.348407	0.241579	0.721098	1.141846	0.512108	0.348405	0.241583	1.141835
	2 Sigma	0.000015	0.000012	0.000012	0.000865	0.000131	0.000049	0.000027	0.000034	0.000867	0.000124	0.000046	0.000029	0.000035	0.000102
	2 SE	0.000001	0.000000	0.000000	0.000035	0.000005	0.000002	0.000001	0.000001	0.000036	0.000005	0.000002	0.000001	0.000001	0.000004

Standard: JNdi-1		$^{140}Ce/^{144}Nd$	$^{141}Pr/^{144}Nd$	$^{147}Sm/^{144}Nd$	$^{146}Nd/^{144}Nd$	$^{142}Nd/^{144}Nd$	$^{143}Nd/^{144}Nd$	$^{145}Nd/^{144}Nd$	$^{148}Nd/^{144}Nd$	$^{146}Nd/^{144}Nd$	$^{142}Nd/^{144}Nd$	$^{143}Nd/^{144}Nd$	$^{145}Nd/^{144}Nd$	$^{148}Nd/^{144}Nd$	Dynamic $^{142}Nd/^{144}Nd$
Average ^{142}Nd voltage: 3.4V	Average	0.000000	0.000043	-0.000001	0.721402	1.141849	0.512109	0.348406	0.241579	0.721393	1.141860	0.512111	0.348406	0.241583	1.141833
	2 Sigma	0.000015	0.000020	0.000011	0.000998	0.000134	0.000050	0.000031	0.000036	0.000998	0.000136	0.000051	0.000030	0.000036	0.000109
	2 SE	0.000001	0.000001	0.000000	0.000041	0.000006	0.000002	0.000001	0.000002	0.000041	0.000006	0.000002	0.000001	0.000002	0.000005

Table 6.2c: Nd isotope compositions for the November 2018 analytical session for the samples JNdi-1 standard.

November 2018 Analytical Session Samples					Line 1 (144_Ax)					Line 2 (146_Ax)					
Sample:PW-012		$^{140}Ce/^{144}Nd$	$^{141}Pr/^{144}Nd$	$^{147}Sm/^{144}Nd$	$^{146}Nd/^{144}Nd$	$^{142}Nd/^{144}Nd$	$^{143}Nd/^{144}Nd$	$^{145}Nd/^{144}Nd$	$^{148}Nd/^{144}Nd$	$^{146}Nd/^{144}Nd$	$^{142}Nd/^{144}Nd$	$^{143}Nd/^{144}Nd$	$^{145}Nd/^{144}Nd$	$^{148}Nd/^{144}Nd$	Dynamic $^{142}Nd/^{144}Nd$
Average ^{142}Nd voltage: 3.6V	Average	0.000001	1.433960	-0.000001	0.721116	1.141857	0.511392	0.348404	0.241577	0.721101	1.141839	0.511380	0.348403	0.241583	1.141835
	2 Sigma	0.000017	0.301711	0.000010	0.000421	0.000132	0.000053	0.000029	0.000037	0.000415	0.000120	0.000048	0.000028	0.000035	0.000099
	2 SE	0.000001	0.012317	0.000000	0.000017	0.000006	0.000002	0.000001	0.000002	0.000017	0.000005	0.000002	0.000001	0.000001	0.000004

Sample:PW-015		$^{140}Ce/^{144}Nd$	$^{141}Pr/^{144}Nd$	$^{147}Sm/^{144}Nd$	$^{146}Nd/^{144}Nd$	$^{142}Nd/^{144}Nd$	$^{143}Nd/^{144}Nd$	$^{145}Nd/^{144}Nd$	$^{148}Nd/^{144}Nd$	$^{146}Nd/^{144}Nd$	$^{142}Nd/^{144}Nd$	$^{143}Nd/^{144}Nd$	$^{145}Nd/^{144}Nd$	$^{148}Nd/^{144}Nd$	Dynamic $^{142}Nd/^{144}Nd$
Average ^{142}Nd voltage: 3.5V	Average	-0.000005	0.267953	-0.000003	0.721334	1.141853	0.511705	0.348406	0.241578	0.721325	1.141847	0.511707	0.348405	0.241582	1.141836
	2 Sigma	0.000012	0.090836	0.000009	0.000785	0.000123	0.000048	0.000030	0.000037	0.000783	0.000138	0.000050	0.000029	0.000036	0.000107
	2 SE	0.000000	0.003708	0.000000	0.000032	0.000005	0.000002	0.000001	0.000002	0.000032	0.000006	0.000002	0.000001	0.000002	0.000004

Sample:PW-033		$^{140}Ce/^{144}Nd$	$^{141}Pr/^{144}Nd$	$^{147}Sm/^{144}Nd$	$^{146}Nd/^{144}Nd$	$^{142}Nd/^{144}Nd$	$^{143}Nd/^{144}Nd$	$^{145}Nd/^{144}Nd$	$^{148}Nd/^{144}Nd$	$^{146}Nd/^{144}Nd$	$^{142}Nd/^{144}Nd$	$^{143}Nd/^{144}Nd$	$^{145}Nd/^{144}Nd$	$^{148}Nd/^{144}Nd$	Dynamic $^{142}Nd/^{144}Nd$
Average ^{142}Nd voltage: 3.4V	Average	-0.000006	1.090032	-0.000003	0.721345	1.141852	0.511678	0.348406	0.241579	0.721336	1.141851	0.511673	0.348405	0.241582	1.141837
	2 Sigma	0.000014	0.293182	0.000009	0.000823	0.000127	0.000051	0.000030	0.000037	0.000824	0.000130	0.000048	0.000029	0.000035	0.000101
	2 SE	0.000001	0.012029	0.000000	0.000034	0.000005	0.000002	0.000001	0.000002	0.000034	0.000005	0.000002	0.000001	0.000001	0.000004

Sample:PW-038		$^{140}Ce/^{144}Nd$	$^{141}Pr/^{144}Nd$	$^{147}Sm/^{144}Nd$	$^{146}Nd/^{144}Nd$	$^{142}Nd/^{144}Nd$	$^{143}Nd/^{144}Nd$	$^{145}Nd/^{144}Nd$	$^{148}Nd/^{144}Nd$	$^{146}Nd/^{144}Nd$	$^{142}Nd/^{144}Nd$	$^{143}Nd/^{144}Nd$	$^{145}Nd/^{144}Nd$	$^{148}Nd/^{144}Nd$	Dynamic $^{142}Nd/^{144}Nd$
Average ^{142}Nd voltage: 3.5V	Average	-0.000004	0.812951	0.000001	0.721501	1.141848	0.512246	0.348407	0.241577	0.721492	1.141847	0.512239	0.348402	0.241580	1.141833
	2 Sigma	0.000012	0.260824	0.000009	0.001189	0.000132	0.000050	0.000030	0.000036	0.001189	0.000135	0.000051	0.000031	0.000037	0.000110
	2 SE	0.000001	0.010648	0.000000	0.000049	0.000006	0.000002	0.000001	0.000002	0.000049	0.000006	0.000002	0.000001	0.000002	0.000005

Sample:PW-039		$^{140}Ce/^{144}Nd$	$^{141}Pr/^{144}Nd$	$^{147}Sm/^{144}Nd$	$^{146}Nd/^{144}Nd$	$^{142}Nd/^{144}Nd$	$^{143}Nd/^{144}Nd$	$^{145}Nd/^{144}Nd$	$^{148}Nd/^{144}Nd$	$^{146}Nd/^{144}Nd$	$^{142}Nd/^{144}Nd$	$^{143}Nd/^{144}Nd$	$^{145}Nd/^{144}Nd$	$^{148}Nd/^{144}Nd$	Dynamic $^{142}Nd/^{144}Nd$
Average ^{142}Nd voltage: 3.7V	Average	-0.000005	0.616400	-0.000003	0.721309	1.141848	0.511926	0.348406	0.241579	0.721302	1.141855	0.511924	0.348405	0.241581	1.141836
	2 Sigma	0.000013	0.167435	0.000008	0.000806	0.000123	0.000048	0.000029	0.000036	0.000804	0.000131	0.000048	0.000027	0.000036	0.000100
	2 SE	0.000000	0.006301	0.000000	0.000030	0.000005	0.000002	0.000001	0.000001	0.000030	0.000005	0.000002	0.000001	0.000001	0.000004

Sample:PW-043		$^{140}Ce/^{144}Nd$	$^{141}Pr/^{144}Nd$	$^{147}Sm/^{144}Nd$	$^{146}Nd/^{144}Nd$	$^{142}Nd/^{144}Nd$	$^{143}Nd/^{144}Nd$	$^{145}Nd/^{144}Nd$	$^{148}Nd/^{144}Nd$	$^{146}Nd/^{144}Nd$	$^{142}Nd/^{144}Nd$	$^{143}Nd/^{144}Nd$	$^{145}Nd/^{144}Nd$	$^{148}Nd/^{144}Nd$	Dynamic $^{142}Nd/^{144}Nd$
Average ^{142}Nd voltage: 3.5V	Average	-0.000006	1.219837	-0.000003	0.721169	1.141840	0.511635	0.348407	0.241577	0.721165	1.141860	0.511633	0.348404	0.241579	1.141835
	2 Sigma	0.000013	0.458119	0.000009	0.001227	0.000135	0.000050	0.000030	0.000037	0.001222	0.000120	0.000047	0.000029	0.000035	0.000104
	2 SE	0.000001	0.018750	0.000000	0.000050	0.000006	0.000002	0.000001	0.000002	0.000050	0.000005	0.000002	0.000001	0.000001	0.000004

Sample:PW-055		$^{140}Ce/^{144}Nd$	$^{141}Pr/^{144}Nd$	$^{147}Sm/^{144}Nd$	$^{146}Nd/^{144}Nd$	$^{142}Nd/^{144}Nd$	$^{143}Nd/^{144}Nd$	$^{145}Nd/^{144}Nd$	$^{148}Nd/^{144}Nd$	$^{146}Nd/^{144}Nd$	$^{142}Nd/^{144}Nd$	$^{143}Nd/^{144}Nd$	$^{145}Nd/^{144}Nd$	$^{148}Nd/^{144}Nd$	Dynamic $^{142}Nd/^{144}Nd$
Average ^{142}Nd voltage: 3.9V	Average	-0.000004	1.056629	-0.000003	0.721242	1.141846	0.512219	0.348406	0.241574	0.721233	1.141854	0.512214	0.348405	0.241582	1.141830
	2 Sigma	0.000012	0.330147	0.000008	0.000835	0.000119	0.000045	0.000027	0.000035	0.000828	0.000122	0.000047	0.000030	0.000035	0.000100
	2 SE	0.000000	0.013478	0.000000	0.000034	0.000005	0.000002	0.000001	0.000001	0.000034	0.000005	0.000002	0.000001	0.000001	0.000004

Sample:PW-060		$^{140}Ce/^{144}Nd$	$^{141}Pr/^{144}Nd$	$^{147}Sm/^{144}Nd$	$^{146}Nd/^{144}Nd$	$^{142}Nd/^{144}Nd$	$^{143}Nd/^{144}Nd$	$^{145}Nd/^{144}Nd$	$^{148}Nd/^{144}Nd$	$^{146}Nd/^{144}Nd$	$^{142}Nd/^{144}Nd$	$^{143}Nd/^{144}Nd$	$^{145}Nd/^{144}Nd$	$^{148}Nd/^{144}Nd$	Dynamic $^{142}Nd/^{144}Nd$
Average ^{142}Nd voltage: 3.7V	Average	0.000006	1.397280	-0.000003	0.721198	1.141843	0.511480	0.348407	0.241580	0.721193	1.141855	0.511472	0.348404	0.241579	1.141837
	2 Sigma	0.000019	0.386116	0.000008	0.000662	0.000123	0.000048	0.000030	0.000038	0.000657	0.000129	0.000048	0.000029	0.000036	0.000103
	2 SE	0.000001	0.015763	0.000000	0.000027	0.000005	0.000002	0.000001	0.000002	0.000027	0.000005	0.000002	0.000001	0.000002	0.000004

Table 6.2d: Nd isotope compositions for the November 2018 analytical session for the standards analyzed

The quality of the results can be evaluated by comparing $^{142}Nd/^{144}Nd$ ratios to other stable isotope ratios measured. The absence of correlation between $\mu^{142}Nd$ and $\mu^{145, 148, 150}Nd$, indicates that mass dependent fractionation is adequately corrected (Figure 6.11).

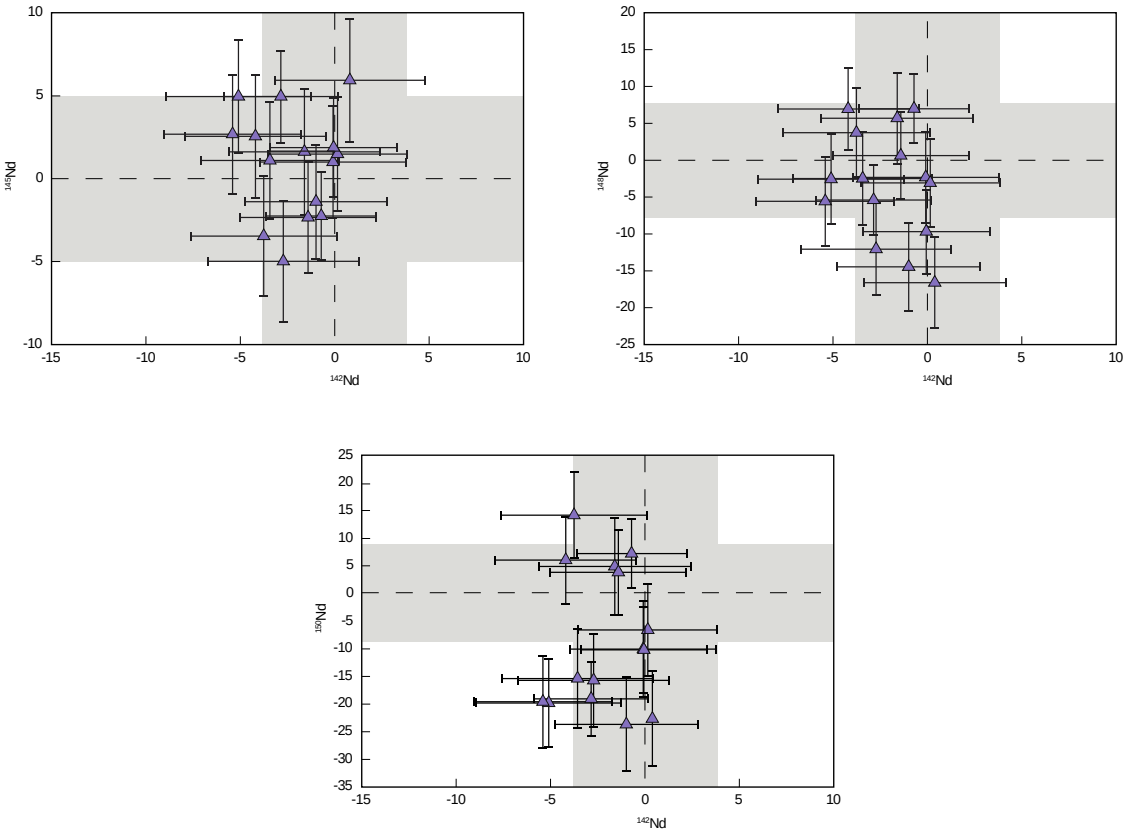

Figure 6.11 $\mu^{142}Nd$ vs. $\mu^{145, 148, 150}Nd$ for the 15 samples. The values are expressed in μ notation, as ppm derivation from the JNdi-1 standard that was analyzed during the same analytical sessions. The grey bands are the errors on the average $\mu^{142, 145, 148, 150}Nd$ values for both analytical sessions. The error bars on the sample data points are 2σ.

The samples show no resolvable ^{142}Nd anomalies, with $\mu^{142}Nd$ values ranging from -5.4 to +0.4 compared to the JNdi-1 terrestrial standard, yielding an overall average -2.0±3.9 (n=15, 2SD) (Figure 6.12, Table 6.3). The Fe-rich lavas yielded an average of -1.7±2.1, the intrusive rocks an average of -1.6±5.4 with samples ranging from -5.4±3.7 to 0.4±3.8. The two tholeiite samples yielded $\mu^{142}Nd$ values of -4.0±3.8 and -3.5±4.1. Two samples, PW-014 and PW-020, in the June

2018 session were run twice on the same filament, and the samples runs were combined to calculate their $\mu^{142}Nd$ values.

June 2018 Analytical Session				
Sample	**$^{142}Nd/^{144}Nd$**	**2SE**	**$\mu^{142}Nd$**	**2SE (ppm)**
PW-002 (black clinopyroxenite)	1.141834	0.000004	-3.2	3.7
PW-014 (gabbro)	1.141834	0.000003	-2.6	3.1
PW-019 (Fe-rich lava)	1.141836	0.000005	-1.4	4.1
PW-020 (Fe-rich lava)	1.141837	0.000003	-0.5	3.0
PW-029 (tholeiite)	1.141833	0.000005	-3.5	4.1
PW-032 (tholeiite)	1.141833	0.000004	-4.0	3.8
PW-058 (gabbro)	1.141832	0.000004	-4.9	3.9
JNdi-1 avg (n=4)	1.141837	0.000005		4.0 (2σ)
November 2018 Analytical Session				
Sample	**$^{142}Nd/^{144}Nd$**	**2SE**	**$\mu^{142}Nd$**	**2SE (ppm)**
PW-012 (black clinopyroxenite)	1.141835	0.000004	-1.4	3.6
PW-015 (gabbro)	1.141836	0.000004	-0.1	3.9
PW-033 (peridotite)	1.141837	0.000004	0.1	3.7
PW-038 (green clinopyroxenite)	1.141833	0.000005	-2.7	4.0
PW-039 (dunite)	1.141836	0.000004	-0.1	3.4
PW-043 (dunite)	1.141835	0.000004	-1.0	3.8
PW-055 (black clinopyroxenite)	1.141830	0.000004	-5.4	3.7
PW-060 (black clinopyroxenite)	1.141837	0.000004	0.4	3.8
JNdi-1 avg (n=9)	1.141837	0.000004		3.7 (2σ)

Table 6.3: Calculated $\mu^{142}Nd$ values for the 15 samples analysed for each analytical session, with 2 standard error (ppm). Reported JNdi-1 values are the average of the standards analysed during each analytical session

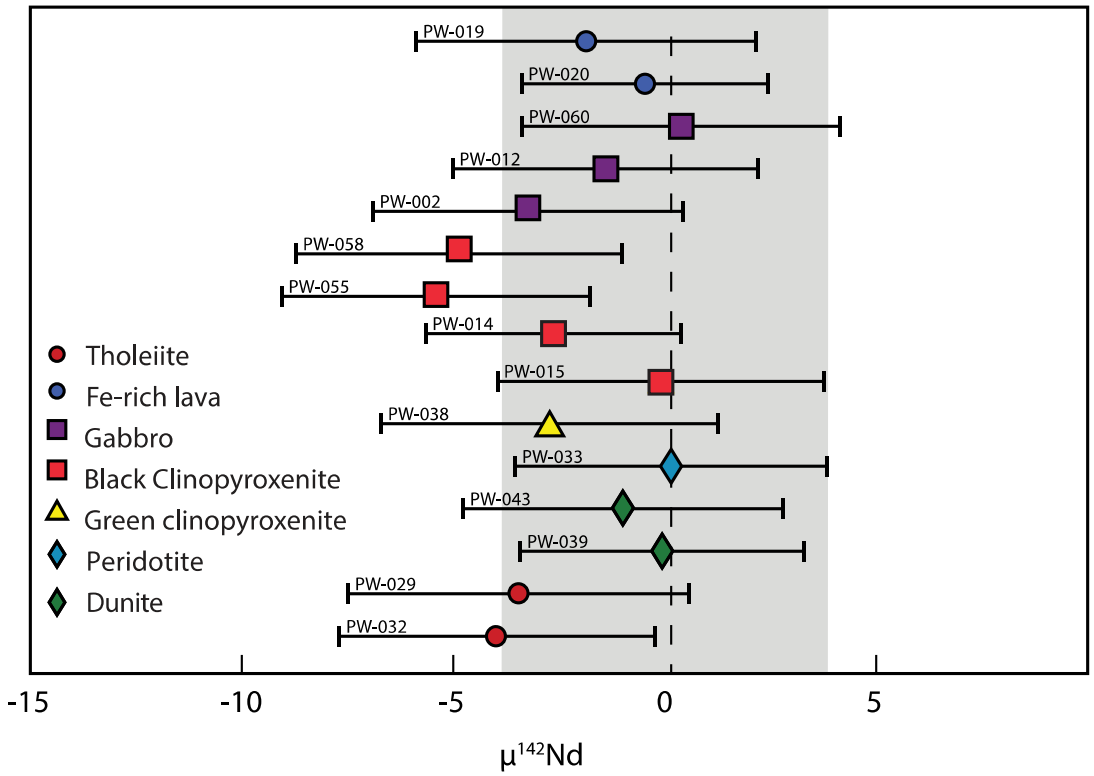

Figure 6.12: $\mu^{142}Nd$ values for the 15 samples from the Pulpwood-Playter Harbour sequence. Values are expressed in ppm deviations from the measured JNdi-1 Nd terrestrial standard, each sample was analysed once, with the exception of PW-014 and PW-020 that was run twice and the runs are combined. The symbols represent the calculated $\mu^{142}Nd$ values with 2SE bars. The grey zone is the 2SD error (reproducibility) on the average JNdi-1 standard.

6.5 ^{182}W results

Five samples were analysed for high precision W isotopic compositions in September 2018; 1 dunite, 1 green clinopyroxenite and 3 black clinopyroxenites. The W isotopic results for the samples and standards are in Table 6.4, Table 6.5 and Figure 6.14. During the analytical session a W-standard was analysed numerous times, yielding an average of 0.864892±0.000004 (n=7, 2σ).

	Line 1						Line 2						
B20180923-StdW	180W/184W	181W/184W	182W/184W	183W/184W	185W/184W	186W/184W	182W/184W	183W/184W	185W/184W	186W/184W	187W/184W	Mean 182W/184W	Mean 183W/184W
Average	0.003866	0.000002	0.864888	0.467111	0.010085	0.927670	0.864893	0.467118	0.010085	0.927670	0.016768	0.864890	0.467115
2*SE	0.000002	0.000001	0.000004	0.000002	0.000048	0.000000	0.000009	0.000004	0.000048	0.000000	0.000080	0.000005	0.000002

B20180923-StdW	180W/184W	181W/184W	182W/184W	183W/184W	185W/184W	186W/184W	182W/184W	183W/184W	185W/184W	186W/184W	187W/184W	Mean 182W/184W	Mean 183W/184W
Average	0.003877	0.000001	0.864884	0.467111	0.006846	0.927670	0.864901	0.467116	0.006844	0.927670	0.011402	0.864893	0.467113
2*SE	0.000001	0.000001	0.000004	0.000002	0.000086	0.000000	0.000007	0.000004	0.000084	0.000000	0.000140	0.000004	0.000002

B20180923-StdW	180W/184W	181W/184W	182W/184W	183W/184W	185W/184W	186W/184W	182W/184W	183W/184W	185W/184W	186W/184W	187W/184W	Mean 182W/184W	Mean 183W/184W
Average	0.003873	0.000001	0.864877	0.467108	0.006273	0.927670	0.864901	0.467120	0.006275	0.927670	0.010422	0.864890	0.467114
2*SE	0.000002	0.000000	0.000004	0.000002	0.000104	0.000000	0.000008	0.000004	0.000104	0.000000	0.000172	0.000005	0.000002

B20180923-StdW	180W/184W	181W/184W	182W/184W	183W/184W	185W/184W	186W/184W	182W/184W	183W/184W	185W/184W	186W/184W	187W/184W	Mean 182W/184W	Mean 183W/184W
Average	0.003878	0.000001	0.864879	0.467107	0.008149	0.927670	0.864904	0.467118	0.008143	0.927670	0.013564	0.864890	0.467113
2*SE	0.000001	0.000001	0.000005	0.000002	0.000213	0.000000	0.000009	0.000004	0.000211	0.000000	0.000352	0.000005	0.000003

B20180923-StdW	180W/184W	181W/184W	182W/184W	183W/184W	185W/184W	186W/184W	182W/184W	183W/184W	185W/184W	186W/184W	187W/184W	Mean 182W/184W	Mean 183W/184W
Average	0.003866	0.000001	0.864891	0.467113	0.009699	0.927670	0.864892	0.467119	0.009684	0.927670	0.016070	0.864894	0.467117
2*SE	0.000004	0.000001	0.000007	0.000003	0.000225	0.000000	0.000013	0.000006	0.000225	0.000000	0.000370	0.000007	0.000003

B20181002-StdW	180W/184W	181W/184W	182W/184W	183W/184W	185W/184W	186W/184W	182W/184W	183W/184W	185W/184W	186W/184W	187W/184W	Mean 182W/184W	Mean 183W/184W
Average	0.003874687	1.46345E-06	0.864883502	0.467113224	0.02300005	0.92767	0.864904329	0.467121169	0.023002931	0.92767	0.03830606	0.864895	0.467115758
2*SE	1.34258E-06	6.33444E-07	5.18257E-06	2.74083E-06	0.000730988	4.8203E-16	1.16985E-05	5.38093E-06	0.000733565	4.82934E-16	0.001219489	5.78751E-06	2.95222E-06

B20181002-StdW	180W/184W	181W/184W	182W/184W	183W/184W	185W/184W	186W/184W	182W/184W	183W/184W	185W/184W	186W/184W	187W/184W	Mean 182W/184W	Mean 183W/184W
Average	0.003876571	1.61591E-06	0.864881861	0.467110655	0.01165223	0.92767	0.864906162	0.46712063	0.01165341	0.92767	0.019450549	0.864894	0.467115168
2*SE	1.41705E-06	4.88024E-07	4.31888E-06	2.04427E-06	0.000268401	2.42435E-16	7.91989E-06	3.4036E-06	0.000268457	2.42611E-16	0.000447024	4.51898E-06	1.99469E-06

	Line 1						Line 2						
B20180923-PW-039	180W/184W	181W/184W	182W/184W	183W/184W	185W/184W	186W/184W	182W/184W	183W/184W	185W/184W	186W/184W	187W/184W	Mean 182W/184W	Mean 183W/184W
Average	0.003873	0.000000	0.864881	0.467109	0.240378	0.927670	0.864898	0.467117	0.227813	0.927670	0.380431	0.864889	0.467114
2*SE	0.000002	0.000001	0.000004	0.000002	0.015692	0.000000	0.000008	0.000004	0.014688	0.000000	0.024531	0.000005	0.000002

B20180923-PW-038	180W/184W	181W/184W	182W/184W	183W/184W	185W/184W	186W/184W	182W/184W	183W/184W	185W/184W	186W/184W	187W/184W	Mean 182W/184W	Mean 183W/184W
Average	0.003876	0.000000	0.864883	0.467110	0.120145	0.927670	0.864901	0.467120	0.119467	0.927670	0.199618	0.864890	0.467115
2*SE	0.000001	0.000000	0.000004	0.000002	0.012299	0.000000	0.000007	0.000004	0.012092	0.000000	0.020264	0.000004	0.000002

B20180923-PW-015	180W/184W	181W/184W	182W/184W	183W/184W	185W/184W	186W/184W	182W/184W	183W/184W	185W/184W	186W/184W	187W/184W	Mean 182W/184W	Mean 183W/184W
Average	0.003873	-0.000001	0.864883	0.467110	0.091501	0.927670	0.864903	0.467119	0.091412	0.927670	0.152545	0.864892	0.467114
2*SE	0.000002	0.000001	0.000004	0.000002	0.001422	0.000000	0.000009	0.000004	0.001431	0.000000	0.002392	0.000005	0.000002

B20181002-PW-055_b	180W/184W	181W/184W	182W/184W	183W/184W	185W/184W	186W/184W	182W/184W	183W/184W	185W/184W	186W/184W	187W/184W	Mean 182W/184W	Mean 183W/184W
Average	0.003875022	-2.76092E-07	0.864895321	0.46711233	0.027976355	0.92767	0.86491369	0.46711748	0.027973378	0.92767	0.046583404	0.864904506	0.467114905
2*SE	7.62071E-07	4.22034E-07	3.54391E-06	1.6883E-06	0.000368208	7.46902E-16	6.91993E-06	3.38339E-06	0.000368622	7.4699E-16	0.000612906	3.83413E-06	1.81301E-06

B20181002-PW-009	180W/184W	181W/184W	182W/184W	183W/184W	185W/184W	186W/184W	182W/184W	183W/184W	185W/184W	186W/184W	187W/184W	Mean 182W/184W	Mean 183W/184W
Average	0.003874	0.000001	0.864888	0.467111	0.041339	0.927670	0.864901	0.467118	0.041318	0.927670	0.068820	0.864894	0.467115
2*SE	0.000002	0.000001	0.000005	0.000002	0.002695	0.000000	0.000008	0.000004	0.002689	0.000000	0.004479	0.000005	0.000002

Table 6.4: W isotopic data for the standards and 5 samples that were analysed in September 2018.

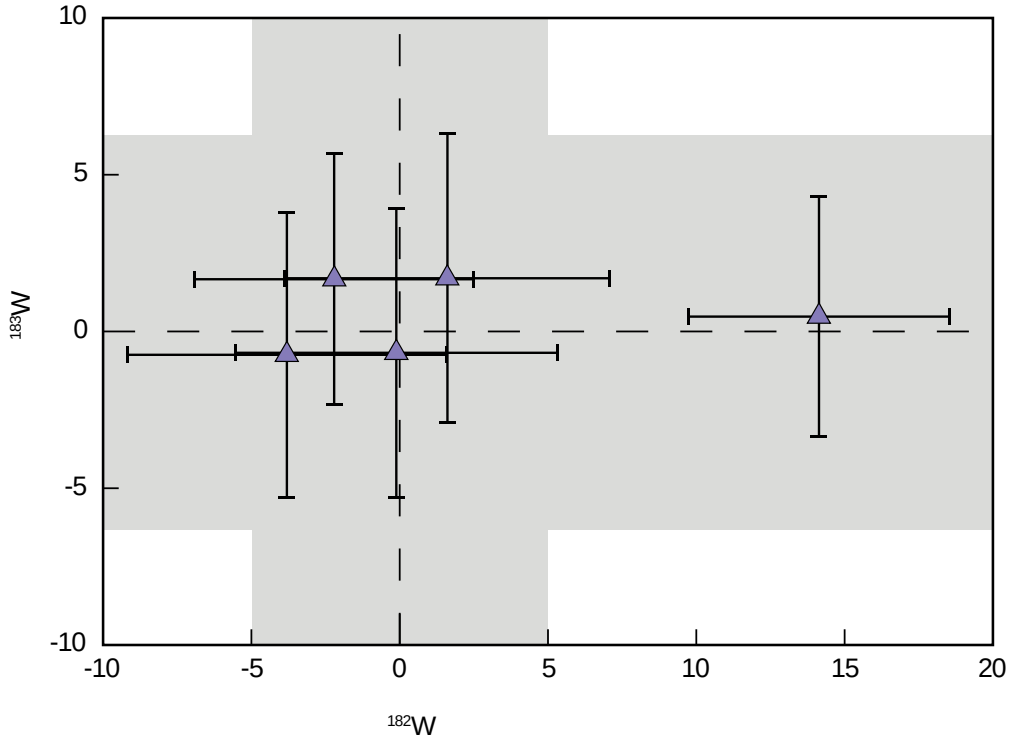

Figure 6.13: $\mu^{182}W$ vs. $\mu^{183}W$ values for the 5 samples and the standard. The values are expressed in μ notation, as ppm derivation from the Alfa Aesar standard that was analyzed during the analytical sessions. The grey error bars are the 2σ of the individual standards calculated $\mu^{182, 183}W$ during analytical session.

During the treatment of data, in addition to $\mu^{182}W$ being calculated from the resulting $^{182}W/^{184}W$ of the sample, ratios of $^{183}W/^{184}W$ were also treated and can be used to calculate $\mu^{183}W$ in the same manner. This value can then be used to establish if any correlation between $\mu^{182}W$ and $\mu^{183}W$ exists (Figure 6.13). No such correlation exists here, indicating that mass dependent fractionation has not played an effect on the $\mu^{182}W$ values measured (Table 6.5).

Sample	$^{182}W/^{184}W$	2SE	$\mu^{182}W$	2SE
StdW	0.864890	0.000005	-3.0	5.6
StdW	0.864893	0.000004	1.0	4.8
StdW	0.864890	0.000005	-2.4	5.3
StdW	0.864890	0.000005	-2.4	6.2
StdW	0.864894	0.000007	2.1	8.3
StdW	0.864895	0.000006	3.0	6.7
StdW	0.864894	0.000005	1.5	5.2
StdW Avg	0.864892	0.000004	0.0	5.0 (2σ)
PW-039 (dunite)	0.864889	0.000005	-3.8	5.4
PW-038 (green clinopyroxenite)	0.864890	0.000004	-2.2	6.2
PW-015 (black clinopyroxenite)	0.864892	0.000005	-0.1	8.3
PW-055 (black clinopyroxenite)	0.864905	0.000004	14.1	6.7
PW-009 (black clinopyroxenite)	0.864894	0.000005	1.6	5.2

Table 6.5: Calculated $\mu^{182}W$ values for the 5 samples analysed for each analytical session, with 2SE (ppm). Reported Alfa Aesar values are the average of the standards analysed during each analytical session

Of the 5 samples analysed for their $\mu^{182}W$ isotopic composition, 4 showed no resolvable anomalies compared to the standard, with values ranging between -3.8 and +1.6 and one sample (PW-055) showed a resolvable $\mu^{182}W$ value of +14.1±6.7 (Figure 6.14). During sample preparation there is nothing to indicate that this sample was contaminated, nor did the yields of the sample suggest fractionation during column separation. Furthermore, during analysis for W isotopic composition, various other isotopes were monitored in order to evaluate if the samples had fractionated differently to what is expected. As indicated in Fig. 6.14, PW-055 does not plot differently to the other samples analyzed during the session for their $\mu^{183}W$ composition.

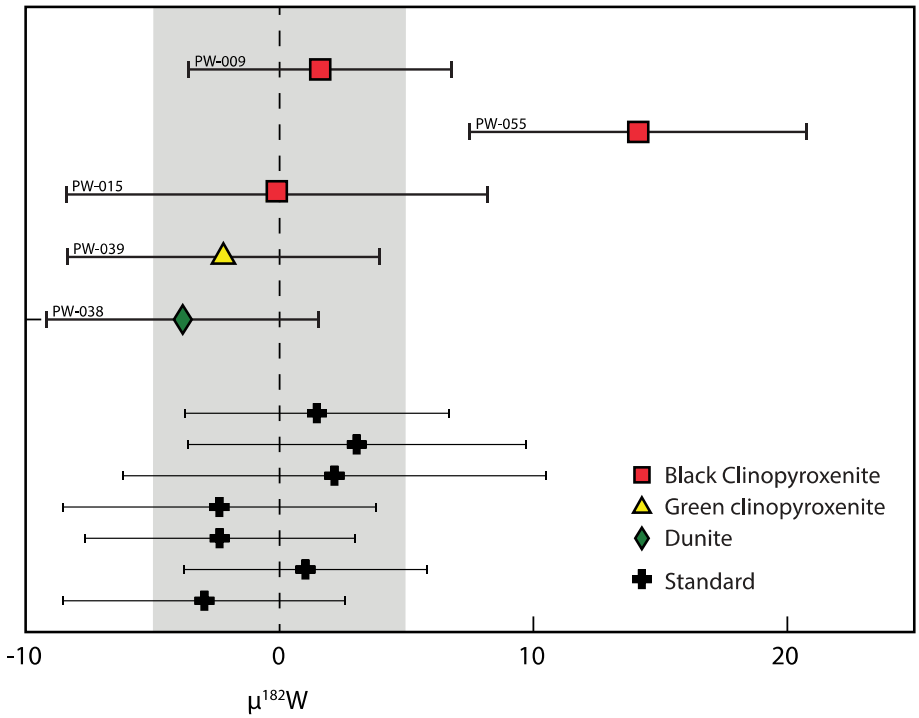

Figure 6.14: $\mu^{182}W$ values for the 5 samples from the Pulpwood-Playter Harbour sequence. Values are expressed in ppm deviations from the measured Alfa Aesar W terrestrial standard, each sample was analysed once. The symbols represent the calculated $\mu^{182}W$ values, and the black lines are 2SE on individual samples. The grey bar represents the 5 ppm 2σ error on the standard.

7.0 Discussion

7.1 Age of the Pulpwood-Playter Harbour sequence

This study aims to characterize the isotopic composition of the mantle source of ferropicrites, in order to constrain the geochemical characteristics of the Neoarchean mantle and perhaps allow for further constraints on ferropicrite petrogenesis. In order to characterize the isotopic composition of mantle-derived rocks, their age of crystallization must first be constrained in order to understand when they have derived from the mantle. Prior to this study, the age of the PPH had not been directly constrained, only inferred from U-Pb zircon analyses from surrounding plutons, suggesting a minimum age of ~2.72 Ga (Corfu and Muir, 1989).

Since the PPH rocks are ultramafic to mafic in composition and do not contain zircons, U-Pb dating cannot be applied to constrain their age. The intrusive rocks transition from ultramafic dunites and peridotites to mafic clinopyroxenites and more evolved gabbros. This cogenetic relationship between rocks of different compositions allows for the applications of isochron age-dating methods to be an ideal tool to constrain their age. Of the various geochronological dating methods, the ^{147}Sm-^{143}Nd system was chosen for several reasons. The Rb-Sr system was not utilized, however, they are much more mobile elements compared to Sm and Nd, and have a lower closure temperature, 450-500 °C, compared to 600-650 °C for the Sm-Nd system. The lower closure temperature makes the Rb-Sr system more susceptible to metamorphic resetting, which could be an issue given that the PPH sequence was metamorphosed to greenschist facies conditions (Polat, 2009). The higher closer temperature and lower mobility of the Sm-Nd system allows it to be an ideal choice, minimizing the probability of post-formation processes disturbing this system.

When all samples from the PPH are plotted on the same isochron, an age of 2681±51 Ma (Figure 6.11, 7.1) is obtained, with an initial $^{143}Nd/^{144}Nd$ isotopic composition of 0.509279±0.000008, corresponding to an $\varepsilon^{143}Nd$=2.3±0.2 (MSWD=6.6, n=24). This isochron includes all the samples, including the tholeiites, which may not be cogenetic, or have derived from the same mantle source (Kitayama and Francis, 2014). Field relationships suggest that the tholeiites, which underlie the Fe-rich lithologies, should be older. The isochron also includes samples from the overlying Fe-rich lavas, which Kitayama and Francis (2014) interpreted as the product of mixing between the tholeiitic magma and the parental Fe-rich magma producing the differentiated intrusive rocks.

The slope on an isochron plot can be taken to have two meanings; an age representing the last isotopic homogenization event (igneous or metamorphic age), or the product of mixing between two sources. The latter would represent a mixing line, which essentially has no geochronological meaning. As such, in order to constrain the age of the PPH sequence we must consider a possible mixing between two sources. In the field, the Fe-rich intrusive ultramafic rocks transition from each lithology with no sharp contact between them, suggesting they are all cogenetic. Furthermore, Kitayama and Francis (2014) have previously indicated that the variations within the geochemical composition of the intrusive rocks represent a fractional crystallization trend, and are reflective of closed-system magmatic processes. If we consider just the intrusive samples on an isochron, we obtain an age of 2713±95 Ma with an initial $^{143}Nd/^{144}Nd$ =0.509249±0.000010, which corresponds to an $\varepsilon^{143}Nd$=2.5±0.2 (MSWD=7.9, n=17) (Figure 7.1a). Thus the age yielded from the isochron of the intrusive samples can be considered representative of the true igneous age of differentiation for these rocks (Figure 7.1a).

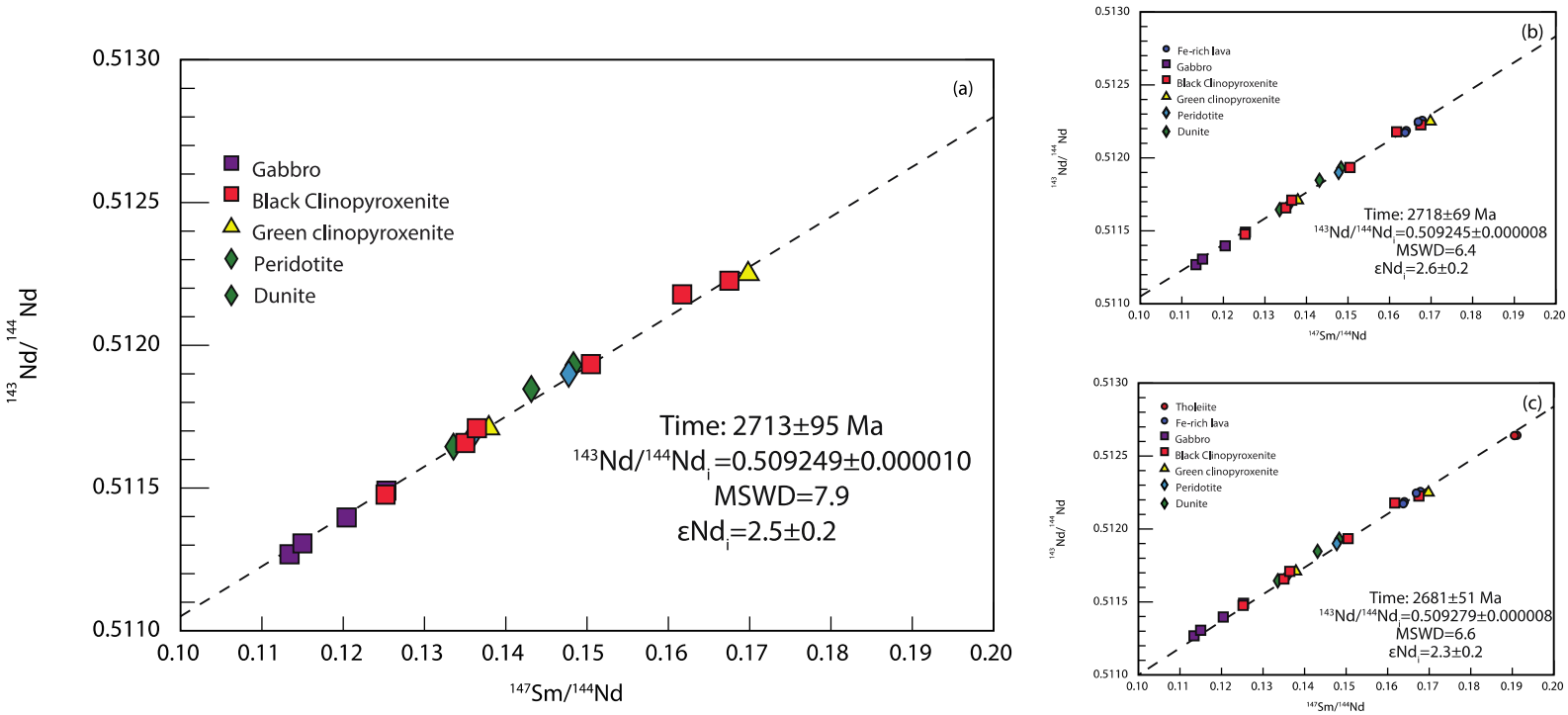

Figure 7.1: Sm-Nd isochrons for the PPH sequence. (a) Sm-Nd isochron for the intrusive samples, (b) Sm-Nd isochron for the Fe-rich samples and (c) Sm-Nd isochron for all lithologies. Regressions (dashed lines) were calculated using ISOPLOT v.4.15 Ludwig (2012), the error on the ages, $^{143}Nd/^{144}Nd$ and εNd_i is 2σ. CHUR values from Bouvier et al. (2008) were used to calcualted εNd_i values. Samples were only excluded from the isochron based on lithology.

Rocks that are co-genetic and derived from the same source will have the same initial isotopic composition, regardless of their Nd concentration. This is because igneous processes, such as fractional crystallization, can affect the Nd concentration, but the ratio of isotopes of heavier elements (e.g. Nd) will not be fractionated through these processes. Correlations between the initial Nd isotopic composition and Nd concentrations of rocks will therefore be reflective of mixing between two end members. Figure 7.2 shows the $^{143}Nd/^{144}Nd$ calculated at the isochron age of 2713 Ma of the intrusive rocks vs. Nd concentrations for all PPH rocks, to investigate this possible mixing between the tholeiites and Fe-rich parental magma. No correlation is observed between the Nd concentration and the calculated initial $^{143}Nd/^{144}Nd_{(2713Ma)}$ ratio of the samples studied here. Furthermore, most ferropicritic lavas samples do not plot on the mixing line

between the tholeiites and parental Fe-rich magmas. In fact, the initial $^{143}Nd/^{144}Nd$ ratio for all ferropicritic lavas are within the error of the calculated initial $^{143}Nd/^{144}Nd=0.509249\pm0.000010$ at 2713 Ma, arguing against them being the result of mixing, at least for their Nd isotopic composition.

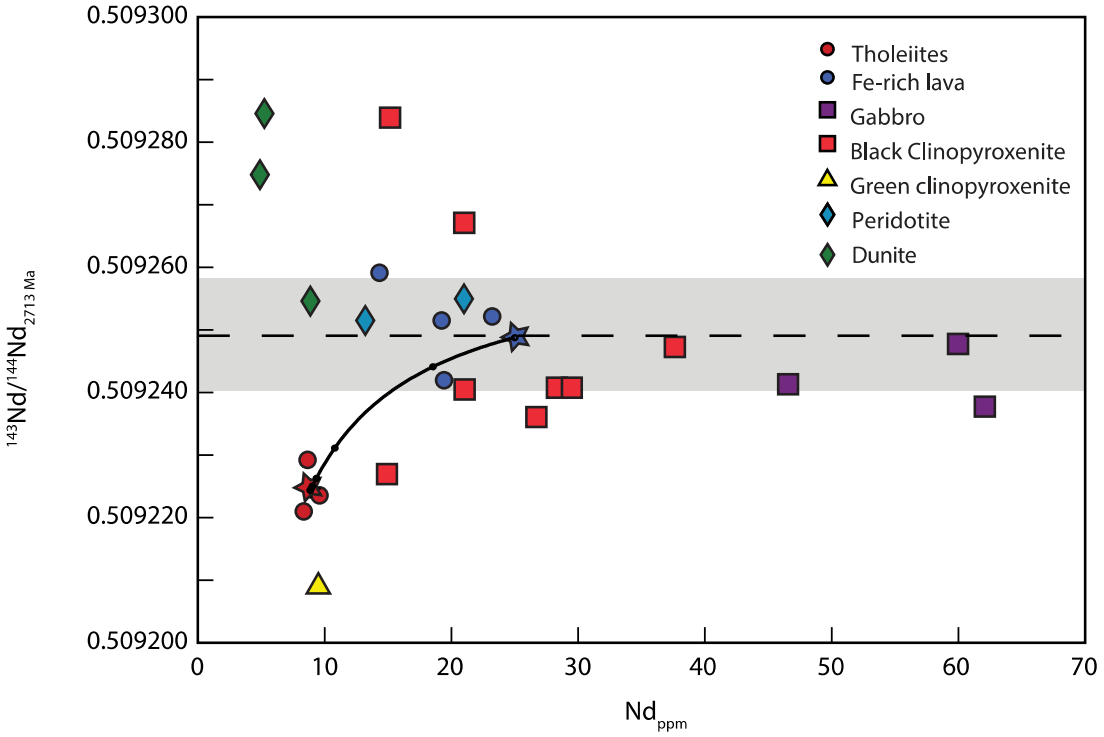

Figure 7.2: $^{143}Nd/^{144}Nd_i$ @ 2713Ma vs. Nd (ppm) for the 18 samples (and 6 duplicates) analysed for their Sm-Nd compositions. The samples all plot within the error given on the $^{143}Nd/^{144}Nd_i$ value from the isochron plotted in Figure 7.1a. The red star is the average Nd_{ppm} and $^{143}Nd/^{144}Nd$ for the analyzed tholeiites. The blue star is the initial isotopic composition from Figure 7.2a and the estimated Nd concentration of the parental ferropiciritic magma from Kityama and Francis (2014).

When the Fe-rich lavas are considered with intrusive rocks on an isochron, the age becomes 2718±69 Ma with the $\varepsilon^{143}Nd=2.6\pm0.2$ (Figure 7.1b). This further suggests that if the ferropicritic lavas are indeed the product of mixing between the tholeiites and the parental Fe-rich magma, their isotopic composition was not affected. In fact, both these ages are unresolvable from the

age of 2681±51 Ma yielded by an isochron when all the samples, including the tholeiites, are considered (Figure 7.1c).

The similarity of the calculated initial $^{143}Nd/^{144}Nd$ compositions of the samples, along with the absence of correlations with Nd concentrations, support that the isochrons obtained here yielded an igneous age, arguing against a relationship that reflects mixing of two distinct geochemical reservoirs, at least for their Sm-Nd isotopic compositions. Therefore, given the fact that the tholeiites and Fe-rich lavas plot on the same isochron as the intrusive rocks, this suggests that the ferropicritic rocks and the tholeiites have the same age and derived from the same mantle source, even if they were produced by different petrogenetic processes. There is the possibility that they could have come from different sources, but these sources would, at their time of formation of the tholeiites and Fe-rich rocks of ~2.7 Ga, have the same Nd isotopic composition.

Whilst various models have been proposed for the petrogenesis of ferropicrites, the Sm-Nd isotopic results presented here can help further constrain these models. If both the tholeiites and Fe-rich rocks have come from the same source, melting of such source would need to produce both lithologies, which exhibit different geochemical characteristics. Kitayama and Francis (2014) suggested that the source could be an olivine cumulate which had crystallized from a deep-seated Hadean magma ocean. This source would have localized enrichments in Fe, Ni and LREE, in order to source the alkaline ferropicrites of the PPH. Melting of this chemically heterogeneous source would allow for both magma that is tholeiitic and Fe-rich in affinity to be produced from the same mantle source, if the Fe-enrichments did not affect the isotopic composition or happened shortly before the melting of the mantle.

Alternatively, it has been suggested that alkaline ferropicrites may derive from a garnet pyroxenite source (Milidragovic and Francis, 2016; Gibson et al., 2002). It has been shown that a garnet pyroxenite source would be capable of melting to produce both tholeiitic and alkaline in affinity melts (Keshav et al., 2004, Hirschmann et al., 2003),. However, these studies (Keshav et al., 2004, Hirschmann et al., 2003), have been on modern oceanic island basalts (e.g. Hawaii), and although Archean ferropicrites are considered to be analogous to modern day OIBs (Milidragovic and Francis, 2014), the geochemical characteristics of the tholeiites are not similar to Hawaiian tholeiitic basalts, but they are closer to typical Archean basalts (Barnes and Arndt, 2019). When plotted in a Th/Yb vs. Nb/Yb variation plot from Pearce (2008), the tholeiites indicate a source between NMORB and EMORB, typical of Archean tholeiites, whilst the Fe-rich lavas source from a more enriched source, equivalent to EMORB (Figure 7.3). However, the geochemical composition of the Fe-rich lavas may not be representative of their original composition (Kitayama and Francis, 2014), as such the gabbro samples have also been plotted in Figure 7.3. The calculated parental magma of the Fe-rich intrusive rocks (Kitayama and Francis, 2014), also suggests a source similar to where the gabbros plot (Figure 7.3) and suggest a source that is more OIB-like in affinity.

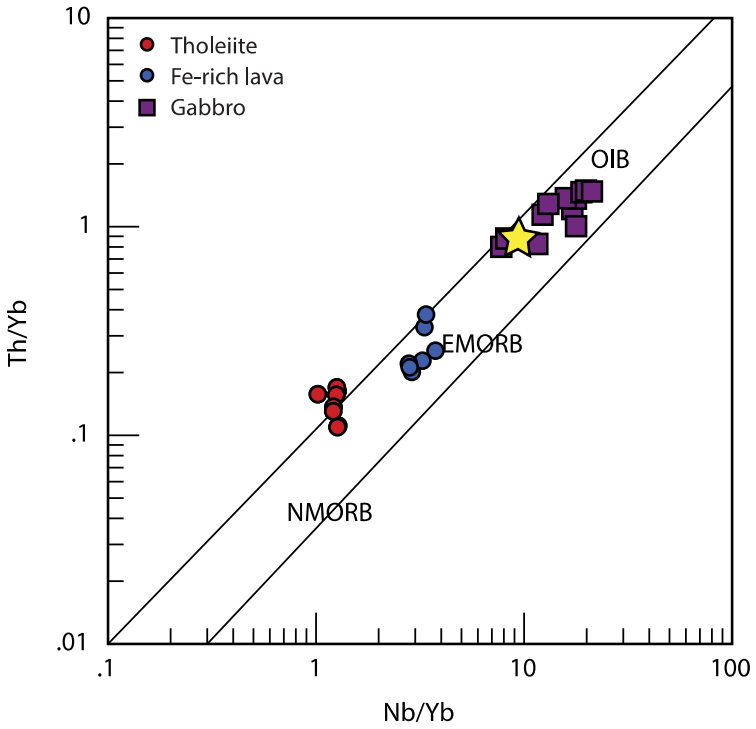

Figure 7.3: Tholeiites (red circles), Fe-rich lavas (blue circles) and gabbro intrusive samples (purple squares) plotted in Nb/Yb vs. Th/Yb discrimination diagram after Pearce 2008. The estimated parental magma (yellow star) as calculated by Kitayama and Francis (2008). OIB – Ocean Island Basalt, E- and N- MORB – Enriched and Normal Mid Ocean Ridge Basalt.

The samples analysed for geochronological dating can be plotted on three separate isochrons – all the samples, the intrusive samples and the Fe-rich samples (Figure 7.1). The ages yielded by these isochrons are resolvable from one another, and are also consistent with surrounding U-Pb dates on zircons of 2.68 - 2.72 Ma from granitic plutons (Corfu and Muir, 1989). This strongly suggests that the Sm-Nd isochron age obtained here for the PPH rocks is reflective of their igneous age. Therefore, we can take the age of the PPH sequence to be 2681±51 Ma, with an initial $\varepsilon^{143}Nd=2.3\pm1.0$. The similarity in the initial $\varepsilon^{143}Nd$ compositions indicate that the tholeiites and Fe-rich lavas have derived from the same mantle source, but any such differentiation that occurred to produce the Fe-rich intrusive rocks and tholeiites must have occurred just prior to formation in order to maintain the same initial isotopic composition. If

the PPH sequence sourced from an olivine cumulate formed during a Hadean magma ocean crystallization event, this source must have been retained in the mantle until 2.7 Ga, and not have been affected by the convecting mantle.

7.2 ^{142}Nd isotopic composition of the Pulpwood-Playter Harbour sequence

One of the proposed hypotheses for the petrogenesis of ferropicrites is that they may have derived from Fe- and Si-enriched mantle domains that differentiated during the crystallization of a magma ocean (Francis et al., 1998; Kellog et al., 1999; Goldstein and Francis, 2014). Silicate fractionation resulting from this crystallization will fractionate lithophile element ratios such as Sm/Nd, and given that magma ocean episodes are expected to occur during the Earth's earliest times (i.e during the Hadean), the differentiation of these reservoirs will be recorded in the short-lived ^{146}Sm-^{142}Nd system. In other words, if the source of ferropicrites is a mantle domain that differentiated during the Hadean, and was not homogenized by mantle convection, it will be characterized by ^{142}Nd anomalies. If mantle derived rocks sourced from this reservoir after the Hadean, it will reflect these deviations.

In order to test this hypothesis, 15 samples from various lithologies of the PPH sequence were analyzed for ^{142}Nd isotopic compositions. Most of the samples yielded slightly negative μ^{142}Nd values ranging from +0.4 to -5.4, with no resolvable differences in μ^{142}Nd values between the various lithologies or rocks with different Nd concentrations (Figure 7.4). The PPH dunites and tholeiites, which are characterized by the lowest Nd concentrations of the suite (< 10 ppm), have undistinguishable μ^{142}Nd values from the gabbros that have much higher (> 40 ppm) Nd concentrations (Fig. 7.4). This indicates that even if the Nd concentrations of some rocks were affected by post-emplacement processes, it did not affect their ^{142}Nd isotopic composition.

Major and trace element compositions of the Fe-rich lavas can be explained by mixing between the parental magma sources of the tholeiitic lavas and intrusive ferropicritic rocks (Kitayama and Francis, 2014). However, a similarity in ^{143}Nd and ^{142}Nd isotopic composition suggests that either the tholeiitic and ferropicritic magma derived from a chemically heterogeneous but isotopically homogeneous source, or that they derived from the same mantle source.

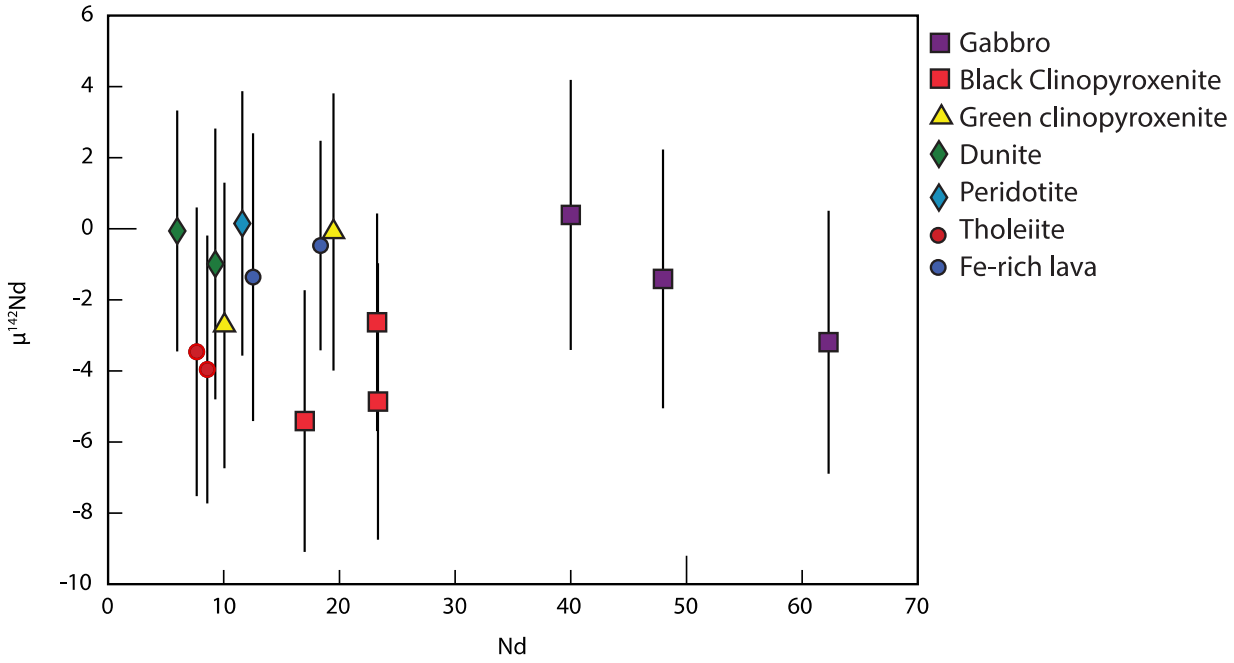

Figure 7.4: $\mu^{142}Nd$ vs. Nd (ppm) for the 15 samples of varying lithologies analysed for ^{142}Nd isotopic composition.

The average for all the rocks analyzed gives $\mu^{142}Nd$ = - 2.0 ±3.9 (n=15, 2SD). This average is the same within the error of the measured terrestrial Nd standard ($\mu^{142}Nd$ = 0 ±4), which is representative of the modern terrestrial mantle. The absence of resolvable ^{142}Nd variability would *a priori* suggests that there is no evidence of early silicate differentiation events recorded in the source of the PPH rocks. Given the short stirring time estimated for the Archean mantle of 100-250 Ma (e.g. Allègre and Lewin, 1995), chemical heterogeneities formed more than 4.0

billion years ago should have been eradicated by 2.7 Ga when the ferropicrites were emplaced. Nevertheless, when evaluating the μ^{142}Nd results closely, it is plausible that the average μ^{142}Nd of the PPH rocks could be statistically different from the modern mantle, but not resolved because of the ±4ppm external analytical precision we currently typically get on ^{142}Nd/^{144}Nd measurements. If a number of samples were derived from a mantle source with a μ^{142}Nd value identical to the modern terrestrial mantle, a normal distribution around μ^{142}Nd = 0 would be expected. Figure 7.5 shows the comparison between the μ^{142}Nd values for the PPH and BCF rocks analyzed here and modern mantle-derived rocks (ocean island basalts and mid-ocean ridge basalts). Out of the 15 PPH samples analysed, 13 yield negative μ^{142}Nd values, representing 87% of the sample population studied here. In contrast, only 36% of the modern-mantle derived rocks analyzed so far (n=70) show negative μ^{142}Nd values, and the average μ^{142}Nd for all the samples is +0.9 ±0.8 (2SE).

While the current analytical precision does not allow to resolve the average μ^{142}Nd value of -2.0 ±3.9 of the PPH rocks from that of +1.0 ±4.0 from the modern terrestrial mantle, the probability that 13 out of 15 rocks analyzed yielded negative μ^{142}Nd values, if they were derived from a mantle isotopically identical to the modern terrestrial mantle, is extremely small (0.32%).

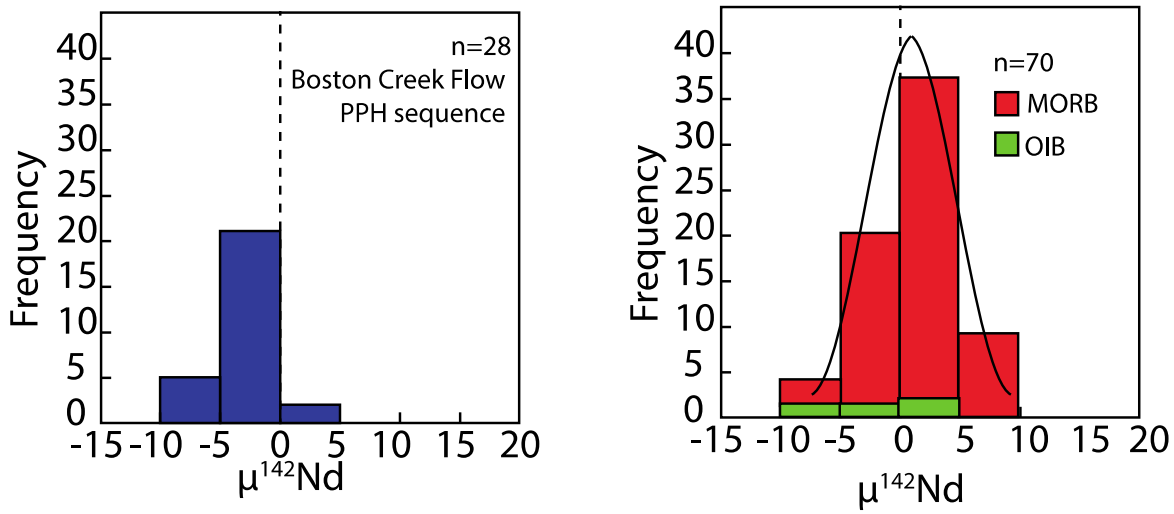

Figure 7.5: Histogram of $\mu^{142}Nd$ values for the PPH sequence (left) compared to $\mu^{142}Nd$ values for modern mantle rocks from the literature (right). MORB: Mid-ocean ridge basalts; OIB: ocean island basalts. BCF data from Putchtel et al. (2019). MORB and OIB data from Andreasen et al. (2008), Boyet and Carlson (2006), Caro et al., (2006), Garçon et al. (2018), Horan et al. (2018), Jackson et al. (2012), Murphy et al. (2010), and Peters et al. (2018)

Furthermore, it is interesting to note that nine 2.72 Ma rocks from the Boston Creek Flow (Abitibi greenstone belt), show comparable slightly negative $\mu^{142}Nd$ values to the PPH rocks averaging at -3.8 ±2.8 (Puchtel et al., 2018) (Figure 7.6). The Boston Creek Flow rocks share geochemical affinities with the PPH ferropicrites, with compositions that are also enriched in Fe and Ti, and identical initial $\varepsilon^{143}Nd$ of +2.5, suggesting they could derive from similar mantle source(s) and produced through similar processes. Puchtel et al., (2018) concluded that the ^{142}Nd composition of the source of the Boston Creek rocks was unresolvable from the modern terrestrial mantle, but all the samples they analyzed yielded negative $\mu^{142}Nd$ values. Given that there is now report of ^{142}Nd negative anomalies in 26 of 28 Archean ultramafic komatiitic and ferropicritic samples analyzed in the southern Superior Province (a probability of 0.0016% if their mantle source had no anomaly), in the next sections, we discuss the implications of the ferropicrite source being characterized by negative anomalies in ^{142}Nd, and we will compare these results with those obtained from the long-lived ^{147}Sm-^{143}Nd system.

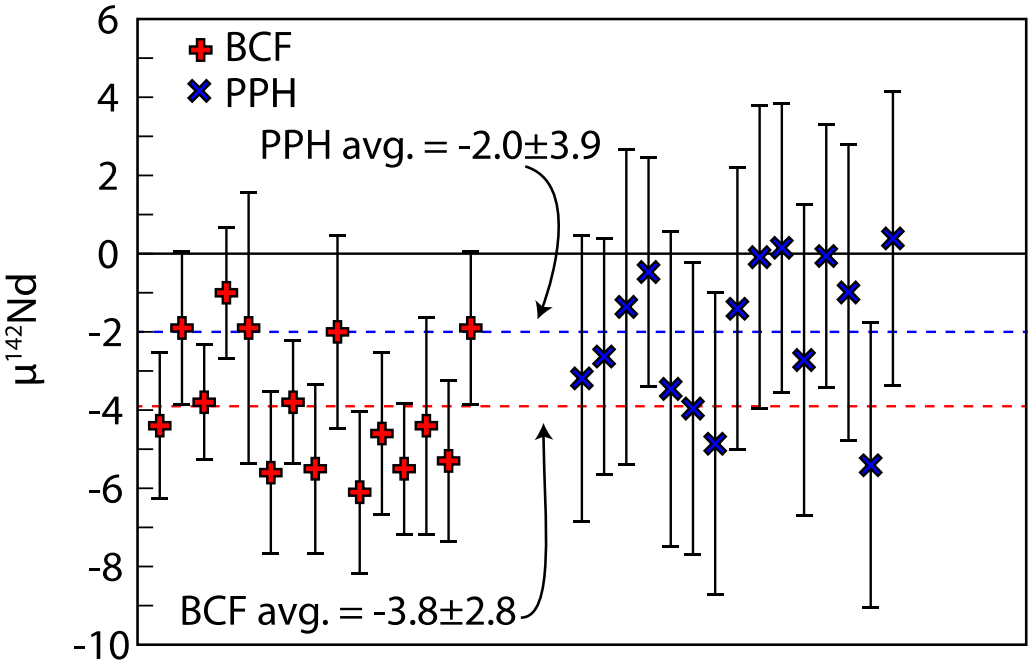

Figure 7.6: Comparison of PPH μ^{142}Nd data with the BCF μ^{142}Nd data from Puchtel et al. (2018). The μ^{142}Nd values despite unresolvable show homogeneity in being negative for 22 out of the 24 samples. Error bars are calculated at 2SD. BCF samples shown include 6 duplicate samples

7.3 ^{142}Nd and ^{143}Nd isotopic composition and early evolution of the Pulpwood-Playter Harbour mantle source

Since both ^{143}Nd and ^{142}Nd are decay products Sm isotopes (^{147}Sm and ^{146}Sm, respectively), silicate differentiation events occurring during the first 500 Ma (Hadean period) of the Earth's history, while ^{146}Sm is still extant, will affect both short-lived ^{146}Sm-^{142}Nd and long-lived ^{147}Sm-^{143}Nd systems. Fractionated reservoirs with a high Sm/Nd ratio will evolve towards higher ^{143}Nd/^{144}Nd and ^{142}Nd/^{144}Nd ratios, and those with low Sm/Nd ratios will evolve towards lower ^{143}Nd/^{144}Nd and ^{142}Nd/^{144}Nd ratios. However, fractionation events occurring after the Hadean will only affect the ^{147}Sm-^{143}Nd system, since ^{146}Sm is extinct. These differentiated reservoirs will evolve with different Sm/Nd and to different ^{143}Nd/^{144}Nd ratios, but they will have the same

^{142}Nd compositions. Differentiation events occurring at different times, therefore, can result in the decoupling of the short-lived ^{146}Sm-^{142}Nd and the long-lived ^{147}Sm-^{143}Nd systems.

The PPH mantle has a μ^{142}Nd value of -2.0±3.9, reflecting a source evolution with a Sm/Nd ratio that was lower than the modern mantle. This result also suggests that the source of ferropicrites was more enriched in incompatible elements than the modern mantle. However, their initial ^{143}Nd/^{144}Nd composition and ε^{143}Nd (t=2681 Ma) value of +2.3±0.2 translates a source that evolved with suprachondritic Sm/Nd ratio and that was more depleted in incompatible elements than chondrites.

In the next sections, we discuss models that can explain the combined ^{143}Nd and ^{142}Nd observations of the PPH ferropicrites.

7.3.1 Source mixing to produce the Pulpwood-Playter Harbour sequence

It has been proposed that the petrogenesis of ferropicrites arise from melting of a silica-deficient garnet pyroxenite (Jennings et al. 2016). This garnet pyroxenite source would be produced from the metasomatism of peridotitic mantle by eclogite melts (Figure 7.7).

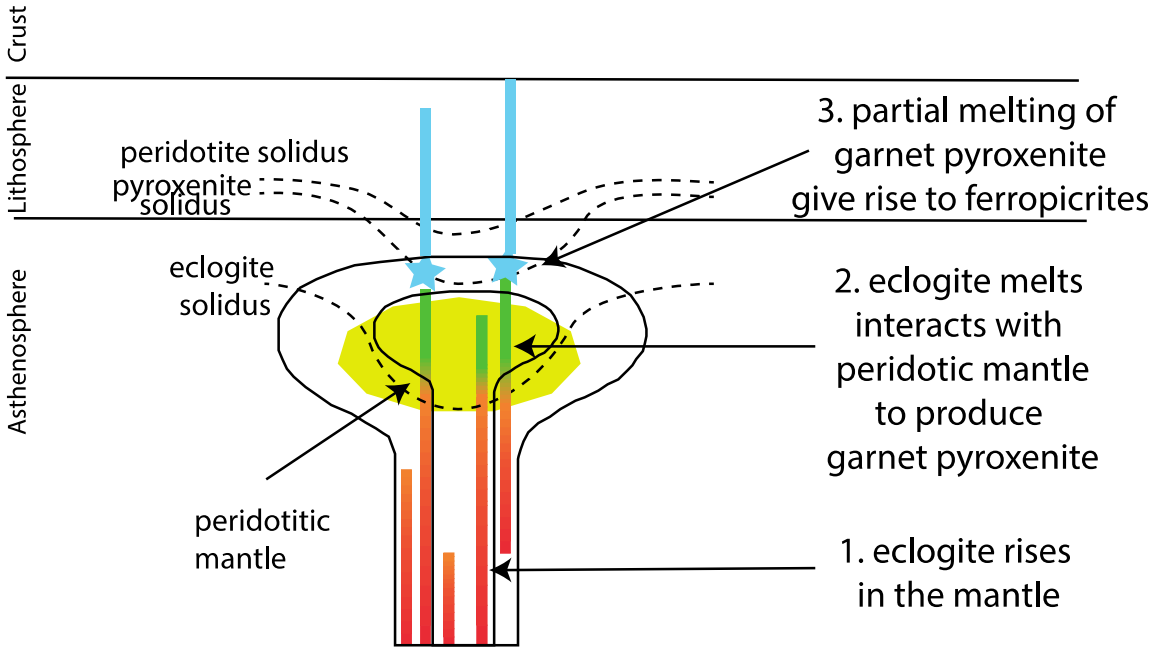

Figure 7.7: Modified schematic of an heterogeneous mantle plume (Jennings, 2016). Melting of eclogitic material (green), formed from the metamorphism of subducted basaltic crust, produced a melt that interacts with peridotic mantle to produce pyroxenite (yellow). In order to have a ^{142}Nd anomaly, the protolith of this eclogitic material would need to be Hadean basaltic crust.

Subducted oceanic crust is the likely mechanism proposed to introduce eclogite in the mantle via metamorphism of the basaltic crust (Green and Ringwood, 1967). The origin of the negative ^{142}Nd anomalies in the PPH ferropicritic rocks could therefore stem from this eclogitic component rather than from the mantle itself. However, in order for the eclogite material to have deficits in ^{142}Nd compared to the "normal" depleted mantle, its basaltic crustal protolith would need to be produced in the Hadean (Figure 7.8). The extent of the negative μ^{142}Nd value for this Hadean basaltic crust would depend on its age and Sm/Nd ratio. O'Neil and Carlson (2017) have proposed that ~2.7 Ga tonalites and trondhjemites from the Hudson Bay terrane of the Northeastern Superior Province were produced from the reworking of 4.2-4.3 Ga basaltic crust. Because these tonalites and trondhjemites cover a large extent of the Hudson Bay

terrane, this Hadean basaltic crust appears to have been an important crustal reservoir that survived at least until the Neoarchean, and could also be the origin of some eclogitic material in the mantle during the Neoarchean. Figure 7.8 illustrates the Nd isotopic evolution of enriched basaltic material (turned to eclogite), derived from the depleted mantle at 4.3 Ga and characterized by a $^{147}Sm/^{143}Nd$ ratio of 0.15, which would be similar to the Hadean mafic reservoir involved in the formation of the Neoarchean tonalites and trondhjemite of the Hudson Bay terrane (O'Neil and Carlson, 2017). A 4.3 Ga mafic crustal reservoir with such a low Sm/Nd ratio would, however, evolve to a $\mu^{142}Nd$ value of ~-11 and $\varepsilon^{143}Nd$ of value of ~-8 at 2681 Ma, much lower than those of the PPH ferropicrites. Melts from this Hadean eclogitic material would therefore need to metasomatised the "normal" peridoditic mantle at ~2.7 Ga ($\mu^{142}Nd=0$ and $\varepsilon^{143}Nd=+\sim4$) to produce the silica-deficient pyroxenite. This would result in isotopic mixing between the Hadean eclogitic material and Neoarchean peridoditic mantle. If this metasomatism event was also the cause of the LREE enrichment of the ferropicritic rocks, it would need to occur shortly prior to the eruption of the ferropicrites (~2.7 Ga), for the initial $^{143}Nd/^{144}Nd$ to remain relatively close to the depleted mantle composition. Any post 4.0 Ga LREE enrichments would have no effect on the $^{142}Nd/^{144}Nd$ ratio.

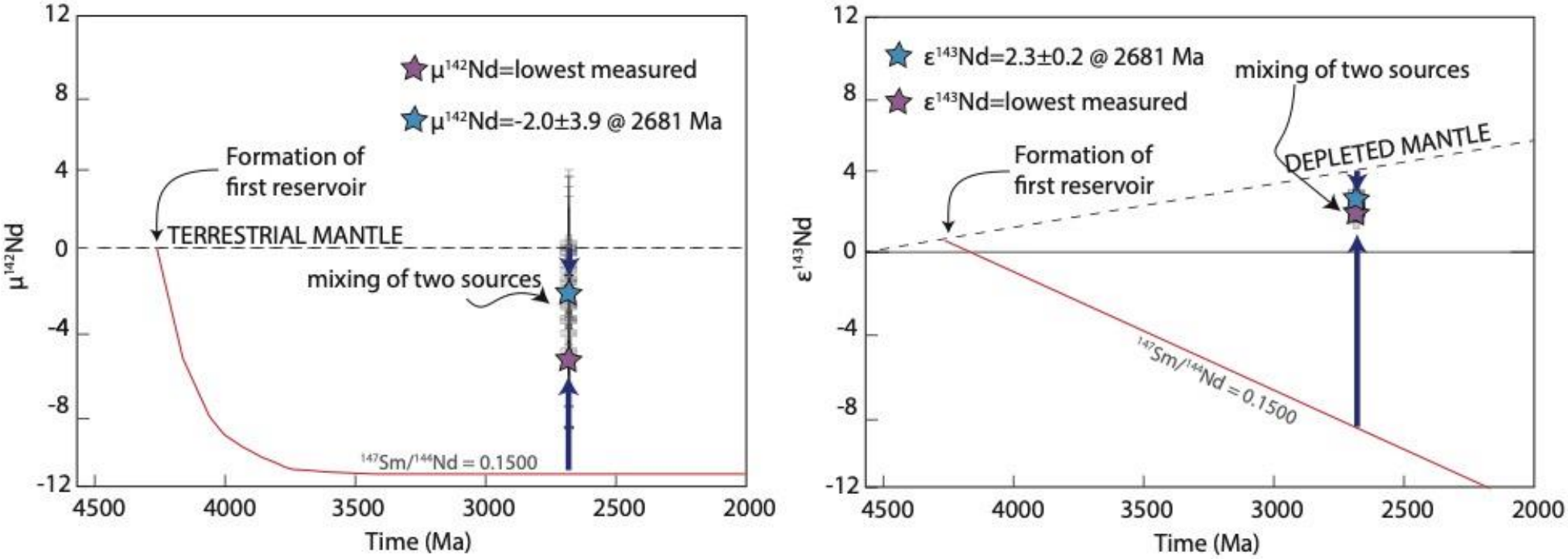

Figure 7.8: Plausible binary mixing model for the source of ferropicrites that would involve a Hadean component mixing with the modern mantle. The Hadean basaltic component is characterized by $^{147}Sm/^{144}Nd$ =0.1500. At ~2.7 Ga this source is characterized by an low $\mu^{142}Nd$ sand $\varepsilon^{143}Nd$ values, and mixes with a peridotitic mantle source characterized by $\mu^{142}Nd$=0. This results in a source characterized by slightly negative $\mu^{142}Nd$ and positive (with respect to CHUR) $\varepsilon^{143}Nd$ values.

In this model, the negative $\mu^{142}Nd$ value of the ferropicritic rocks arises from the involvement of a Hadean basaltic crust, turned into eclogitic material, which interacts with peridotite to form the pyroxenitic source of the Fe-rich magmas. The petrogenesis of the PPH tholeiites however do not require the participation of eclogite and are likely derived from the melting of "normal" peridotitic mantle (Figure 7.9).

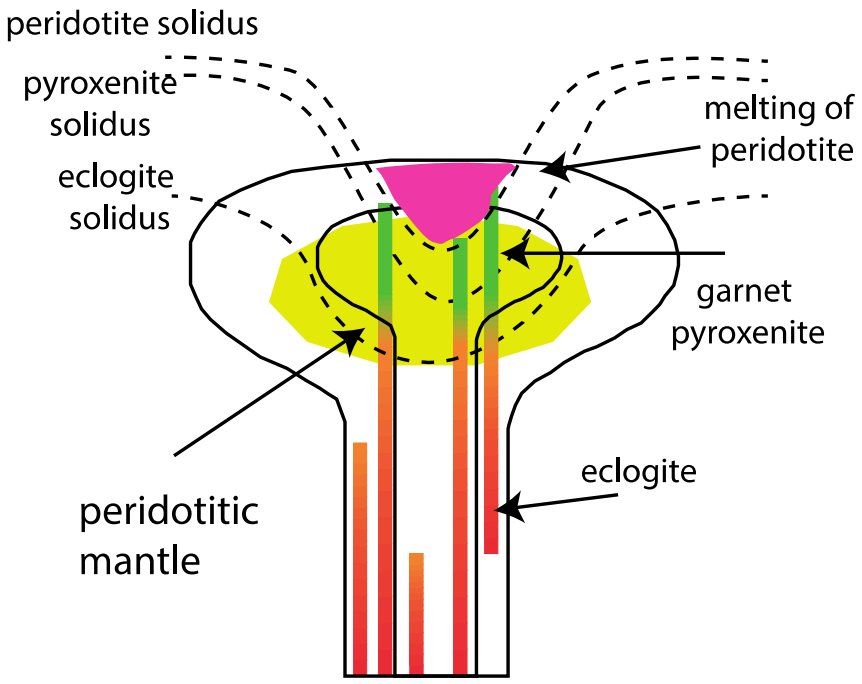

Figure 7.9: Modified schematic after Jennings, 2016, illustrating the melting of a heterogeneous plume to produce both tholeiitic basalts from the melting of peridotite and ferropicrites from the melting of pyroxenite (yellow)

The PPH tholeiites, however, have the same initial Nd isotopic composition, with respect to both $\mu^{142}Nd$ and $\varepsilon^{143}Nd$ as the ferropicritic rocks. This would suggest that the metasomatic event forming the pyroxenite source of the Fe-rich magma, imprinted its Nd isotopic composition in some peridotite without forming pyroxenite. Furthermore, if the tholeiites were

to derive from the peridotitic component it would be characterized by the same μ^{142}Nd values as the terrestrial mantle. This is not the case with the PPH sequence, both tholeiite samples analysed display a slightly negative μ^{142}Nd values. It has been proposed that some tholeiitic Hawaii basalts were sourced from pyroxenite (Keshav et al., 2004; Hirschmann et al., 2003) and that Archean ferropicrites could be analogues to modern day OIBs (Milidragovic and Francis, 2014). It could therefore be argued that the same pyroxene source with a negative μ^{142}Nd value produced both the PPH ferropicrites and tholeiites with identical Nd isotopic compositions. However, the trace element patterns of modern OIB tholeiites that have derived from a pyroxenite source show varying degrees of LREE enrichments, and this is not observed in the PPH tholeiites. Therefore, we find this scenario to be unlikely and would argue that a more suitable model would need to better account for the ^{142}Nd composition in the source of both the PPH ferropicrites and tholeiites.

7.3.2 Single source differentiation evolution of the Pulpwood-Playter Harbour sequence

The slightly negative ^{142}Nd anomalies found in the PPH rocks suggest that their source has been differentiated in the Hadean. This supports the hypothesis that ferropicrites may have derived from an olivine cumulate that crystallized from a deep-seated Hadean magma ocean (Goldstein and Francis, 2008; Kitayama and Francis, 2011). Assuming the PPH ferropicrites have derived from a single reservoir formed from a single differentiation event, we can use the ^{143}Nd and ^{142}Nd observations to model the isotopic evolution of such a reservoir and provide time constraints as to when this source differentiated and acquired its Sm/Nd ratio.

Figure 7.10 shows possible models that can explain the ε^{143}Nd and μ^{142}Nd of the PPH source, assuming this source differentiated in one single event. Our results show that an extremely

early silicate differentiation event, between 4.55 Ga and 4.47 Ga, of a mantle source characterized by a $^{147}Sm/^{144}Nd$ ratio between 0.2011 and 0.2067, would be required to satisfy both observed $\varepsilon^{143}Nd$ and $\mu^{142}Nd$ values. A later differentiation event would require a lower Sm/Nd ratio for the source to evolve to the $\mu^{142}Nd$ observed in the PPH rocks, but this would also lead to a lower $\varepsilon^{143}Nd$ at 2.7 Ga, inconsistent with the values obtained from the ^{147}Sm-^{143}Nd isochrons. Such a mantle source with $^{147}Sm/^{144}Nd$ ratio between 0.2011 and 0.2067 would be more enriched in incompatible elements that the present-day MORB source, which is characterized $^{147}Sm/^{144}Nd$ ratio between 0.23 and 0.25 (Albarède, 2001). Similar early silicate differentiation events have also been suggested to explain the ^{143}Nd and ^{142}Nd compositions of Eoarchean rocks from other locations, such as SW Greenland and Northern Labrador (Rizo et al., 2011; Morino et al., 2018), and could be related to the solidification of magma oceans formed after the Moon-forming impact. While the exact timing of this last giant impact to Earth is still under debate, increasing evidence from the oldest rocks on Earth (O'Neil et al., 2008), the I-Xe age of the Earth's atmosphere (Swindle et al., 1986), the oldest zircons found on Earth (Wilde et al., 2001), and the oldest lunar rocks and minerals (Kleine et al., 2005, Touboul et al., 2007) suggest the first terrestrial and lunar crust formed between 4.5 Ga and 4.3 Ga. While a silicate differentiation event between 4.55 Ga and 4.47 Ga is possible to create the ferropicrites' source, a more difficult question to answer is how such a mantle reservoir survived stirring and mixing by mantle convection for half of the Earth's existence, from the Hadean until 2.7 Ga. The answer to that question might be related to the different chemical composition of this Fe-rich source, its viscosity and density contrast with the ambient mantle, but these are only speculations that are beyond the focus of this thesis.

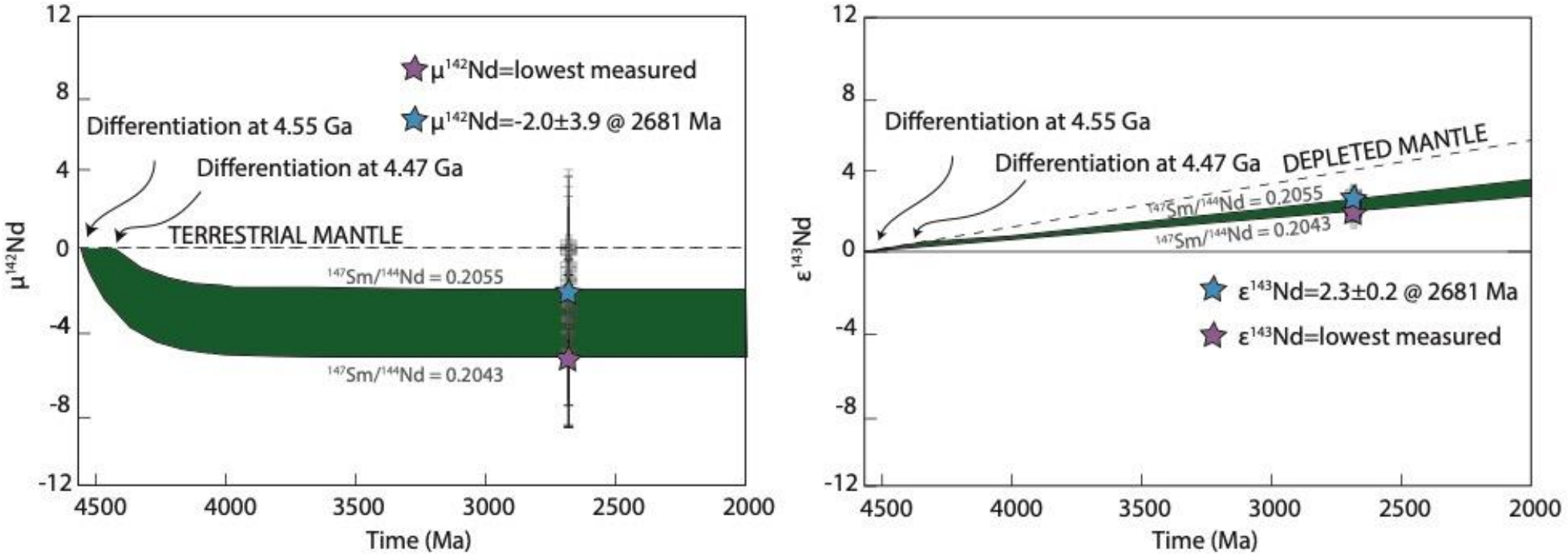

Figure 7.10: Plausible models that explain both $\varepsilon^{143}Nd$ and $\mu^{142}Nd$ values of the PPH rocks. Right: Evolution of a mantle source differentiated at 4.556 Ga and characterized by a $^{147}Sm/^{144}Nd$ ratio between 0.2043 and 0.2067. Left: Evolution a mantle source differentiated at 4.468 and characterized by a $^{147}Sm/^{144}Nd$ ratio between 0.2055 and 0.2011. Models use a half-life of 103 Ma for ^{146}Sm (Marks et al., 2004) an initial $^{142}Nd/^{144}Nd$=1.14190 (Gannoun et al., 2011). The $\varepsilon^{143}Nd$ model uses $\lambda=6.54*10^{-6}$ for ^{147}Sm, an initial $^{143}Nd/^{144}Nd$=0.506702, calculated from depleted mantle values after Bouvier et al. (2008). $\varepsilon^{143}Nd$ is calculated from values for CHUR from Bouvier et al. (2008). Blue star – average $\mu^{142}Nd$ =-2.0±3.9, purple star – lowest $\mu^{142}Nd$ =-5.41±3.68, grey star – individual sample measaments and associated errors.

7.4 ^{182}Hf-^{182}W systematics of the Pulpwood-Playter Harbour sequence

The short-lived ^{182}Hf-^{182}W ($t_{1/2}$=8.9 Ma) could provide additional information to the geological history of the source of the PPH rocks. This isotope system becomes extinct after 50 Ma of the Earth's history, making it an ideal tracer of extremely early geological events. Since both the Hf-W and Sm-Nd system have similar behaviour during igneous processes, where the parent is more compatible than the daughter, the two systems should be coupled during silicate differentiation events. Early depleted reservoirs in incompatible elements will be characterized by excesses in both ^{142}Nd and ^{182}W, and enriched reservoirs by deficits in ^{142}Nd and ^{182}W.

The high mobility of W in crustal fluids, however, is an important concern when working with altered and metamorphosed rocks, since their W isotopic value might not be reflective of the mantle source that gave rise to the rocks, but rather W that has been remobilized by fluids. Therefore, when analysing in W isotopic values, the origin of W needs to be considered first in order to understand if it is reflective of the mantle source. After this, we made an attempt to acquire ^{182}W compositions of selected rock samples.

7.4.1 Origin of W in the Pulpwood-Playter Harbour rocks

Twenty-nine samples of varying lithologies were analyzed for their W concentrations. Tungsten is a highly incompatible element during partial melting and fractional crystallization (e.g. Shearer and Righter, 2003), with similar behaviour to Ba, U and Th (Arevalo and McDonough, 2008).

There appears to be no overall correlation between W concentration and PPH lithologies, and no clear magmatic behaviour can be established by attempts to correlate W with magmatic differentiation indicators (i.e MgO).

When the lithological groups are taken individually, only the black clinopyroxenites seem to show an increase in W concentration with increasing Th and U, although this correlation is not as defined as for U vs. Nb or Th (Figure 6.10). This suggests that W concentrations for most PPH rocks are not controlled by primary magmatic processes, but are likely remobilized by secondary processes. There is also no broad correlation between W and differentiation indices such as MgO (Figure 6.7), except perhaps for the black clinopyroxenites, showing a slight increasing trend with fractionation, as the MgO content decreases (Figure 7.11).

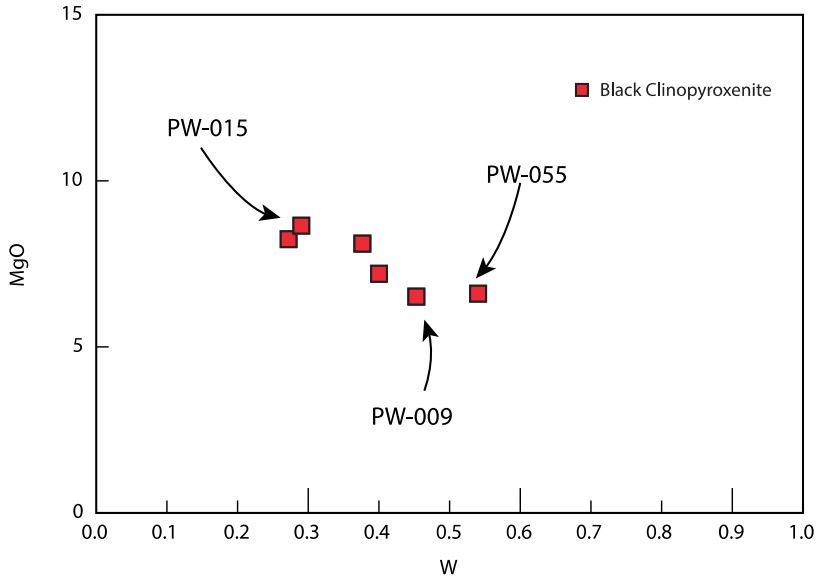

Figure 7.11: MgO (wt. %) vs. W (ppm) for the black clinopyroxenites. Similar to the behaviour of U and Th, as MgO content decreases, W content correlates by a slight increase.

Because of this evidence of remobilization of W within the PPH rocks, it is difficult to clearly establish the primary character of the W concentrations and thus the isotopic composition should be interpreted with caution. Overall, immobile elements, such as REEs and HFSEs

demonstrate that they were generally immobile during post-formation processes and show a correlation Zr (Kitayama and Francis, 2014). However, because ^{182}W anomalies can only be produced within the first 50 Ma of the Earth's history, any deviations of the $^{182}W/^{184}W$ from the terrestrial standard implies that a process fractionated Hf from W in the Hadean, regardless of if the exact origin of W in the rock.

7.4.2 The ^{182}W isotope composition of the Pulpwood-Playter Harbour source

Samples of varying composition (3 black clinopyroxenites, 1 green clinopyroxenite and 1 dunite) were analysed for their ^{182}W isotopic composition. Of these samples 4 presented unresolvable anomalies from the Alfa Aesar standard, which represents the modern mantle ($\mu^{182}W=0$). PW-055, a black clinopyroxenite yielded a positive $\mu^{182}W$ value of 14.14±6.69. Sample yield, and monitoring of other isotopes and isobaric interferences (Figure 6.14, Table 6.4) suggests that this sample was not affected by isotopic fractionation and the $\mu^{182}W$ value is reflective of the sample. As with the $\mu^{142}Nd$ results, $\mu^{182}W$ results were compared with W concentrations in order to determined if there is a correlation between the two (Figure 7.8)

Analytical problems that could affect ^{182}W measurements have recently been reported (e.g. Cook and Schönbachler, 2016). These analytical artefacts relate to preferential loss (e.g. absorption of W by the Teflon used in the laboratory) of some of the W isotopes during chemical extraction procedures of W from the rock matrix. If some of the W isotopes are lost during these procedures, then the measured W isotopic composition of a rock might reflect ^{182}W deviations that are not related to radiogenic ingrowth.

Measuring other W isotopes, besides ^{182}W, can monitor preferential loss of W isotopes. For example, ^{183}W is a stable isotope, and its composition in rocks should be the same as in the

standards. Any variability in ^{183}W would reflect some analytical issues, and would call into question the meaning of any ^{182}W measured. During our analytical sessions, ^{183}W was monitored, and none of the samples showed $\mu^{183}W$ deviations from the standard (Table 6.4, Figure 6.14). Therefore, there is no evidence to suggest that there is an analytical problem with this result, and we discuss below the implications of this ^{182}W variability. There also appears to be no correlation between the W concentrations and $\mu^{182}W$ composition (Figure 7.12).

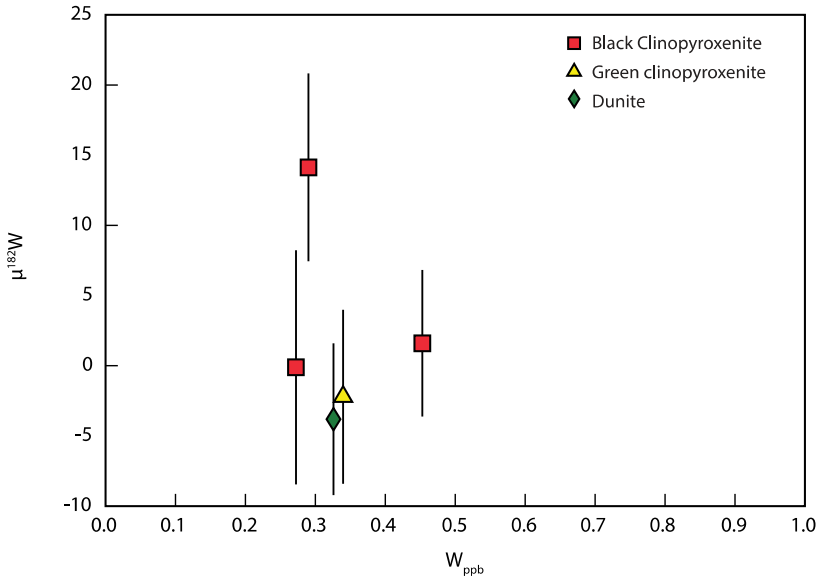

Figure 7.12: $\mu^{182}W$ vs. W concentration for the samples analysed for $\mu^{182}Nd$ isotopic composition – there is no correlation between W concentration and sample $\mu^{182}W$ value. Error bars are 2SE

Early silicate differentiation has been proposed to explain the increasing evidence of positive ^{182}W anomalies measured in 4.3 Ga to 2.7 Ga mantle-derived samples (Puchtel et al., 2018; Rizo et al., 2016; Liu et al., 2016; Puchtel et al., 2016; Touboul et al., 2012). The problem with this hypothesis to explain the ^{182}W value measured in the PPH rock is that ^{182}W and ^{142}Nd variations in these rocks do not correlate positively (Figure 7.14). Given the short half-life of ^{182}Hf, silicate differentiation events occurring early enough to produce ^{182}W variability should create a large

imprint on ^{142}Nd, which is not the case. The rocks analyzed here show slightly negative ^{142}Nd anomalies, and one of the samples analyzed yielded a positive ^{182}W anomaly (Fig. 7.14). This apparent decoupling is not uncommon, and has been observed in Hadean (i.e. Touboul et al., 2014; O'Neil et al., 2008) and Archean mantle derived rocks (i.e Puchtel et al., 2018; Touboul et al., 2012; Boyet and Carlson, 2005; .

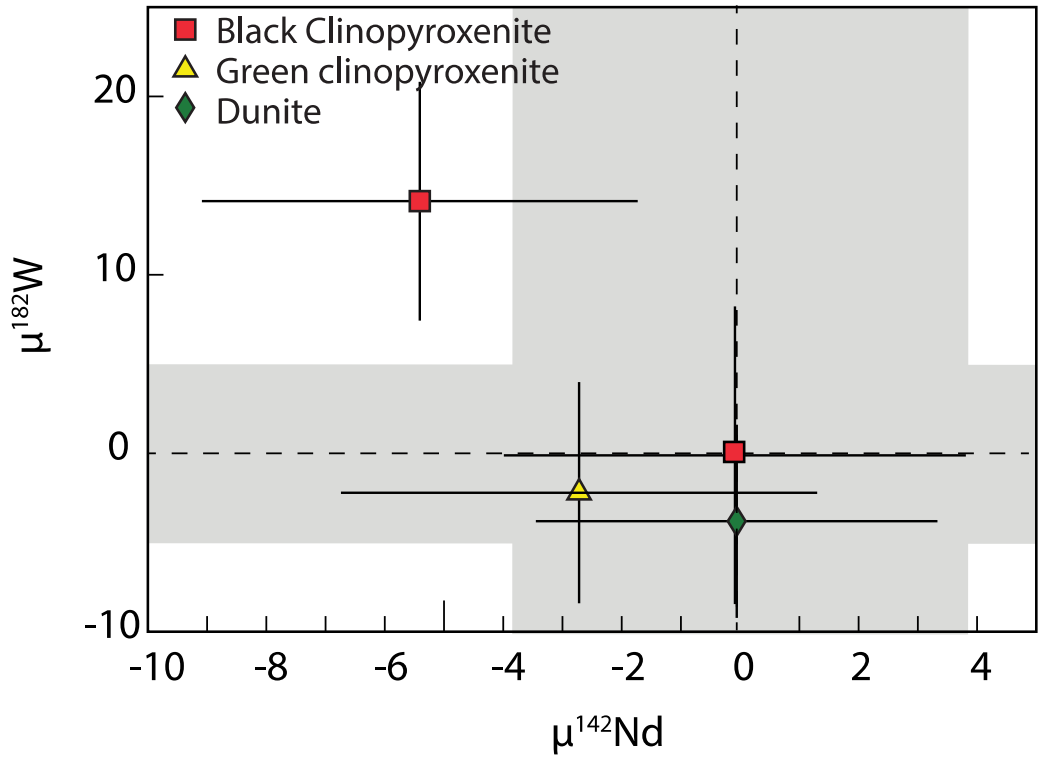

Figure 7.13: μ^{142}Nd vs. μ^{182}W for 4 samples that were analysed for both Nd and W isotopic compositions. The grey bars represent 2SD on the standards.

This sample with a positive ^{182}W anomaly (ε^{182}W = +14.1±6.7) is in fact the PPH sample with the lowest μ^{142}Nd value of -5.4±3.7. Decoupling of ^{182}W and ^{142}Nd has widely been observed in the

geological record, and could suggest that short-lived isotope systematics reflect more than one single event of early silicate differentiation. A differentiation event during the first 50 Ma of Earth's history (i.e. while ^{182}Hf is still decaying) would affect both the ^{182}W/^{184}W and ^{142}Nd/^{144}Nd ratios, while a differentiation event occurring after the extinction of ^{182}Hf, but before that of ^{146}Sm, would affect the ^{142}Nd/^{144}Nd ratio only. Figure 7.15 shows, however, that it is difficult to explain ^{182}W, ^{142}Nd and ^{143}Nd observations in the PPH rocks, even with multiple differentiation events.

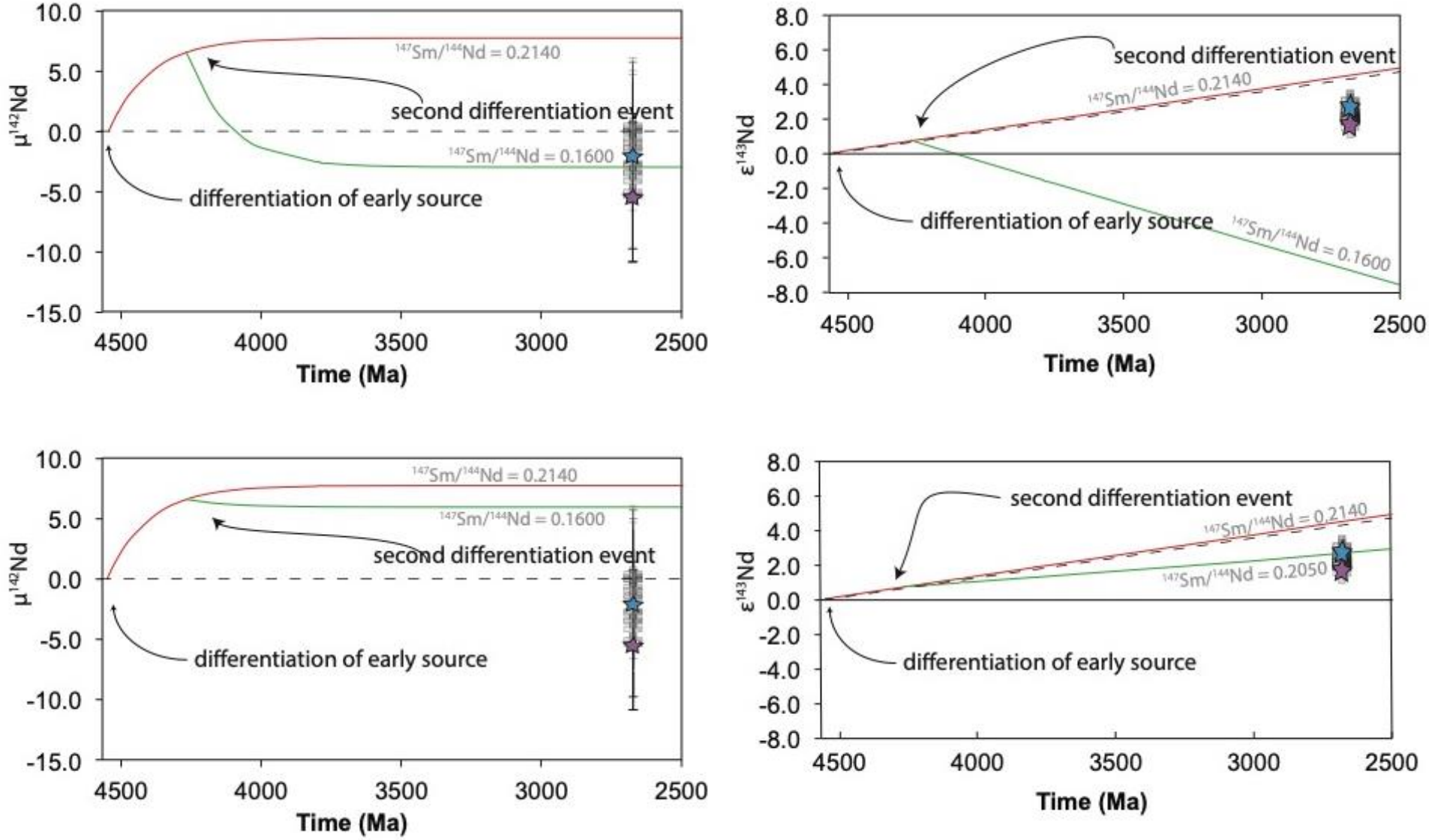

Figure 7.14: Two-stage differentiation model attempting to explain 182W, 142Nd and 143Nd of PPH source. An early differentiation event taking place during the existence of 182Hf would result in evolution of the red line, a second differentiation event would take place after 4.51 Ga, but before 4.0 Ga whilst 146Sm is still extant. An early differentiation event (red line) would fractionate a reservoir to evolve to an excess in both μ182W and μ142Nd. A second fractionation event, taking place after 182Hf has become extinct would only affect the 146Sm-142Nd system. However, manipulation of this model suggests that no matter when, or to what degree the fractionation events taking place would not produce a source that has the μ142Nd and ε143Nd values that we observe in the PPH sequence.

There are other possible scenarios to explain decoupled ^{182}W and ^{142}Nd values. Metal-silicate segregation will fractionate only the Hf/W ratio, since W is siderophile, while Hf, Sm and Nd are all lithophile. Therefore, the ^{182}W variability in the mantle can be created during events related to core formation, which will not affect the Sm-Nd system. Another possibility to explain ^{182}W positive anomalies in ancient mantle sources is that these are lacking their full complement of late-accreted chondritic material that is now present in the modern mantle. Late accretion, or "late veneer", is a widely accepted hypothesis that explains highly siderophile element (HSE) abundances in the mantle, given that these are found in higher abundances than expected for core-mantle equilibrium and in chondritic relative proportions. As little as 0.5 wt.% of the Earth's mass would lower the ^{182}W of the mantle by 15 ppm, as chondritic material is characterized by a $\mu^{182}W$ of -200 ppm, and would satisfactorily explain HSE mantle abundances. Late accretion will not affect ^{142}Nd given the close Nd concentrations and isotope compositions between the mantle and chondrites. We cannot infer if such a model explains the ^{182}W positive anomaly detected in the PPH, since these samples have not been analysed for their HSE abundances. Nevertheless, the samples where both ^{182}W and HSE have been measured (e.g. Touboul et al., 2012; Rizo et al., 2016) show that these are not correlated.

Interestingly, the major and trace element compositions of some ferropicrite sources have been proposed to reflect Fe-rich mantle originating from the infall of Fe-rich SNC (shergottite–nakhlite–chassignite) meteorites believed to originate from Mars, HED (howardite–eucrite–diogenite) achondrites or ordinary chondrites (Milidragovic and Francis, 2016). Our results show that the PPH source was characterized by $\mu^{182}W$ between 0 and +14. Given that chondritic meteorites are characterized by $\mu^{182}W$ of -200 ppm (Kleine et al., 2009), ordinary chondrite

seems unlikely to explain the PPH ferropicrite source, but the Martian mantle is estimated to have a $\mu^{182}W$ of >300 ppm (Kleine and Walker, 2017) and the HED meteorites have $\mu^{182}W$ an order of magnitude higher (Touboul et al., 2015), which could account for the excess of ^{182}W in the source of the PPH rocks. This model by Milidragovic and Francis (2016) was however proposed for subalkaline ferropicrites and may not be applicable to the alkaline PPH ferropicrites.

8.0 Conclusion

The PPH sequence hosts tholeiitic basalts and ferropicritic rocks including differentiated Fe-rich ultramafic to mafic intrusive rocks, overlain by ferropicritic lavas. The well-preserved nature of the PPH sequence has made it ideal to study Neoarchean ferropicrites and to gain further insights into their mantle source. This study provides important new constraints on the age of the PPH sequence, the relationship between the tholeiitic and the Fe-rich lithologies, as well as the origin and evolution of their mantle source. This study constrained the age of the PPH sequence at 2681±51 Ma, when all representative lithologies are considered on the same isochron. The indistinguishable Nd isotopic composition of the PPH tholeiites and ferropicrites strongly suggest they derived from the same mantle source. Mixing of two sources has been proposed to explain the fact that the ferropicritic lavas are transitioning from alkaline to subalkaline compositions. This is not supported by the Nd isotopic compositions of the PPH rocks, or if such mixing occurred, both sources had similar isotopic compositions at the same time. Short-lived isotopic systems, ^{146}Sm-^{142}Nd and ^{182}Hf-^{182}W, were applied to samples from the PPH to establish if source reservoirs formed in Hadean were involved in the formation of

the PPH sequence. An average $\mu^{142}Nd$=-2.0±3.9, though unresolvable, indicates, when considered with their initial $\varepsilon^{143}Nd$, that both the tholeiites and ferropicrites were sourced from a Hadean mantle formed between 4.56 and 4.47 Ga. The ^{182}W analysis of the PPH sequence demonstrates variable signatures, with 4 samples showing $\mu^{182}W$ values unresolvable from the modern terrestrial mantle and one sample yield a resolvable excess in ^{182}W of +14.1±6.9 ppm. If we assume the PPH is characterized by a positive ^{182}W anomaly, we infer that the ^{146}Sm-^{142}Nd system has become decoupled from the ^{182}Hf-^{182}W system.

Several silicate differentiation scenarios were tested, but no model could reconcile all $\mu^{142}Nd$, $\varepsilon^{143}Nd$ and $\mu^{182}W$ values of the PPH rocks. The occurrence of a decoupled $\mu^{142}Nd$-$\mu^{182}W$ signature is not uncommon in Hadean and Archean rocks. As such, it is possible that an early metal-silicate fractionation event occurred, forming a reservoir characterized by excesses in $\mu^{182}W$ without affecting the $\mu^{142}Nd$ signature. This was followed by a silicate fractionation event only affecting the ^{146}Sm-^{142}Nd system (i.e. occurring after the extinction of ^{182}Hf), resulting in the values we observe in the PPH sequence. An alternative model for the origin of ferropicrites proposed the involvement of Fe-rich meteoritic material in the mantle, which would be consistent with the possible excess ^{182}W of the PPH sequence.

References

Albarède, F. (2001). Radiogenic ingrowth in systems with multiple reservoirs: applications to the differentiation of the mantle–crust system. *Earth and Planetary Science Letters*, *189*(1-2), 59-73.

Allègre, C. J. (2008). *Isotope geology*. Cambridge University Press.

Allegre, C. J., & Lewin, E. (1995). Scaling laws and geochemical distributions. *Earth and Planetary Science Letters*, *132*(1-4), 1-13.

Andreasen, R., et al. "Where on Earth is the enriched Hadean reservoir?." *Earth and Planetary Science Letters* 266.1-2 (2008): 14-28.

Archer, G. J., Mundl, A., Walker, R. J., Worsham, E. A., & Bermingham, K. R. (2017). High-precision analysis of 182W/184W and 183W/184W by negative thermal ionization mass spectrometry: per-integration oxide corrections using measured 18O/16O. *International journal of mass spectrometry*, *414*, 80-86.

Arevalo Jr, R., & McDonough, W. F. (2008). Tungsten geochemistry and implications for understanding the Earth's interior. *Earth and Planetary Science Letters*, *272*(3-4), 656-665.

Babechuk, M. G., Kamber, B. S., Greig, A., Canil, D., & Kodolányi, J. (2010). The behaviour of tungsten during mantle melting revisited with implications for planetary differentiation time scales. *Geochimica et Cosmochimica Acta*, *74*(4), 1448-1470.

Breton, T., & Quitté, G. (2014, March). Aqueous Alteration of Carbonaceous Chondrites and Effects on Tungsten Mass Dependent Isotope Fractionation. In *Lunar and Planetary Science Conference* (Vol. 45, p. 1810).

Bouvier, A., Vervoort, J. D., & Patchett, P. J. (2008). The Lu–Hf and Sm–Nd isotopic composition of CHUR: constraints from unequilibrated chondrites and implications for the bulk composition of terrestrial planets. *Earth and Planetary Science Letters*, *273*(1-2), 48-57.

Boyet, M., & Carlson, R. W. (2006). A new geochemical model for the Earth's mantle inferred from 146Sm–142Nd systematics. *Earth and Planetary Science Letters*, *250*(1-2), 254-268.

Campbell, I. H., & Griffiths, R. W. (1992). The changing nature of mantle hotspots through time: implications for the chemical evolution of the mantle. *The Journal of Geology*, *100*(5), 497-523.

Caro, G., Bourdon, B., Birck, J. L., & Moorbath, S. (2006). High-precision 142Nd/144Nd measurements in terrestrial rocks: constraints on the early differentiation of the Earth's mantle. *Geochimica et Cosmochimica Acta*, *70*(1), 164-191.

Corfu, F., & Muir, T. L. (1989). The Hemlo-Heron Bay greenstone belt and Hemlo Au□ Mo deposit, Superior Province, Ontario, Canada 1. Sequence of igneous activity determined by zircon U□ Pb geochronology. *Chemical Geology: Isotope Geoscience Section*, *79*(3), 183-200.

Cook, D. L., & Schönbächler, M. (2016). High-precision measurement of W isotopes in Fe–Ni alloy and the effects from the nuclear field shift. *Journal of Analytical Atomic Spectrometry*, *31*(7), 1400-1405.

Fletcher, I.R., Rosman, K.J.R. (1982). Precise determination of initial εNd from Sm–Nd isochron data. *Geochimica et Cosmochimica Acta,* 46, 1983–1987.

Francis, D., Ludden, J., Johnstone, R., & Davis, W. (1999). Picrite evidence for more Fe in Archean mantle reservoirs. *Earth and Planetary Science Letters*, *167*(3-4), 197-213.

Gannoun, A., Boyet, M., Rizo, H., & El Goresy, A. (2011). 146Sm–142Nd systematics measured in enstatite chondrites reveals a heterogeneous distribution of 142Nd in the solar nebula. *Proceedings of the National Academy of Sciences*, *108*(19), 7693-7697.

Garçon, M., Boyet, M., Carlson, R. W., Horan, M. F., Auclair, D., & Mock, T. D. (2018). Factors influencing the precision and accuracy of Nd isotope measurements by thermal ionization mass spectrometry. *Chemical Geology*, *476*, 493-514.

Gibson, S. A., Thompson, R. N., & Dickin, A. P. (2000). Ferropicrites: geochemical evidence for Fe-rich streaks in upwelling mantle plumes. *Earth and Planetary Science Letters*, *174*(3-4), 355-374.

Gibson, S. A. (2002). Major element heterogeneity in Archean to Recent mantle plume starting-heads. *Earth and Planetary Science Letters*, *195*(1-2), 59-74.

Goldstein, S. B., & Francis, D. (2008). The petrogenesis and mantle source of Archaean ferropicrites from the Western Superior Province, Ontario, Canada. *Journal of Petrology*, *49*(10), 1729-1753.

Green, D. H., & Ringwood, A. E. (1967). The genesis of basaltic magmas. *Contributions to Mineralogy and Petrology*, *15*(2), 103-190.

Hanski, E. J., & Smolkin, V. F. (1989). Pechenga ferropicrites and other early Proterozoic picrites in the eastern part of the Baltic Shield. *Precambrian Research*, *45*(1-3), 63-82.

Heinonen, J. S., & Luttinen, A. V. (2008). Jurassic dikes of Vestfjella, western Dronning Maud Land, Antarctica: Geochemical tracing of ferropicrite sources. *Lithos*, *105*(3-4), 347-364.

Hirschmann, M. M., Kogiso, T., Baker, M. B., & Stolper, E. M. (2003). Alkalic magmas generated by partial melting of garnet pyroxenite. *Geology*, *31*(6), 481-484.

Horan, M. F., Carlson, R. W., Walker, R. J., Jackson, M., Garçon, M., & Norman, M. (2018). Tracking Hadean processes in modern basalts with 142-Neodymium. *Earth and Planetary Science Letters*, *484*, 184-191.

Jackson, M. G., & Carlson, R. W. (2012). Homogeneous superchondritic 142Nd/144Nd in the mid-ocean ridge basalt and ocean island basalt mantle. *Geochemistry, Geophysics, Geosystems*, *13*(6).

Jakobsen, J. K., Veksler, I. V., Tegner, C., & Brooks, C. K. (2005). Immiscible iron-and silica-rich melts in basalt petrogenesis documented in the Skaergaard intrusion. *Geology*, *33*(11), 885-888.

Jennings, E. S. (2016). *Ferropicrites as evidence for lithological heterogeneity in the mantle source of continental flood basalts* (Doctoral dissertation, PhD thesis). University of Cambridge).

Jennings, E. S., Holland, T. J., Shorttle, O., Maclennan, J., & Gibson, S. A. (2016). The composition of melts from a heterogeneous mantle and the origin of ferropicrite: application of a thermodynamic model. *Journal of Petrology*, *57*(11-12), 2289-2310.

Jochum, K. P., Willbold, M., Raczek, I., Stoll, B., & Herwig, K. (2005). Chemical Characterisation of the USGS Reference Glasses GSA-1G, GSC-1G, GSD-1G, GSE-1G, BCR-2G, BHVO-2G and BIR-1G Using EPMA, ID-TIMS, ID-ICP-MS and LA-ICP-MS. *Geostandards and Geoanalytical Research*, *29*

Kellogg, L. H., Hager, B. H., & Van Der Hilst, R. D. (1999). Compositional stratification in the deep mantle. *Science*, *283*(5409), 1881-1884.

Keshav, S., Gudfinnsson, G. H., Sen, G., & Fei, Y. (2004). High-pressure melting experiments on garnet clinopyroxenite and the alkalic to tholeiitic transition in ocean-island basalts. *Earth and Planetary Science Letters*, *223*(3-4), 365-379.

Kitayama, Y. C., & Francis, D. (2014). Iron-rich alkaline magmatism in the Archean Wawa greenstone belts (Ontario, Canada). *Precambrian Research*, *252*, 53-70.

Kleine, T., Mezger, K., Palme, H., & Scherer, E. (2005, March). Tungsten isotopes provide evidence that core formation in some asteroids predates the accretion of chondrite parent bodies. In *36th Annual Lunar and Planetary Science Conference* (Vol. 36).

König, Münker, Hohl, Paulick, Barth, Lagos, . . . Büchl. (2011). The Earth's tungsten budget during mantle melting and crust formation. *Geochimica Et Cosmochimica Acta, 75*(8), 2119-2136.

Lee, D. C., & Halliday, A. N. (1995). Hafnium-tungsten chronometry and the timing of terrestrial core formation.

Li, Z., Chen, B., Wei, C., Wang, C., & Han, W. (2015). Provenance and tectonic setting of the Paleoproterozoic metasedimentary rocks from the Liaohe Group, Jiao-Liao-Ji Belt, North China Craton: insights from detrital zircon U–Pb geochronology, whole-rock Sm–Nd isotopes, and geochemistry. *Journal of Asian Earth Sciences*, *111*, 711-732.

Liu, J., Touboul, M., Ishikawa, A., Walker, R. J., & Pearson, D. G. (2016). Widespread tungsten isotope anomalies and W mobility in crustal and mantle rocks of the Eoarchean Saglek Block, northern Labrador, Canada: implications for early Earth processes and W recycling. *Earth and Planetary Science Letters*, *448*, 13-23.

Ludwig, K. R. (2012). Isoplot 3.75–4.15: a geochronological toolkit for Microsoft Excel. *Berkeley Geochronology Center Special Publication, Berkeley, California*.

Marks, N. E., Borg, L. E., Hutcheon, I. D., Jacobsen, B., & Clayton, R. N. (2014). Samarium–neodymium chronology and rubidium–strontium systematics of an Allende calcium–aluminum-rich inclusion with implications for 146Sm half-life. *Earth and Planetary Science Letters*, *405*, 15-24.

Milidragovic, D., & Francis, D. (2016). Ca. 2.7 Ga ferropicritic magmatism: A record of Fe-rich heterogeneities during Neoarchean global mantle melting. *Geochimica et Cosmochimica Acta*, *185*, 44-63.

Morino, P., Caro, G., & Reisberg, L. (2018). Differentiation mechanisms of the early Hadean mantle: Insights from combined 176Hf-142,143 Nd values of Archean rocks from the Saglek Block. *Geochimica et Cosmochimica Acta*, *240*, 43-63.

Murphy, D. T., Brandon, A. D., Debaille, V., Burgess, R., & Ballentine, C. (2010). In search of a hidden long-term isolated sub-chondritic 142Nd/144Nd reservoir in the deep mantle: Implications for the Nd isotope systematics of the Earth. *Geochimica et Cosmochimica Acta*, *74*(2), 738-750.

Nagai, Y., & Yokoyama, T. (2014). Chemical separation of Mo and W from terrestrial and extraterrestrial samples via anion exchange chromatography. *Analytical chemistry*, *86*(10), 4856-4863.

Nier, A. O. (1950). A redetermination of the relative abundances of the isotopes of carbon, nitrogen, oxygen, argon, and potassium. *Physical Review*, *77*(6), 789.

O'Neil, J., & Carlson, R. W. (2017). Building Archean cratons from Hadean mafic crust. *Science*, *355*(6330), 1199-1202.

O'Neil, J., Carlson, R. W., Francis, D., & Stevenson, R. K. (2008). Neodymium-142 evidence for Hadean mafic crust. *Science*, *321*(5897), 1828-1831.

Pearce, J. A. (2008). Geochemical fingerprinting of oceanic basalts with applications to ophiolite classification and the search for Archean oceanic crust. *Lithos*, *100*(1-4), 14-48.

Peters, B. J., Carlson, R. W., Day, J. M., & Horan, M. F. (2018). Hadean silicate differentiation preserved by anomalous 142 Nd/144 Nd ratios in the Réunion hotspot source. *Nature*, *555*(7694), 89.

Pin, C., & Zalduegui, J. S. (1997). Sequential separation of light rare-earth elements, thorium and uranium by miniaturized extraction chromatography: application to isotopic analyses of silicate rocks. *Analytica Chimica Acta*, *339*(1-2), 79-89.

Polat, A., Kerrich, R., & Wyman, D. A. (1998). The late Archean Schreiber–Hemlo and White River–Dayohessarah greenstone belts, Superior Province: collages of oceanic plateaus, oceanic arcs, and subduction–accretion complexes. *Tectonophysics*, *289*(4), 295-326.

Polat, A. (2009). The geochemistry of Neoarchean (ca. 2700 Ma) tholeiitic basalts, transitional to alkaline basalts, and gabbros, Wawa Subprovince, Canada: implications for petrogenetic and geodynamic processes. *Precambrian Research*, *168*(1-2), 83-105.

Puchtel, I. S., Blichert-Toft, J., Touboul, M., Horan, M. F., & Walker, R. J. (2016). The coupled 182W-142Nd record of early terrestrial mantle differentiation. *Geochemistry, Geophysics, Geosystems*, *17*(6), 2168-2193.

Puchtel, I. S., Blichert-Toft, J., Touboul, M., & Walker, R. J. (2018). 182W and HSE constraints from 2.7 Ga komatiites on the heterogeneous nature of the Archean mantle. *Geochimica et Cosmochimica Acta*, *228*, 1-26.

Righter, K., & Shearer, C. K. (2003). Magmatic fractionation of Hf and W: constraints on the timing of core formation and differentiation in the Moon and Mars. *Geochimica et Cosmochimica Acta*, *67*(13), 2497-2507.

Rizo, H., Boyet, M., Blichert-Toft, J., & Rosing, M. (2011). Combined Nd and Hf isotope evidence for deep-seated source of Isua lavas. *Earth and Planetary Science Letters*, *312*(3-4), 267-279.

Rizo, H., Walker, R. J., Carlson, R. W., Touboul, M., Horan, M. F., Puchtel, I. S., ... & Rosing, M. T. (2016). Early Earth differentiation investigated through 142Nd, 182W, and highly siderophile element abundances in samples from Isua, Greenland. *Geochimica et Cosmochimica Acta*, *175*, 319-336.

Shaheen, M., Gagnon, J. E., Yang, Z., & Fryer, B. J. (2008). Evaluation of the analytical performance of femtosecond laser ablation inductively coupled plasma mass spectrometry at 785 nm with glass reference materials. *Journal of Analytical Atomic Spectrometry*, *23*(12), 1610-1621.

Stoll, B., Jochum, K. P., Herwig, K., Amini, M., Flanz, M., Kreuzburg, B., ... & Enzweiler, J. (2008). An automated iridium-strip heater for LA-ICP-MS bulk analysis of geological samples. *Geostandards and Geoanalytical Research*, *32*(1), 5-26.

Sun, S. S., & McDonough, W. F. (1989). Chemical and isotopic systematics of oceanic basalts: implications for mantle composition and processes. *Geological Society, London, Special Publications*, *42*(1), 313-345.

Swindle, T. D., Caffee, M. W., Hohenberg, C. M., & Taylor, S. R. (1986). I-Pu-Xe dating and the relative ages of the Earth and Moon. In *Origin of the Moon* (pp. 331-357).

Tanaka, T., Togashi, S., Kamioka, H., Amakawa, H., Kagami, H., Hamamoto, T., ... & Kunimaru, T. (2000). JNdi-1: a neodymium isotopic reference in consistency with LaJolla neodymium. *Chemical Geology*, *168*(3-4), 279-281.

Touboul, M., Kleine, T., Bourdon, B., Palme, H., & Wieler, R. (2007). Late formation and prolonged differentiation of the Moon inferred from W isotopes in lunar metals. *Nature*, *450*(7173), 1206.

Touboul, M., Puchtel, I. S., & Walker, R. J. (2012). 182W evidence for long-term preservation of early mantle differentiation products. *science*, *335*(6072), 1065-1069.

Tuff, J., and S. A. Gibson. "Trace-element partitioning between garnet, clinopyroxene and Fe-rich picritic melts at 3 to 7 GPa." *Contributions to Mineralogy and Petrology* 153.4 (2007): 369-387.

Wilde, S. A., Valley, J. W., Peck, W. H., & Graham, C. M. (2001). Evidence from detrital zircons for the existence of continental crust and oceans on the Earth 4.4 Gyr ago. *Nature*, *409*(6817), 175.

Zhang, J., Liu, Y., Ling, W., & Gao, S. (2017). Pressure-dependent compatibility of iron in garnet: Insights into the origin of ferropicritic melt. *Geochimica et Cosmochimica Acta*, *197*, 356-377.

Appendix A: Whole-rock Major Element Analytical Procedure

Whole rock major element analysis for all was conducted for all 61 samples by X-Ray fluorescence (XRF) spectroscopy at the University of Ottawa X-Ray core facility. Prior to XRF analysis, the LOI content of each sample was determined. Between 1-1.5 g of powdered sample was weighed out into ceramic crucibles and heated in an oven at 1070˚C for 1 hour. The crucibles were then removed from the oven, cooled and re-weighed. For XRF analysis, ~ 0.8 g of sample powder was combined with 7.2 g of a (79:21) $Li_2B_4O_7$: $LiBO_4$ flux and a 1% LiBr non-wetting agent, to make a 1 part sample to 9 parts flux ratio. Samples were fused in Pt crucibles into glass. Sample analysis was carried out on a Rigaku Supermini200WDXRF spectrometer.

The reference materials, UB-N, UM-2, MRG-1, PM-S, BCR-2, WS-E, SY-3, BHVO-2, BM, AN-G, BCR-032 and PC1016, were used for sample calibration curves. During the analytical session, the standards BHVO-2 and GSP-2 were measured in order to determine the accuracy of the analyses (Table A.1 and A.2). Major element oxides of the BHVO-2 standard was measured with an accuracy of <3%. The GSP-2 standard was <8% for all major oxides except P_2O_5, which could be reflective of the low P_2O_5 content in the GSP-2 standard.

Element (wt.%)	Measured BHVO-2 values	Certified BHVO-2 values	± 2S	Accuracy (%)
Na_2O	2.18	2.22	0.16	1.8
MgO	7.23	7.22	0.24	0.1
Al_2O_3	13.6	13.5	0.4	0.7
SiO_2	49.7	49.9	1.2	0.4
P_2O_5	0.27	0.27	0 4	0
K_2O	0.52	0.52	0 2	0
CaO	11.4	11.4	0.4	0
TiO_2	2.72	2.6	0 8	4.6
Fe_2O_{3tot}	12.4	12.3	0.4	0.8

Table A.1. Comparison of the result of the geo-reference standard BHVO-2, which was run during whole rock major element analysis, to the certified values of BHVO-2 (Wilson, 1997).

Element (wt.%)	Measured GSP-2 values	Certified GSP-2 values	± 2S	Accuracy (%)
Na_2O	2.85	2.78	0.18	2.5
MgO	0.99	0.96	0 6	3.1
Al_2O_3	15.1	14.9	0.4	1.3
SiO_2	66.7	66.6	1.6	0.2
P_2O_5	0.18	0.29	0 4	37.9
K_2O	5.38	5.39	0.28	0.2
CaO	2	2.1	0.12	4.8
TiO_2	0.64	0.66	0 4	3
Fe_2O_{3tot}	5	4.9	0.32	2

Table A.2. Comparison of the result of the geo-reference standard GSP-2, which was run during whole rock major element analysis, to the certified values of GSP-2 (Wilson, 1997).

Appendix B: Whole-rock Trace Element Analytical Procedure

Trace element sample preparation and analysis for all 61 samples was undertaken at the geochemistry laboratories at the University of Ottawa.

Approximately 100 mg of powdered sample was weight out in 60 mL Savillex beakers and dissolved using a mixture of 1 mL of concentrated HNO_3 and 5 mL of concentrated HF. The beakers were capped and placed on a hotplate at 125°C for 3 days, after which the beakers opened and placed on the hot plate to evaporate at 85°C. Once dry, the samples were re-dissolved in ~ 10 mL of 6M HCl and closed beakers were placed on the hotplate at 125°C for 2 days. A few drops of boric acid was then added to each sample to break up the fluorides, before evaporate them to dryness at 100°C. Once dry, the samples were re-dissolved in concentrated HNO_3 and evaporated to dryness, this was repeated twice.

Samples were diluted ~4000 times in order to be able to analyze simultaneously highly concentrated elements (ex. Cr) in the order of >1000 ppm at the same time as elements which are >10 ppm range of concentration (ex. HREE). Samples were first dissolved in 40 mL of 7N HNO_3 and placed on a hot plate overnight. The next day, a 1 mL aliquot of the sample solution was taken and mixed with 11 mL of 0 1M HNO_3 + traces HF + 2ppb In, for a total volume of 12 mL of ~ 0.5N HNO_3 + tr HF + ~ 1800 ppb In. Traces of HF are added to solutions to avoid the precipitation of HFSE elements such as Hf. Solutions are doped in In since the amount of In in our samples is negligible, and it provides the ability to monitor the analysis stability and correct for possible analytical drifts.

The trace elements from sample solutions were measured using an Agilent 8800 QQQ Triple Quadrupole inductive coupled plasma mass spectrometer (ICP-MS). Sample preparation and analysis took place in three separate analytical sessions. For each analytical session, 4 USGS reference materials (BCR-2a, BHVO-2, BIR-1a) were analyzed multiple times. This was done for two reasons, firstly to evaluate the reproducibility and accuracy of results (Table 5.3a, b, c and d), and secondly to calculate the trace element concentration of the 61 samples. BIR-1a yielded the most reproducible results, and the values obtained for each analytical session were used to correct each session it was run with.

Over the three analytical sessions, the precision obtained during trace element measurements of the BHVO-2 standard was between 6-10% for the REE, HFSE, Sr, Y, Ni, Cu, Zn, Cr, V and Be, 15% for Ba, 11% for Pb and 26% for Th. The calculated average accuracy during the trace element analysis of the BHVO-2 standard was <6% for REE, Sc, V, Cr, Ni, Cu, Sr, Y, Zr and Pb, and <15% for Th, U, Ba, Nb, Rb and Zn. For the BCR-2a standard calculated precision during trace element analysis was <5% for the REE, U, Sr, Y, Zr, V and Be, <10% for Zr, Cu, Rb, Ta and Pb, and 15-25% for Ba, Cr, Ni and Th. The average accuracy for trace element measurements of the BCR-2 standard was <5% on the REE, Pb, Th, Sc, V, Cu, Zn, Rb, Sr, Y, and Zr, 9-15% for Cr, Nb, Ba and U, 19% for Ni and 35% for Ta. In addition to a BIR-1a standard being dissolved for analysis to correct the data to, an additional BIR-1a sample was measured out, dissolved, and analyzed in order to monitor for precision and accuracy on it. The calculated precision on the values obtained from the BIR-1a standard during trace element analysis was <10% for REE, Pb, U, Sc, V, Cr, Ni, Cu, Rb, Sr, Y, Zr and 10-25% for Zn, Nb, Ba and Ta, and 24% for Ta. The average accuracy was <6% for REE, Sc, V, Cr, Ni, Cu, Zn, Rb, Sr, Y, Zr, Nb Pb, Th and U, and 19% for Ba.

The average result for each session is shown in Table 5.3, along with calculated precision and accuracy for each session, full results of each standard analyzed during each analytical session can be found in Table B.3 a-c.

BCR-2										
Element	Lit value (ppm)	Session 1			Session 2			Session 3		
		Average	Precision (%)	Accuracy (%)	Average	Precision (%)	Accuracy (%)	Average	Precision (%)	Accuracy (%)
Sc	33.53	33.49	9	<1	35 7	9	5	34.13	4	2
V	417.60	421.30	19	<1	427.40	3	2	422.10	6	1
Cr	15.85	14.92	9	6	14.63	8	8	10.59	9	33
Ni	12.57	11.58	5	8	11.26	4	10	7.91	7	37
Cu	19.66	18.64	18	5	17.11	4	13	20.46	7	4
Zn	129.50	139.80	4	8	117.90	4	9	135.30	6	5
Rb	46 2	41.50	3	10	47.74	7	4	48.99	7	7
Sr	337.40	342 0	4	1	333.60	6	1	347.10	5	3
Y	36 7	36.71	4	2	35.60	6	1	36.31	5	<1
Zr	186.50	196.80	4	6	189.90	5	2	192.60	5	3
Nb	12.44	11.26	3	10	10.14	2	19	12 0	6	4
Ba	683.90	652 0	1	5	692.90	3	1	509 0	3	26
La	25 8	26 3	1	4	24.20	2	4	26.20	4	5
Ce	53.12	54.49	1	3	51 8	1	4	55.11	4	4
Pr	6.83	7 6	2	3	6.51	1	5	6.84	4	<1
Nd	28.26	29.66	1	5	27.37	1	3	29.84	4	6
Sm	6.55	6.83	1	4	6.51	2	<1	6.87	5	5
Eu	1.99	2.11	1	6	2 5	1	3	1.94	5	3
Gd	6.81	6.78	18	<1	7 1	0	3	6.87	4	<1
Tb	1 8	1.10	1	2	1 8	4	<1	1 8	4	<1
Dy	6.42	6.52	1	2	6.43	2	<1	6.52	5	2
Ho	1.31	1.33	3	1	1.32	3	<1	1.32	4	<1
Er	3.67	3.75	3	2	3.73	2	2	3.72	6	1
Tm	0.53	0.55	3	3	0.53	2	<1	0.54	6	1
Yb	3.39	3.44	2	1	3.35	2	1	3.36	6	<1
Lu	0.50	0.51	2	1	0.49	2	3	0.51	6	<1
Hf	4.97	4.98	3	<1	4.87	4	2	4.91	3	1
Ta	0.79	0.57	2	27	0.54	4	31	0.43	4	45
Pb	10.59	11.11	4	5	11 2	2	4	10 4	6	5
Th	5.83	4.51	4	23	5.13	2	12	7.18	6	23
U	1.68	1.53	6	9	1.57	2	7	1.57	5	7

Table B.3a. Analytical results for the three sessions for the BCR-2 standard, literature values from Jochum et al. (2016).

BHVO-2							
Element	Lit value (ppm)	Session 2			Session 3		
		Average	Precision (%)	Accuracy (%)	Average	Precision (%)	Accuracy (%)
Sc	31.83	32.81	7	3	35 7	9	2
V	318.20	328.20	4	3	427.40	3	1
Cr	287.20	282.30	3	2	14.63	8	<1
Ni	119.80	121.10	4	1	11.26	4	<1
Cu	129.30	129 0	4	<1	17.11	4	2
Zn	103.90	92.20	3	11	117.90	4	2
Rb	9.26	9.30	3	<1	47.74	7	2
Sr	394.10	383.80	2	3	333.60	6	<1
Y	25.91	25.39	1	2	35.60	6	<1
Zr	171.20	169.30	2	1	189.90	5	2
Nb	18.10	15.10	1	17	10.14	2	3
Ba	130.90	133.20	1	2	692.90	3	26
La	15.20	14.80	1	3	24.20	2	3
Ce	37.53	36.43	1	3	51 8	1	1
Pr	5.34	5.14	1	4	6.51	1	2
Nd	24.27	23.58	1	3	27.37	1	4
Sm	6 2	6 6	1	<1	6.51	2	4.4
Eu	2 4	2 5	2	<1	2 5	1	<1
Gd	6.21	6.37	2	3	7 1	0	<1
Tb	0.94	0.93	3	<1	1 8	4	2
Dy	5.28	5.29	4	<1	6.43	2	2
Ho	0.99	1 1	4	2	1.32	3	<1
Er	2.51	2.65	5	6	3.73	2	1
Tm	0.33	0.34	4	2	0.53	2	2
Yb	1.99	2 1	4	<1	3.35	2	2
Lu	0.28	0.27	3	2	0.49	2	2
Hf	4.47	4.44	2	<1	4.87	4	1
Ta	1.15	0.82	3	29	0.54	4	45
Pb	1.65	1.61	3	3	11 2	2	5
Th	1.22	1 6	2	13	5.13	2	17
U	0.41	0.39	3	5	1.57	2	3

Table B.3b. Analytical results for the three sessions for the BHVO-2 standard, literature values from Jochum et al. (2016).

BIR-1a							
Element	Lit value (ppm)	Session 2			Session 3		
		Average	Precision(%)	Accuracy (%)	Average	Precision(%)	Accuracy (%)
Sc	43.21	43 9	4	<1	35 7	9	6
V	320.60	324.80	2	1	427.40	3	5
Cr	392.90	385.30	2	2	14.63	8	4
Ni	168.90	170.90	3	1	11.26	4	5
Cu	120.70	120.20	3	<1	17.11	4	5
Zn	70.40	63 0	3	11	117.90	4	6
Rb	0.21	0.19	9	10	47.74	7	10
Sr	108.60	103.20	3	5	333.60	6	5
Y	15.60	14.90	2	5	35.60	6	5
Zr	14.80	14 0	2	5	189.90	5	7
Nb	0.55	0.48	1	13	10.14	2	10
Ba	6.75	8.79	1	30	692.90	3	8
La	0.63	0.59	2	6	24.20	2	9
Ce	1.92	1.84	1	4	51 8	1	7
Pr	0.37	0.35	1	6	6.51	1	5
Nd	2.40	2.29	3	5	27.37	1	6
Sm	1.11	1.10	1	1	6.51	2	6
Eu	0.52	0.52	4	<1	2 5	1	4
Gd	1.81	1.76	2	2.7	7 1	0	7
Tb	0.36	0.36	3	<1	1 8	4	5
Dy	2.54	2.51	4	1	6.43	2	5
Ho	0.57	0.58	1	1	1.32	3	7
Er	1.68	1.73	1	3	3.73	2	5
Tm	0.26	0.26	4	2	0.53	2	6
Yb	1.63	1.62	5	<1	3.35	2	4
Lu	0.25	0.25	1	<1	0.49	2	5
Hf	0.58	0.58	4	<1	4.87	4	3
Ta	0 4	0 4	72	3	0.54	4	21
Pb	3 4	2.94	1	3	11 2	2	5
Th	0 3	0 3	3	9	5.13	2	22
U	0 1	0 1	12	5	1.57	2	5

Table B.3c: Analytical results for the three sessions for the BIR-1a standard, literature values from Jochum et al., 2016.

Five duplicate samples of varying lithologies were also sent to Activation Laboratories (Actlabs) for trace element analyses to evaluate the quality of the trace element data obtained at the University of Ottawa. At Actlabs, the samples were processed according to the details outlined on their website under code 4B2 – Research – Lithium Metaborate/Tetraborate Fusion – ICP-MS. The results from Actlabs are compared to the results obtained at the University of Ottawa in Figure 5.2. The trace element concentrations obtained from both laboratories are comparable for all lithologies (red and yellow are black clinopyroxenites, green and pink are ultramafic cumulates and blue is a green clinopyroxenite.

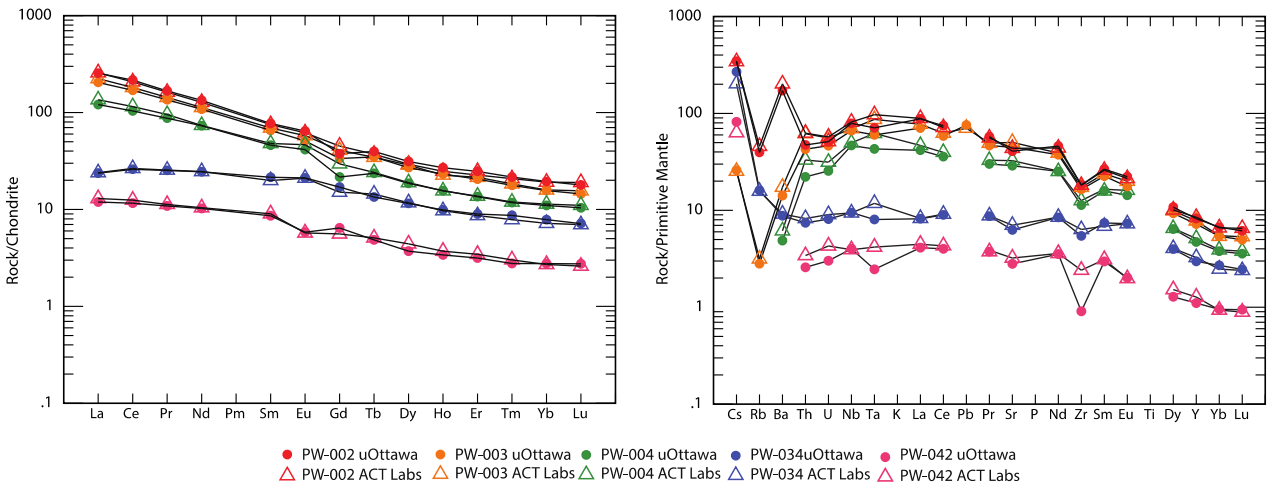

Figure B.2. Normalized Rare Earth Element and Trace Element values for PW-002, PW-003, PW-004, PW-034 and PW-042 samples analysed at the University of Ottawa (circles) and at Actlabs (open triangles).

The average standard error on the REE elements for geo-reference standards BHVO-2, BCR-2 and BIR-1 was generally less than 10%, a calculation of percent difference between the duplicates analyzed by

Actlabs and at the University of Ottawa show that for most of the REE the two are within this error (Table B.4). Only the Zr and Hf concentrations of the ultramafic rock PW-042 obtained at the University of Ottawa are notably to be below the Zr concentration obtained from Actlabs. This may be due to incomplete dissolution of refractory phases containing Zr-Hf during the closed Savillex beaker digestion procedure used at the University of Ottawa, compared to the more aggressive fusion technique used at Actlabs. It is however unlikely that ultramafic rocks contain significant amount of minerals such as zircons and the exact cause for this discrepancy is unknown. Except for Zr and Hf in a few ultramafic samples, the trace element data obtained at the University of Ottawa are in good agreement with the data obtained from an establish commercial lab such as Actlabs.

	La (ppm)	Ce (ppm)	Pr (ppm)	Nd (ppm)	Sm (ppm)	Eu (ppm)	Gd (ppm)	Tb (ppm)	Dy (ppm)	Ho (ppm)	Er (ppm)	Tm (ppm)	Yb (ppm)	Lu (ppm)
PW-002 ACT	61	127	15.4	59.5	11.5	3.58	9.27	1.39	7.44	1.4	3.75	0.53	3.25	0.48
PW-002	60.38	132	15.9	62.3	11.80	3.73	7.73	1.48	7.94	1.53	4.09	0.55	3.30	0.45
% diff	1.02	-3.98	-2.91	-4.47	-2.55	-4.14	19.9	-6.34	-6.29	-8.29	-8.27	-3.69	-1.48	6.08
PW-003 ACT	53.1	111	13.6	52.7	10.6	3.35	8.37	1.29	7.28	1.28	3.55	0.47	2.7	0.40
PW-003	48.4	103	12.85	50.60	10.00	2.95	6.90	1.30	6.86	1.31	3.40	0.45	2.66	0.37
% diff	9.53	6.94	5.83	4.15	5.95	13.37	21.4	-1.09	6.15	-2.49	4.54	3.63	1.45	7.55
PW-004 ACT	32.1	70.4	9.07	34.4	7.33	2.7	6.07	0.9	4.8	0.88	2.27	0.304	1.93	0.28
PW-004	28.6	63.6	8.30	34.1	7.04	2.41	4.44	0.88	4.73	0.88	2.24	0.30	1.87	0.26
% diff	12.06	10.66	9.24	0.84	4.12	12.25	36.6	2.02	1.59	-0.42	1.34	1.47	3.25	6.11
PW-034 ACT	5.67	16.2	2.42	11.5	3.04	1.22	3.1	0.54	2.98	0.55	1.43	0.2	1.22	0.177
PW-034	5.62	15.9	2.40	11.4	3.28	1.23	3.50	0.50	2.93	0.56	1.48	0.22	1.33	0.18
% diff	0.95	1.90	0.70	0.60	-7.36	-0.51	-11.4	7.65	1.73	-1.66	-3.67	-9.67	-8.44	-2.56
PW-042 ACT	3.07	7.64	1.07	4.86	1.38	0.33	1.15	0.19	1.12	0.21	0.57	0.077	0.46	0.066
PW-042	2.83	7.10	1.03	4.78	1.32	0.34	1.32	0.18	0.94	0.19	0.52	0.07	0.47	0.07
% diff	8.59	7.58	3.72	1.62	4.85	-1.84	-13.10	4.85	18.80	9.31	9.36	8.98	-2.01	-5.33

Table B.4. Calculated percent difference between REE values obtained at the University of Ottawa and duplicate samples sent to Actlabs.

	Cr (ppm)	Ni (ppm)	Rb (ppm)	Sr (ppm)	Y (ppm)	Zr (ppm)	Nb (ppm)	Cs (ppm)	Ba (ppm)	Hf (ppm)	Ta (ppm)	Th (ppm)	U (ppm)
PW-002 ACT	< 20	< 20	29.0	921	38.5	203	58.1	2.7	1410	4.40	3.95	5.32	1.2
PW-002			25.2	860	37.4	204.3	56.3	2.73	1200	4.84	2.88	4.01	1.08
% diff			15.3	7.14	3.01	-0.64	3.26	-1.27	17.44	-9.09	36.9	32.7	11.6
PW-003 ACT	< 20	< 20	2.0	1060	35.4	193	49.5	0.2	121	4.5	3.53	5.25	1.17
PW-003			1.78	944	32.8	184	47.3	0.20	98.8	4.48	2.44	3.63	0.97
% diff			12.3	12.21	7.91	4.85	4.63	-2.31	22.4	0.40	44.8	44.7	20.1
PW-004 ACT	< 20	30	< 1	688	23.3	141	35.4	< 0.1	43	3.5	2.53	2.81	0.66
PW-004		38.42	0.62	610	21.4	126	33.2	0.04	34.0	3.45	1.75	1.88	0.54
% diff		-21.92		12.8	8.77	11.06	6.44		26.33	1.53	44.51	49.50	23.2
PW-034 ACT	1510	320	10.0	148	14.8	71	6.7	1.6	64	1.8	0.48	0.7	0.19
PW-034	1685	280.54	10.2	132.35	13.52	60.93	6.76	2.12	61.35	2.01	0.33	0.63	0.17
% diff	-10.39	14.07	-1.86	11.83	9.44	16.53	-0.82	-24.64	4.32	-10.27	46.74	10.95	11.56
PW-042 ACT	3000	1950	< 1	68	5.8	27	2.8	0.5	< 3	0.7	0.17	0.29	0.09
PW-042	3316	1600	0.40	59.06	5.02	10.16	2.86	0.65	4.68	0.26	0.10	0.22	0.06
% diff	-9.52	21.95		15.14	15.60	165.67	-2.00	-22.49		171.22	69.83	32.45	42.23

Table B.5: Calculated percent difference between trace element values obtained at the University of Ottawa and duplicate samples sent to Actlabs.

Appendix C: Column Chromatography Separation Procedure

Acid	Volume	Step
H_2O	5 mL	Rinse Resin
0.4M HCl – 0.5M HF	5 mL	Conditioning
0.4M HCl – 0.5M HF	1 mL	Load
0.4M HCl – 0.5M HF	3 mL	Rinse Majors
9M HCl – 0.05M HF	5 mL	Rinse Ti, Zr, Hf
9M HCl – 1M HF	***10 mL***	***Collect W***
6M HCl	10 mL	Resin cleaning
H_2O	10 mL	Resin cleaning
6M HNO_3 – 3M HF	10 mL	Resin Cleaning
H_2O	5 mL	Resin Cleaning

Table C1: Column chromatography separation of W from whole-rock dissolved samples, using 1 mL of anion exchange resin Eichrom 1x8 200-400 mesh.

Acid	Volume	Step
2N HCl	2 x 10 mL	Conditioning
2N HCl	2 mL	Load Sample
2N HCl	2 x 1 mL	Rinse
2N HCl	2 x 8 mL	Discard
2.5N HCl	10 mL	Discard
6N HCl	***10 mL***	***Collect LREE***
6N HCl	2 x 10 mL	Resin cleaning
H_2O	10 mL	Resin cleaning
6N HCl	10 mL	Resin cleaning
H_2O	10 mL	Resin Cleaning

Table C2: Column chromatography separation procedure for the separation of LREE from whole-rock digested sample for ^{147}Sm-^{143}Nd analysis using Biorad columns filled with 2 mL of cation exchange resin AG50W-X8 200-400 mesh.

Acid	**Volume**	**Step**
0.2N HCl	3 mL	Conditioning
0.2N HCl	0.25 mL	Load Sample
0.2N HCl	0.25 mL	Rinse
0.2N HCl	4.5 mL	Discard
0.2N HCl	***5.5 mL***	***Collect Nd***
0.5N HCl	0.5 mL	Rinse
0.5N HCl	***3.5 mL***	***Collect Sm***
6N HCl	10 mL	Resin Cleaning
0.2N HCl	10 mL	Resin Cleaning

Table C3: Column chromatography separation of Sm and Nd for sample analysis of ^{147}Sm-^{143}Nd using quartz columns filled with 300mg LN spec resin, 50-100µm

Acid	**Volume**	**Step**
MQ Water	1 reservoir	Resin Cleaning
0.5M HCl	1 reservoir	Resin Cleaning
MQ Water	1 reservoir	Resin Cleaning
10M HNO_3	2 mL	Resin Cleaning
10M HNO_3	2 mL	Resin Cleaning
10M HNO_3	2 mL	Resin Cleaning
10M HNO_3 + 20mM $NaBrO_3$	2 mL	Conditioning
10M HNO_3 + 20mM $NaBrO_3$	***0.1 mL***	***Load & Collect***
10M HNO_3 + 20mM $NaBrO_3$	***1 mL***	***Elute & Collect***
10M HNO_3 + 20mM $NaBrO_3$	***5 mL***	***Elute & Collect***
Dry down sample		
MQ Water	2 mL	Resin Cleaning
0.5M HCl	1 reservoir	Resin Cleaning
MQ Water	1 reservoir	Resin Cleaning
10M HNO_3	2 mL	Resin Cleaning
10M HNO_3	2 mL	Resin Cleaning
10M HNO_3	2 mL	Resin Cleaning
10M HNO_3 + 20mM $NaBrO_3$	2 mL	Conditioning
10M HNO_3 + 20mM $NaBrO_3$	***0.4mL***	***Load & Collect***
10M HNO_3 + 20mM $NaBrO_3$	***1 mL***	***Elute & Collect***
10M HNO_3 + 20mM $NaBrO_3$	***5 mL***	***Elute & Collect***
MQ water	2 mL	Resin Cleaning
6M HCl	5 mL	Resin Cleaning
0.2M HCl	2 mL	Resin Cleaning

Table C4: Column chromatography for removal of Ce from LREE cut collected in Table C4, using 0.5 mL LN-spec resin in polyethylene columns

Acid	**Volume**	**Step**
2.5M HCl	10 mL	Conditioning
2.5M HCl	1 mL	Load
2.5M HCl	1 mL	Rinse
2.5M HCl	4mL	Rinse
2.5M HCl	9 mL	Rinse
6M HCl	***6 mL***	***Collect Nd***
6M HCl	***6 mL***	***Collect Nd***
6M HCl	1 reservoir	Resin Cleaning
6M HCl	1 reservoir	Resin Cleaning
MQ H_2O	1 reservoir	Resin Cleaning
6M HCl	1 reservoir	Resin Cleaning

Table C5: Column chromatography protocol for the removal of Na using cation exchange resin AG50W-X8 200-400 mesh.

Acid	**Volume**	**Step**
0.2M HCl	3 mL	Conditioning
0.2M HCl	50 µL	Load
0.2M HCl	100 µL	Rinse
0.2M HCl	100 µL	Rinse
0.2M HCl	11 mL	Rinse
0.2M HCl	***9 mL***	***Collect Nd***
6M HCl	10 mL	Resin Cleaning
6M HCl	10 mL	Resin Cleaning
0.2M HCl	3 mL	Resin Cleaning

Table C6: Column chromatography protocol for the purification of Nd via the removal of Pr and Sm using 20-50um extra fine LN-spec resin (12cm height x 0.4cm width) Teflon columns

Acid	**Volume (mL)**	**Step**
1M HCl- 0.1M HF	3 x 20 mL	Equilibration
1M HCl- 0.1M HF	***5 mL***	***Load and collect W***
1M HCl- 0.1M HF	***3 x 5 mL***	***Rinse tube and collect W***
1M HCl- 0.1M HF	***10 mL***	***Collect W***
2.5M HCl	100 mL	Rinse matrix
4M HCl	30 mL	Rinse matrix
4M HCl	***60 mL***	***Collected REE (Sm, Nd)***
H_2O	20 mL	Resin cleaning
6M HCl	60 mL	Resin cleaning
H_2O	20 mL	Resin cleaning
4M HF	20 mL	Resin cleaning
6M HCl	20 mL	Resin cleaning
H_2O	20 mL	Resin cleaning
4M HF	20 mL	Resin cleaning
6M HCl	20 mL	Resin cleaning
H_2O	20 mL	Resin cleaning

Table C7: Step 1 of 3 separation of HFSE and REE using cation exchange resin AG50W-X8, 200-400 mesh from digested whole rock samples.

Acid	**Volume (mL)**	**Step**
4M HCl – 2M HF	20 mL	Equilibration
4M HCl – 2M HF	20 mL	Equilibration
0.6M HF – 0.36% H_2O_2	~16.6 mL	Loading & elution of major elements, Cr, and Al
1M HCl – 2% H_2O_2	70 mL	Rinse matrix (REE, Ti, Al, Sc, Cr, Zr, Nb, Hf, Ta)
4M HCl – 2M HF	15 mL	Discard
4M HCl – 2M HF	***35 mL***	***Collect W, Mo + traces of Ti***
H_2O	20 mL	Resin cleaning
4M HNO_3 – 0.5M HF	40 mL	Resin cleaning
H_2O	20 mL	Resin cleaning
4M HCl – 2M HF	40 mL	Resin cleaning
H_2O	20 mL	Resin cleaning
4M HNO_3 – 0.5M HF	40 mL	Resin cleaning
H_2O	20 mL	Resin cleaning
4M HCl – 2M HF	40 mL	Resin cleaning
H_2O	20 mL	Resin cleaning

Table C8: Step 2 of 3 – separation of W from HFSEs using 10 mL of anion exchange resin AG1-X8, 200-400 mesh.

Acid	**Volume**	**Step**
4M HNO_3 – 0.5M HF	5 x 1 mL	Clean resin
H_2O	1 mL	Clean resin
4M HNO_3 – 0.5M HF	5 x 1 mL	Clean resin
0.5M HF – 0.3% H_2O_2	1.5 mL	Load
1M HCl – 2% H_2O_2	2 x 0.75 mL	Rinse
4M HCL – 2M HF	***4 * 1 mL***	***Collect***

Table C9: Step 3 of 3 – clean up of W using 30 µL of anion exchange resin AG1-X8 200-400 mesh.

Appendix D: Sample Name and GPS Locations

Sample Number	Sample Name	Easting	Northing
PW-001	Black Clinopyroxenite	552155	5381186
PW-002	Gabbro	552162	5381164
PW-003	Gabbro	552160	5381174
PW-004	Gabbro	552149	5381163
PW-005	Peridotite	552192	5381239
PW-006	Green Clinopyroxenite	552168	5381238
PW-007	Black Clinopyroxenite	552176	5381247
PW-008	Black Clinopyroxenite	552312	5381293
PW-009	Black Clinopyroxenite	552309	5381288
PW-010	Green Clinopyroxenite	552296	5381288
PW-011	Black Clinopyroxenite	552310	5381275
PW-012	Gabbro	552309	5381292
PW-013	Dunite	552307	5381319
PW-014	Black Clinopyroxenite	551989	5381177
PW-015	Black Clinopyroxenite	552013	5381147
PW-016	Gabbro	552014	5381165
PW-017	Black Clinopyroxenite	552036	5381158
PW-018	Black Clinopyroxenite	552049	5381143
PW-019	Fe-rich lava	552254	5381364
PW-020	Fe-rich lava	552277	5381362
PW-021	Fe-rich lava	552287	5381375
PW-022	Fe-rich lava	552290	5381376
PW-023	Fe-rich lava	552291	5381368
PW-024	Fe-rich lava	552638	5381398
PW-025	Green Clinopyroxenite	552634	5381385
PW-026	Tholeiite	552519	5381634
PW-027	Tholeiite	552523	5381636
PW-028	Tholeiite	552533	5381364
PW-029	Tholeiite	552604	5381619
PW-030	Tholeiite	552602	5381622
PW-031	Tholeiite	552617	5381632
PW-032	Tholeiite	552635	5381633
PW-033	Peridotite	552607	5381538
PW-034	Tholeiite	552601	5381526
PW-035	Green Clinopyroxenite	552347	5381335
PW-036	Green Clinopyroxenite	552356	5381337
PW-037	Green Clinopyroxenite	552368	5381333

PW-038	Green Clinopyroxenite	552375	5381329
PW-039	Dunite	552374	5381316
PW-040	Dunite	552358	5381318
PW-041	Peridotite	552360	5381325
PW-042	Dunite	552347	5381318
PW-043	Dunite	552557	5381318
PW-044	Dunite	552568	5381322
PW-045	Black Clinopyroxenite	552354	5381124
PW-046	Peridotite	556345	5381126
PW-047	Dunite	552339	5381131
PW-048	Gabbro	552237	5381053
PW-049	Gabbro	552233	5381045
PW-050	Gabbro	552235	5381043
PW-051	Gabbro	552234	5381043
PW-052	Black Clinopyroxenite	552239	5381051
PW-053	Fe-rich lava	552469	5381392
PW-054	Black Clinopyroxenite	552400	5381353
PW-055	Black Clinopyroxenite	552388	5381351
PW-056	Gabbro	552424	5381477
PW-057	Gabbro	552416	5381481
PW-058	Black Clinopyroxenite	552401	5381484
PW-059	Black Clinopyroxenite	552406	5381484
PW-060	Gabbro	552226	5381339
PW-061	Tholeiite	552141	5381811

Appendix E: Whole-rock Major Element and LOI Results

Sample	Na_2O (wt.%)	MgO (wt.%)	Al_2O_3 (wt.%)	SiO_2 (wt.%)	P_2O_5 (wt.%)	K_2O (wt.%)	CaO (wt.%)	TiO_2 (wt.%)	MnO (wt.%)	Fe_2O_3 (wt.%)	LOI (%)
PW-001	1.82	6.77	6.59	42.2	0.17	0.36	14.4	3.45	0.29	24.0	2.49
PW-002	5.53	1.33	15.2	46.8	0.43	1.10	7.16	0.89	0.37	21.2	1.80
PW-003	4.70	2.77	11.5	46.1	0.26	0.41	9.99	2.00	0.33	21.9	2.30
PW-004	3.00	4.57	8.70	43.4	0.18	0.38	11.9	3.4	0.37	24.1	1.36
PW-005	0.10	18.9	4.41	42.2	0.11	0.05	9.86	1.49	0.31	22.6	4.32
PW-006	0.16	16.6	4.52	42.9	0.10	0.06	16.2	1.84	0.31	17.4	8.12
PW-007	1.11	9.05	6.51	44.2	0.23	0.49	15.1	2.54	0.26	20.6	2.59
PW-008	1.54	6.30	8.71	41.6	0.14	0.70	13.7	3.65	0.28	23.4	1.30
PW-009	1.46	6.51	9.14	41.4	0.14	0.85	13.4	3.28	0.28	23.5	1.36
PW-010	1.07	10.1	6.75	45.0	0.12	0.35	16.4	2.07	0.23	18.0	2.76
PW-011	1.18	8.11	7.11	42.4	0.09	0.44	15.2	3.00	0.24	22.2	2.62
PW-012	4.75	2.17	14.8	48.6	0.32	0.51	8.45	1.48	0.30	18.7	0.00
PW-013	0.06	29.6	4.85	41.7	0.09	0.02	2.5	1.09	0.21	19.9	9.39
PW-014	1.96	8.38	6.87	44.1	0.15	0.83	14.5	2.41	0.27	20.6	4.32
PW-015	1.53	8.24	7.02	43.5	0.11	0.57	14.2	2.91	0.24	21.6	0.39
PW-016	4.69	3.61	12.9	46.3	0.26	0.88	8.46	2.22	0.30	20.4	0.77
PW-017	3.15	5.44	10.3	44.2	0.19	0.59	11.9	2.80	0.29	21.2	0.91
PW-018	1.78	7.24	7.97	41.9	0.1	0.74	12.9	3.84	0.28	23.3	1.28
PW-019	2.28	9.26	10.8	45.6	0.13	0.13	11.1	1.77	0.25	18.6	3.63
PW-020	3.00	6.98	12.9	46.1	0.18	0.31	10.2	2.18	0.23	18.0	1.55
PW-021	1.79	10.3	10.3	44.5	0.14	0.10	12.1	1.72	0.25	18.8	5.19
PW-022	3.46	6.33	11.2	46.8	0.16	0.14	12.2	1.89	0.38	17.5	4.28
PW-023	2.59	7.27	12.5	45.9	0.16	0.37	9.98	2.10	0.29	18.8	0.87
PW-024	3.40	7.41	11.7	47.2	0.13	0.29	9.51	1.86	0.23	18.3	1.53
PW-025	2.14	10.1	10.4	46.8	0.13	0.29	9.53	1.97	0.23	18.5	1.59
PW-026	2.30	8.18	14.8	50.0	0.11	0.18	10.2	1.06	0.17	13.0	1.87
PW-027	1.74	10.5	14.6	45.5	0.11	0.14	11.9	1.09	0.21	14.3	4.55
PW-028	3.01	7.28	14.3	50.6	0.11	0.28	11.5	0.96	0.18	11.8	2.18
PW-029	2.24	9.05	13.9	50.2	0.11	0.14	10.7	0.96	0.18	12.5	1.99
PW-030	0.65	7.66	13.3	50.6	0.1	0.08	14.4	0.92	0.20	12.1	4.91
PW-031	0.65	7.03	13.4	51.8	0.11	0.18	13.3	0.97	0.20	12.3	4.95
PW-032	2.97	7.44	13.6	50.2	0.12	0.24	12.3	0.98	0.18	12.1	2.48
PW-033	0.04	20.4	5.45	44.2	0.09	0.03	7.55	1.22	0.20	20.8	5.43
PW-034	0.51	12.9	6.37	45.8	0.09	0.48	14.3	1.72	0.21	17.6	4.92
PW-035	0.42	15.1	4.93	47.6	0.06	0.11	15.7	1.22	0.20	14.7	4.12
PW-036	0.51	14.7	4.87	47.6	0.08	0.09	16.2	1.26	0.21	14.5	3.82
PW-037	0.48	15.1	4.65	48.2	0.07	0.25	14.6	1.25	0.21	15.3	4.09
PW-038	0.58	14.8	4.63	47.5	0.07	0.14	16.2	1.25	0.21	14.6	4.93

Sample	Na_2O (wt.%)	MgO (wt.%)	Al_2O_3 (wt.%)	SiO_2 (wt.%)	P_2O_5 (wt.%)	K_2O (wt.%)	CaO (wt.%)	TiO_2 (wt.%)	MnO (wt.%)	Fe_2O_3 (wt.%)	LOI (%)
PW-039	0.00	31.5	2.61	40.1	0.05	0.03	2.71	0.70	0.27	22.1	10.7
PW-040	0.05	31.1	3.09	40.0	0.05	0.04	2.13	0.73	0.26	22.5	10.3
PW-041	0.09	21.7	4.04	46.0	0.08	0.03	8.11	1.09	0.28	18.6	3.87
PW-042	0.05	30.6	2.73	40.0	0.05	0.03	3.39	0.69	0.30	22.2	10.9
PW-044	0.05	28.6	3.36	41.3	0.08	0.02	4.03	0.97	0.27	21.4	7.80
PW-045	1.21	6.96	8.44	41.2	0.15	1.21	13.0	3.38	0.27	24.2	1.44
PW-046	0.07	19.4	3.02	44.4	0.07	0.04	8.81	1.13	0.30	22.7	2.70
PW-047	0.07	25.2	3.25	41.4	0.08	0.05	3.22	0.99	0.26	25.5	6.84
PW-048	4.07	3.80	10.6	44.3	0.26	0.63	9.94	2.50	0.32	23.6	0.76
PW-049	4.68	2.08	13.3	46.0	0.31	0.89	8.67	1.65	0.33	22.1	0.50
PW-050	1.35	6.98	13.8	51.1	0.08	0.15	11.4	1.01	0.21	13.9	1.61
PW-051	2.71	4.47	8.50	42.2	0.17	0.6	11.9	3.79	0.32	25.4	0.51
PW-052	2.96	6.82	8.32	44.6	0.18	0.51	12.7	2.47	0.26	21.1	2.76
PW-053	2.89	10.3	10.4	48.2	0.10	0.17	10.6	1.56	0.22	15.7	2.44
PW-054	1.54	7.97	8.61	43.0	0.11	0.57	13.9	3.04	0.24	21.1	1.88
PW-055	1.36	8.65	7.35	42.2	0.09	0.40	14.4	3.20	0.24	22.1	2.94
PW-056	4.18	4.34	12.5	45.7	0.24	0.62	9.07	2.74	0.33	20.2	2.49
PW-057	5.13	3.08	14.3	47.1	0.31	0.31	7.12	2.09	0.30	20.2	1.00
PW-058	2.53	6.60	9.43	42.4	0.13	0.45	11.8	3.41	0.27	23.0	3.11
PW-059	1.74	7.20	8.50	40.9	0.10	0.91	12.1	3.47	0.26	24.9	3.22
PW-060	3.14	3.96	12.1	44.7	0.23	0.37	11.4	2.61	0.32	21.2	0.82
PW-061	3.43	3.59	10.1	43.49	0.24	0.57	11.1	3.06	0.31	24.1	0.46

Appendix F: ICP-MS Whole-rock Trace Element Data, Normalized to BIR-1a

Sample	V (ppm)	Cr (ppm)	Co (ppm)	Ni (ppm)	Cu (ppm)	Zn (ppm)	Rb (ppm)	Sr (ppm)	Y (ppm)	Zr (ppm)	Nb (ppm)	Cs (ppm)	Ba (ppm)	La (ppm)	Ce (ppm)	Pr (ppm)
PW-001	423	-	58.6	128	575	157	2.47	509	19.0	89.4	25.2	0.29	66.0	24.5	55.1	7.23
PW-002	1.65	-	30.7	-	7.17	230	25.2	860	37.4	204	56.3	2.73	1201	60.4	132	15.9
PW-003	21.1	-	41.3	5.38	234	194	1.78	945	32.8	184	47.3	0.20	98.8	48.5	104	12.9
PW-004	192	-	58.9	38.4	348	177	0.62	610	21.4	127	33.3	0.04	34.0	28.6	63.6	8.30
PW-005	148	1548	103.3	735	321	109	0.10	83.0	11.6	63.2	12.8	0.02	3.98	17.6	38.9	4.92
PW-006	179	997	63.6	383	524	86.9	0.29	459	10.6	54.3	11.3	0.04	4.90	13.7	31.5	4.15
PW-007	284	551	60.6	193	445	112	1.87	208	15.5	73.2	15.2	0.13	421	19.9	46.7	6.30
PW-008	530	-	66.9	83.1	444	128	6.81	254	20.8	91.8	15.2	0.47	182	16.9	40.7	5.60
PW-009	465	0.91	62.9	136	411	128	10.4	403	21.7	93.9	17.6	0.71	217	19.0	45.4	6.18
PW-010	316	209	57.7	215	392	89.6	0.73	229	15.6	57.2	11.0	0.02	192	13.0	31.3	4.40
PW-011	670	45.5	81.6	269	640	90.4	3.16	185	17.1	76.5	11.5	0.27	129	11.6	29.3	4.10
PW-012	16.2	-	41.4	0.41	97.0	203	2.01	461	35.2	200	38.6	0.14	328	41.8	93.8	11.8
PW-013	151	2890	123.3	1752	177	98.6	0.31	41.4	6.89	34.3	4.68	0.32	1.80	5.30	12.9	1.83
PW-014	310	293	63.8	160	645	118	17.0	325	16.4	84.8	17.2	1.09	267	18.7	42.3	5.59
PW-015	603	41.0	77.8	251	731	114	3.81	190	16.6	75.6	12.2	0.12	102	12.7	31.2	4.47
PW-016	126	-	49.9	13.6	166	158	20.7	301	29.3	169	29.0	1.06	403	30.8	70.0	9.17
PW-017	384	-	66.7	70.4	410	141	2.25	253	25.8	126	20.9	0.03	161	22.4	52.7	7.09
PW-018	687	1.17	85.4	142	596	138	13.3	210	17.5	88.7	13.6	0.61	219	13.4	32.6	4.53
PW-019	298	925	79.5	465	226	102	0.35	80.8	20.3	82.6	5.41	0.04	34.5	6.36	17.2	2.63
PW-020	382	164	62.3	125	190	111	1.50	209	27.3	111	7.84	0.05	187	9.34	25.2	3.84
PW-021	285	907	77.5	434	170	102	0.19	103	21.2	90.4	5.57	0.05	15.9	7.09	19.2	2.92
PW-022	319	647	73.8	339	0.67	124	0.28	162	23.5	95.8	6.08	0.04	32.8	8.41	21.9	3.32
PW-023	398	382	74.2	227	200	152	9.79	166	26.6	114	8.88	0.37	215	9.89	26.2	3.90
PW-024	372	65	70.6	104	141	82.7	2.71	131	20.5	95.1	6.65	0.72	36.5	7.62	19.9	2.93
PW-025	409	327	77.1	187	180	97.9	3.16	92.1	20.5	94.0	7.14	0.31	38.4	7.63	20.7	3.16
PW-026	285	400	50.0	96.8	65.0	87.5	1.72	155	26.3	55.8	3.81	0.03	19.2	4.90	12.8	1.92
PW-027	305	579	61.7	179	53.8	109	1.50	101	29.3	64.2	4.00	0.05	17.4	5.27	14.2	2.10
PW-028	256	392	47.6	115	96.4	82.7	4.34	111	24.7	68.4	3.44	0.06	36.2	4.43	11.8	1.75
PW-029	259	437	51.4	129	76.7	71.0	0.78	191	23.0	32.1	2.76	0.02	27.7	3.76	9.96	1.54

Sample	V (ppm)	Cr (ppm)	Co (ppm)	Ni (ppm)	Cu (ppm)	Zn (ppm)	Rb (ppm)	Sr (ppm)	Y (ppm)	Zr (ppm)	Nb (ppm)	Cs (ppm)	Ba (ppm)	La (ppm)	Ce (ppm)	Pr (ppm)
PW-030	242	396	45.3	118	34.6	70.1	0.32	110	22.6	28.2	2.67	0.03	11.3	3.58	9.52	1.47
PW-031	236	470	47.7	147	36.2	73.3	3.40	174	24.4	38.9	2.96	0.07	17.9	3.94	10.7	1.63
PW-032	259	394	47.9	118	91.6	71.2	2.34	484	25.8	39.9	3.19	0.11	56.4	4.15	10.9	1.69
PW-033	224	1624	124	1083	227	201	0.14	35.7	10.5	59.6	6.33	0.13	4.28	6.95	17.5	2.52
PW-034	316	1685	59.2	281	403	68.9	10.2	132	13.5	60.9	6.76	2.12	61.4	5.62	15.9	2.4
PW-035	263	1842	77.9	469	778	64.0	0.35	60.1	9.20	36.2	3.48	0.08	35.2	4.13	11.2	1.73
PW-036	241	1904	72.1	439	858	61.3	0.20	40.1	10.7	42.6	4.45	0.03	13.7	5.46	14.5	2.18
PW-037	257	1275	76.4	426	292	57.6	5.67	54.2	11.5	50.2	5.33	0.66	155.6	6.12	16.0	2.40
PW-038	269	1802	79.8	452	674	64.2	0.34	54.6	10.8	45.3	4.47	0.06	15.2	4.65	12.8	2.01
PW-039	119	3510	164	1593	38.9	90.5	0.24	17.7	4.58	20.4	3.08	0.28	3.22	3.68	9.34	1.33
PW-040	133	3242	166	1662	31.3	89.6	0.34	29.3	4.34	18.9	3.06	0.60	4.12	3.97	9.20	1.23
PW-041	186	2501	103	815	1136	75.4	0.08	12.7	7.25	37.7	3.85	0.05	4.39	5.51	12.9	1.77
PW-042	111	3316	146	1599	98.8	85.0	0.40	59.1	5.02	10.2	2.86	0.65	4.68	2.83	7.10	1.03
PW-043	123	3513	139	1684	111	88.2	0.29	22.6	6.61	28.4	6.43	0.44	9.63	7.50	17.1	2.23
PW-044	135	2964	144	1667	78.9	76.4	0.21	19.7	7.18	28.3	6.79	0.33	4.26	7.33	17.0	2.26
PW-045	642	6.19	80.6	160	538	119	18.9	613	21.3	97.4	16.5	1.21	362	18.0	43.2	5.84
PW-046	149	1699	134	955	202	90.0	0.14	96.3	7.32	43.4	8.99	0.10	4.75	12.3	26.7	3.35
PW-047	137	723	158	1141	137	93.3	0.44	54.4	6.27	41.2	8.3	0.27	11.2	9.4	20.3	2.61
PW-048	151	0.70	71.1	30.2	384	148	3.05	767	29.8	164	40.4	0.04	168	44.6	99.3	11.8
PW-049	13.2	-	56.6	4.19	132	193	4.72	1282	39.7	216	58.1	0.10	478	58.3	123	14.7
PW-050	337	176	48.9	69.2	154	84.7	1.19	101	20.6	48.1	2.33	0.11	10.9	2.91	7.68	1.21
PW-051	124	-	87.1	16.2	603	208.9	4.45	596	23.5	146	44.0	0.12	138	32.3	72.3	9.17
PW-052	340	203	74.7	156	640	135	5.79	454	20.1	121	27.3	0.23	55.3	29.3	64.0	7.97
PW-053	323	866	68.6	217	190	85.9	0.85	154	18.2	84.0	5.87	0.14	15.2	7.52	19.1	2.70
PW-054	740	-	89.6	120	541	126	12.9	329	21.4	101	9.50	0.82	92.0	11.1	29.2	4.21
PW-055	902	-	95.2	211	730	122	6.04	293	17.6	80.1	7.50	0.69	36.0	8.08	21.9	3.34
PW-056	347	-	63.7	26.1	60.6	161	14.5	240	28.6	154	18.8	2.49	108	20.9	50.4	6.77
PW-057	135	-	53.3	0.66	33.5	164	2.02	363	33.0	182	23.1	0.37	48.5	26.6	64.2	8.67
PW-058	758	-	85.5	117	388	145	7.68	167	23.8	125	12.3	1.20	51.8	13.8	34.8	4.79
PW-059	867	-	91.9	225	538	132	23.9	153	20.4	114	10.6	4.08	98.8	11.7	29.8	4.21
PW-060	226	-	62.2	14.9	114	181	1.05	432	29.6	171	33.2	0.06	257	32.5	73.6	9.34
PW-061	62	-	67.8	7.80	389	209	4.37	522	28.4	173	47.6	0.14	173	38.4	85.7	10.9

Sample	Nd (ppm)	Sm (ppm)	Eu (ppm)	Gd (ppm)	Tb (ppm)	Dy (ppm)	Ho (ppm)	Er (ppm)	Tm (ppm)	Yb (ppm)	Lu (ppm)	Hf (ppm)	Ta (ppm)	W (ppm)	Pb (ppm)	Th (ppm)	U (ppm)
PW-001	30.2	6.17	1.85	4.15	0.80	4.27	0.78	2.07	0.27	1.64	0.24	2.68	1.32	0.41	4.46	1.59	0.47
PW-002	62.3	11.8	3.73	7.73	1.48	7.94	1.53	4.09	0.55	3.30	0.45	4.84	2.88	0.27	4.71	4.01	1.08
PW-003	50.6	10.0	2.95	6.90	1.30	6.86	1.31	3.40	0.45	2.66	0.37	4.48	2.44	0.27	5.38	3.63	0.97
PW-004	34.1	7.04	2.41	4.44	0.88	4.73	0.88	2.24	0.3	1.87	0.26	3.45	1.75	0.33	4.28	1.88	0.54
PW-005	19.6	3.71	0.87	2.69	0.46	2.50	0.47	1.27	0.17	1.02	0.15	1.79	0.71	0.37	1.20	1.03	0.27
PW-006	17.3	3.49	1.22	2.46	0.44	2.34	0.44	1.14	0.15	0.92	0.14	1.60	0.61	0.3	3.05	0.84	0.21
PW-007	26.3	5.42	1.63	4.06	0.67	3.44	0.63	1.72	0.23	1.36	0.19	2.24	0.83	0.38	2.42	1.20	0.32
PW-008	24.8	5.76	1.73	4.76	0.83	4.40	0.83	2.20	0.29	1.75	0.26	2.87	0.84	0.26	2.70	1.09	0.30
PW-009	26.8	6.13	1.84	4.65	0.83	4.61	0.89	2.34	0.31	1.88	0.27	3.01	0.92	0.26	2.20	1.22	0.35
PW-010	19.4	4.42	1.35	3.37	0.61	3.37	0.64	1.63	0.22	1.36	0.19	1.91	0.57	0.25	1.81	0.83	0.23
PW-011	18.3	4.58	1.39	4.62	0.62	3.41	0.63	1.60	0.23	1.41	0.21	2.39	0.60	0.18	2.89	0.97	0.25
PW-012	48.0	9.94	3.05	9.66	1.29	7.01	1.40	3.85	0.54	3.15	0.44	4.57	1.88	0.16	4.36	3.59	0.93
PW-013	8.17	1.95	0.47	1.56	0.27	1.54	0.28	0.74	0.10	0.68	0.10	1.05	0.23	0.23	0.76	0.34	0.12
PW-014	23.3	4.97	1.47	4.05	0.63	3.43	0.65	1.67	0.22	1.33	0.20	2.38	0.89	0.15	3.89	1.24	0.34
PW-015	19.5	4.49	1.44	3.73	0.64	3.48	0.64	1.68	0.22	1.38	0.21	2.29	0.61	0.23	1.83	0.82	0.23
PW-016	37.7	7.96	2.45	6.54	1.07	5.68	1.13	3.05	0.40	2.50	0.36	3.95	1.46	0.17	3.09	2.07	0.56
PW-017	30.6	6.88	2.04	6.00	0.93	5.12	0.97	2.53	0.34	2.16	0.30	3.63	1.04	0.24	2.15	1.39	0.37
PW-018	20.4	4.67	1.59	4.31	0.66	3.67	0.68	1.79	0.24	1.40	0.21	2.70	0.67	0.19	3.82	0.81	0.25
PW-019	12.5	3.51	1.07	4.17	0.63	3.81	0.77	2.10	0.30	1.87	0.28	2.23	0.27	0.17	0.94	0.38	0.11
PW-020	18.4	4.83	1.64	5.75	0.85	5.08	1.00	2.79	0.41	2.41	0.37	2.98	0.38	0.16	2.13	0.55	0.17
PW-021	14.0	3.82	1.13	4.21	0.66	3.89	0.79	2.10	0.31	1.99	0.30	2.36	0.29	0.14	0.57	0.44	0.13
PW-022	15.6	4.16	1.16	4.55	0.71	4.18	0.88	2.36	0.35	2.16	0.34	2.50	0.31	0.12	0.87	0.46	0.12
PW-023	19.7	5.36	1.57	5.25	0.86	5.48	1.12	3.13	0.44	2.67	0.40	3.24	0.33	0.15	0.95	0.88	0.18
PW-024	14.3	3.98	1.31	4.92	0.66	3.83	0.74	2.0	0.29	1.77	0.26	2.40	0.31	0.13	1.35	0.45	0.16
PW-025	15.5	4.19	1.20	4.78	0.67	3.90	0.77	2.04	0.28	1.72	0.25	2.49	0.35	-	1.34	0.51	0.15
PW-026	10.0	3.24	0.84	3.75	0.73	4.97	1.08	3.15	0.48	3.00	0.45	1.89	0.16	0.13	0.68	0.49	0.11
PW-027	11.1	3.63	1.08	4.13	0.73	5.34	1.17	3.47	0.52	3.17	0.51	1.59	0.16	0.14	0.64	0.54	0.11
PW-028	9.05	2.99	0.92	3.56	0.63	4.55	0.98	2.88	0.43	2.75	0.43	1.77	0.14	0.13	1.0	0.43	0.10
PW-029	7.65	2.28	0.80	3.65	0.58	3.75	0.81	2.39	0.34	2.15	0.31	1.16	0.13	0.03	0.8	0.24	0.07
PW-030	7.45	2.3	0.83	3.44	0.53	3.57	0.78	2.25	0.33	2.10	0.31	0.88	0.13	0.04	0.68	0.23	0.07

Sample	Nd (ppm)	Sm (ppm)	Eu (ppm)	Gd (ppm)	Tb (ppm)	Dy (ppm)	Ho (ppm)	Er (ppm)	Tm (ppm)	Yb (ppm)	Lu (ppm)	Hf (ppm)	Ta (ppm)	W (ppm)	Pb (ppm)	Th (ppm)	U (ppm)
PW-030	7.45	2.30	0.83	3.44	0.53	3.57	0.78	2.25	0.33	2.10	0.31	0.88	0.13	0.04	0.68	0.23	0.07
PW-031	8.25	2.79	0.96	3.55	0.60	4.02	0.90	2.70	0.40	2.44	0.37	1.02	0.17	0.13	1.59	0.33	0.09
PW-032	8.58	2.76	0.93	3.71	0.69	4.36	0.98	2.85	0.42	2.64	0.37	1.22	0.16	0.08	3.42	0.34	0.10
PW-033	11.6	2.88	0.72	2.87	0.40	2.26	0.40	1.15	0.16	1.06	0.14	1.49	0.30	0.11	0.89	0.58	0.15
PW-034	11.4	3.28	1.23	3.50	0.50	2.93	0.56	1.48	0.22	1.33	0.18	2.01	0.33	0.23	2.34	0.63	0.17
PW-035	8.71	2.44	0.77	2.50	0.37	2.11	0.40	1.04	0.15	0.85	0.12	1.22	0.16	0.16	0.64	0.29	0.10
PW-036	10.4	2.86	0.88	2.96	0.41	2.18	0.43	1.13	0.17	0.95	0.14	1.42	0.20	0.15	0.63	0.41	0.09
PW-037	11.3	3.03	0.99	3.18	0.47	2.49	0.48	1.17	0.17	1.00	0.14	1.53	0.23	0.11	0.75	0.47	0.11
PW-038	10.1	2.94	0.97	3.02	0.43	2.38	0.48	1.23	0.16	1.05	0.15	1.37	0.20	0.16	1.13	0.43	0.20
PW-039	5.98	1.45	0.40	1.42	0.18	0.95	0.18	0.46	0.07	0.48	0.07	0.53	0.11	0.13	0.78	0.28	0.07
PW-040	5.42	1.20	0.30	1.27	0.17	1.00	0.19	0.51	0.08	0.50	0.08	0.45	0.10	0.25	1.13	0.30	0.08
PW-041	8.37	2.07	0.40	2.04	0.28	1.53	0.28	0.74	0.10	0.67	0.10	1.07	0.16	0.10	1.01	0.39	0.10
PW-042	4.78	1.32	0.34	1.32	0.18	0.94	0.19	0.52	0.07	0.47	0.07	0.26	0.10	0.28	1.18	0.22	0.06
PW-043	9.27	1.98	0.58	1.90	0.24	1.29	0.24	0.73	0.09	0.67	0.09	0.79	0.29	0.26	0.98	0.57	0.15
PW-044	9.78	2.22	0.65	2.24	0.31	1.68	0.31	0.87	0.11	0.75	0.10	0.79	0.31	0.22	0.86	0.55	0.16
PW-045	25.34	5.93	1.85	5.81	0.78	4.31	0.82	2.14	0.30	1.86	0.28	3.11	0.84	0.15	1.50	1.38	0.35
PW-046	13.6	2.72	0.55	2.51	0.30	1.55	0.29	0.86	0.11	0.68	0.10	1.25	0.47	0.05	0.91	0.88	0.20
PW-047	10.6	2.14	0.52	1.99	0.25	1.31	0.24	0.70	0.10	0.69	0.10	1.05	0.41	0.08	1.14	0.78	0.22
PW-048	47.2	9.47	2.78	9.06	1.18	6.42	1.24	3.29	0.45	2.54	0.36	4.19	1.99	0.07	3.90	3.48	0.78
PW-049	58.6	11.75	3.52	10.96	1.45	7.90	1.47	3.84	0.51	3.08	0.44	4.61	2.68	0.09	5.87	4.51	1.02
PW-050	6.45	2.19	0.76	2.75	0.52	3.47	0.75	2.25	0.34	2.28	0.35	1.35	0.09	0.25	0.60	0.36	0.08
PW-051	39.2	8.15	2.19	6.55	1.00	5.35	0.98	2.58	0.36	2.07	0.33	4.14	1.50	0.20	3.16	3.06	0.60
PW-052	33.8	6.85	1.89	5.93	0.84	4.57	0.86	2.22	0.30	1.79	0.26	3.30	0.99	0.11	3.32	2.89	0.52
PW-053	12.9	3.61	1.14	3.86	0.60	3.62	0.70	1.93	0.27	1.74	0.25	2.26	0.22	0.07	1.02	0.66	0.12
PW-054	21.2	5.74	1.64	5.34	0.83	4.82	0.90	2.38	0.32	1.90	0.28	3.35	0.36	0.25	1.34	1.05	0.21
PW-055	17.0	4.68	1.45	4.48	0.69	4.06	0.74	1.97	0.26	1.50	0.22	2.74	0.28	0.21	1.77	0.72	0.15
PW-056	32.1	7.66	2.21	7.05	1.03	5.86	1.11	2.94	0.40	2.41	0.36	3.95	0.64	0.56	2.16	1.93	0.39
PW-057	39.7	9.08	2.80	8.34	1.19	6.75	1.28	3.36	0.46	2.81	0.43	4.44	0.79	0.43	1.96	2.47	0.49
PW-058	23.3	5.90	1.77	5.50	0.82	4.79	0.93	2.47	0.34	2.03	0.29	3.65	0.45	0.39	2.10	1.34	0.27
PW-059	20.4	5.06	1.65	5.19	0.80	4.31	0.82	2.11	0.28	1.73	0.26	3.33	0.39	0.36	1.89	1.25	0.25
PW-060	40.	8.28	2.42	7.42	1.07	6.07	1.17	3.12	0.43	2.54	0.38	4.49	1.15	0.44	5.22	3.26	0.64
PW-061	46.8	9.41	2.67	7.76	1.06	6.00	1.12	2.91	0.39	2.39	0.36	4.48	1.64	0.17	3.37	3.57	0.68

Appendix G: Whole rock W concentrations via isotope dilution

Sample	W (ppb)	2σ error
blank	1	<1
PW-003	394	46
PW-005	759	38
PW-007	1268	37
PW-009	453	17
PW-011	377	22
PW-012	385	7
PW-013	444	55
PW-015	272	8
PW-019	106	9
PW-020	173	7
PW-023	198	7
PW-024	148	8
PW-027	170	7
PW-029	253	31
PW-032	206	6
PW-033	281	20
PW-038	340	19
PW-039	326	6
PW-041	220	16
PW-047	207	12
PW-048	174	4
PW-049	189	6
PW-051	299	17
PW-055	290	13
PW-056	807	64
PW-057	620	32
PW-058	540	40
PW-059	400	40
PW-060	607	23
BCR-2	490	24
BHVO-2	223	6